

Acta Universitatis
Lappeenrantaensis
839



Mohammad Gerami Tehrani

MECHANICAL DESIGN GUIDELINES OF AN ELECTRIC VEHICLE POWERTRAIN



Mohammad Gerami Tehrani

MECHANICAL DESIGN GUIDELINES OF AN ELECTRIC VEHICLE POWERTRAIN

Dissertation for the degree of Doctor of Science (Technology) to be presented with due permission for public examination and criticism in the Auditorium 1318 at LUT University, Finland on the 1st of February, 2019, at noon.

Acta Universitatis
Lappeenrantaensis 839

- Supervisors Professor Jussi Sopenen
LUT School of Energy Systems
LUT University
Finland
- D.Sc. (Tech.) Janne E. Heikkinen
LUT School of Energy Systems
LUT University
Finland
- Reviewers Professor Bengt Jacobson
Department of Mechanics and Maritime Sciences
Chalmers University of Technology
Sweden
- Associate Professor Kari Tammi
Department of Mechanical Engineering
Aalto University
Finland
- Opponents Professor Bengt Jacobson
Department of Mechanics and Maritime Sciences
Chalmers University of Technology
Sweden
- Associate Professor Kari Tammi
Department of Mechanical Engineering
Aalto University
Finland

ISBN 978-952-335-330-5
ISBN 978-952-335-331-2 (PDF)
ISSN-L 1456-4491
ISSN 1456-4491

LUT-yliopisto
Yliopistopaino 2019

Abstract

Mohammad Gerami Tehrani

Mechanical Design Guidelines of an Electric Vehicle Powertrain

Lappeenranta 2019

75 pages

Acta Universitatis Lappeenrantaensis 839

Dissertation

LUT University

ISBN 978-952-335-330-5

ISBN 978-952-335-331-2 (PDF)

ISSN-L 1456-4491

ISSN 1456-4491

The tendency of alternating fossil energy sources with state-of-the-art renewable energy resources is spreading in most contemporary fuel consuming applications, and transportation, as one of the essential human needs, is not an exemption. Electric mobility is becoming more popular and practical day by day. Despite the recent advancements in electric vehicle technology, this state of the art is facing many challenges and requires further development. Improving the efficiency and finding new solutions for upcoming needs with a sustainable design methodology will enhance the progress in this field. Specialized and solitary improvement in this field may lead to weakening the overall efficiency and performance of the electric vehicle. Hence, the objective of this study is to develop a comprehensive approach that considers various aspects of electric vehicle driveline technology consistently in order to simultaneously satisfy different needs. In this dissertation, a multidisciplinary approach is presented for an electric powertrain design process, which covers the initial design optimization as well as evaluating the design endurance and performance. Theoretical and numerical methods, as well as the simulation tools, are applied in order to initiate and validate each design step. Different kinds of electric vehicle application—transportation, high-performance racing, and agriculture—are benchmarked by the presented methodology. Finally, both the study's accomplishments and findings verify the proposed methodology and ensure both a reliable platform and path of action for future developments in electric vehicle driveline design technology.

Keywords: Electric vehicle, hybrid vehicle, driveline, powertrain, efficiency, simulation, design process, gearbox

Acknowledgements

This dissertation drew a period of academic pursuits, during which I have been accompanied and supported by many people. It is a pleasure that I now have the opportunity to express my gratitude to all of them. First and foremost, I would like to express my appreciation and gratitude to my advisor, Professor Jussi Sopenen, for offering me the opportunity to pursue my PhD degree and for entrusting me with challenging projects. He taught me how to strive for excellence in my academic pursuits and helped me to develop my critical thinking and presentation skills. I would also like to thank Janne Heikkinen, DSc (Tech.), for his support during the dissertation publication process.

The comments from the preliminary examiners and opponents of the public examination Professor Bengt Jacobson from Chalmers University of Technology and Associate Professor Kari Tammi from Aalto University are appreciated.

I am also in debt to my master's thesis advisor, Dr. Kimmo Kerkkänen, for his warmest encouragement and support during my master's thesis. I would particularly like to single out my supervisor Juuso Kelkka, MS, at the product development department of Valmet Automotive Inc.: I want to thank you for your excellent cooperation and for all of the opportunities I was given to conduct my research and further my thesis at Lappeenranta.

I would also like to thank all of the Machine Dynamics laboratory group members for the insightful discussions and help along the way.

And finally, I would like to thank my wife Masoumeh and our beloved daughter Dina. Without their unwavering support, love, and understanding, I would have never been able to complete this journey.

The financial support of the Research Foundation of LUT University and the Walter Ahlström Foundation is highly acknowledged.

Mohammad Gerami Tehrani
August 2018
Lappeenranta, Finland

To My Mother

Contents

Abstract

Acknowledgements

Contents

List of publications	11
Nomenclature	15
1 Introduction	17
1.1 The motivation for the study	18
1.2 Electric and hybrid powertrains	19
1.3 Scientific contribution	22
1.4 Dissertation outline.....	24
2 Design methods and materials	25
2.1 Finite Element Analysis	25
2.1.1 Static loads	26
2.1.2 Torsional vibration analysis	28
2.1.3 Electromagnetic study.....	29
2.1.4 The thermomechanical solution	29
2.2 Equivalent stress calculation	31
2.3 The simulation platform	32
2.3.1 Tractive power calculation.....	32
2.3.2 Co-simulation utilization.....	35
2.3.3 Real-time simulation	38
3 A summary of the findings	41
3.1 The initial design process	41
3.2 Lifetime calculation.....	48
3.3 Energy consumption and efficiency	55
3.4 The validation of the functionality of electromechanical systems	60
3.5 Electric tractor performance	61
4 Conclusion	65
4.1 Future studies	66
5 References	69
Publications	

List of publications

This thesis is based on the following papers and the rights have been granted by publishers to include the papers in the dissertation:

- I. Gerami Tehrani, M., and Sopenan, J. (2014). "Torsional Vibration Analysis of Multiple Driving Mode Hybrid Bus Drivetrain," in: *ASME 2014 International Design Engineering Technical Conferences and Computers and Information in Engineering Conference*, pp. V008T11A064–V008T11A064. Buffalo: ASME.
- II. Sinkko, S., Montonen, M., Gerami Tehrani, M., Pyrhönen, J., Sopenan, J., and Nummelin, T. (2014). "Integrated Hub-Motor Drive Train For Off-Road Vehicles," in: *Power Electronics and Applications (EPE'14-ECCE Europe), 2014 16th European Conference on*, pp. 1–11. Lappeenranta: IEEE.
- III. Gerami Tehrani, M., Montonen, J., Immonen, P., Sinkko, S., Kaikko, E., Nokka, J., Sopenan, J., and Pyrhönen J. (2015). "Application of Hub-Wheel Electric Motor Integrated With Two Step Planetary Transmission for Heavy Off-Road Vehicles," in: *ASME 2015 International Design Engineering Technical Conferences and Computers and Information in Engineering Conference*, pp. V003T01A044–V003T01A044. Boston: ASME.
- IV. Gerami Tehrani, M., Kelkka, J., Sopenan, J., Mikkola, A., and Kerkkänen, K. (2016). "Electric Vehicle Energy Consumption Simulation by Modeling the Efficiency of Driveline Components," *SAE International Journal of Commercial Vehicles* 9, no. 2016-01-9016, pp. 31–39.
- V. Lindh, P., Gerami Tehrani, M., et al. (2016). "Multidisciplinary Design of a Permanent-Magnet Traction Motor for a Hybrid Bus Taking the Load Cycle into Account," *IEEE Transactions on Industrial Electronics* 63, no. 6. pp. 3397–3408.
- VI. Sikanen, E., Heikkinen, J., Nerg, J., Gerami Tehrani, M., and Sopenan, J. (2018). "Fatigue life calculation procedure for the rotor of an embedded magnet traction motor taking into account thermomechanical loads," *Mechanical Systems and Signal Processing*, vol. 111, pp. 36–46.

The author's contribution

The articles were written under the supervision of Professors Jussi Sopenan, Aki Mikkola, and Juha Pyrhönen. This dissertation has been written under the supervision of Professor Jussi Sopenan and Doctor Janne E. Heikkinen.

The author was the principal author and investigator in Papers I, III, and IV. The author's contribution to the publications was as follows:

Publication I

The author's contribution in this conference article was analyzing a novel multi-driving mode powertrain for a hybrid bus in order to study system torsional vibration as well as

collaboration in the driveline architecture design. The powertrain components are modeled and analyzed employing the finite element method (FEM). By analyzing the mode shapes from initial model simulation, the critical components are detected and different configurations of the powertrain are analyzed regarding different strategies in modeling. Different strategies are applied to model the components as bar and mass elements and a sensitivity analysis is carried out respectively. Excitations due to the diesel engine and electric machines are calculated and the probability of torsional resonances in the system is defined.

Publication II

The author's scientific contribution in this article was to verify the functionality of an integrated two-speed gearbox and an electric motor for off-road working machinery applications. A dynamic model of planetary gearbox is developed and the control system is modified according to the system response and dynamic characteristics of the planetary gearset and clutch mechanism. The presented model can be used in the future to study different load conditions and to continue developing gear shifting control systems. The model can also be embedded in a full vehicle model to study the practicality and the drive behavior more closely and realistically. The results indicate that it is possible to conduct gear shifting using the proposed approach.

Publication III

The contribution of the author to this conference paper was the implementation of a novel electric powertrain that consists of an integrated two-speed gearbox and EM in a tractor powertrain to obtain a real-time simulation benchmark. The advantages of the proposed system from the performance and efficiency points of view are explained and its functionality is verified by multibody system analysis. Real-time vehicle simulation software is then employed to evaluate the designed powertrain in two different all-electric powertrain architectures that are subjected to comparison at the power-consumption level. The better operation of individually controlled wheels is explained and the lack of a traction control system is shown to manifest itself in the inefficient operation of the hub-wheel EM. The effect of presented driveline configuration on the vehicle power consumption and drive performance is analyzed and discussed in the paper.

Publication IV

The author's contribution in this paper was developing a method for the efficient design of EV transmission by calculating local and total power losses in the driveline. Three types of transmissions—namely manual, automatic and continuously variable transmissions—are embedded in the model. The results are compared for the total energy consumption of the EV and bilateral effect of mechanical and electrical efficiency on the electric vehicle overall efficiency is explained. Based on the model—which includes gearbox losses, gear ratio selection strategy and the efficiency maps of power electronics and the EM—the most efficient option for transmission is a single reduction gear. The

comparison is only done from the point of view of energy efficiency and the additional costs and complications introduced into the system are neglected.

Publication V

The author's role in this journal paper was the mechanical design of the electric motor rotor geometry and fatigue life calculation for a novel hybrid city bus. The stress history is calculated by analyzing a custom driving cycle data and the fatigue life of three different rotor designs that satisfy both mechanical and electrical demands is studied. A new way of design optimization and selection-table formatting are proposed and as a result of the optimization, the optimum rotor design was selected from among three proposed designs. The fatigue life is long enough and the design yields both a good electromagnetic performance and low manufacturing costs, due to the small amount of expensive PM material used when compared with other rotor designs. This paper was an inter-laboratory cooperation between the Machine Dynamics Laboratory and the Laboratory of Electrical Drives Technology.

Publication VI

The author's contribution in this publication was formed of the thermomechanical fatigue life analysis of electric motor rotor taking into account thermomechanical loads. The interaction and counteraction of thermal and mechanical stress in the electric motor rotor is studied. In this journal article, a coupled literature survey is investigated in order to calculate the thermomechanical stresses in an embedded permanent magnet motor. Next, a fatigue life cycle calculation for a chaotic stress history was presented. The data measured from a full electric car in a track test were studied. By analyzing the results, the effect of thermal loads on stress levels and in the predicted fatigue life, in the studied traction motor, is discussed. The total stresses were at an acceptable level, even when the thermal stresses are included. Dr. Janne Nerg provided the measurement data and power loss formulation for the traction motor. Eerik Sikanen is responsible for finite element modeling of the rotor and providing thermal, mechanical, and thermomechanical stress history.

Nomenclature

Latin alphabet

A	Vehicle frontal area	m^2
a	Acceleration	m/s^2
b	Basquin exponent	–
C_d	Air drag coefficient	–
C_r	Rolling resistance coefficient	–
D	Diameter	m
F	Force	N
f	Frequency	Hz
g	Acceleration due to gravity	m/s^2
K	Material properties matrix	–
k	Quantity of rain flow stress classes	–
k_t	Stress concentration factor	–
L	Characteristic length	m
m	Mass	kg
N	Number of load cycles	–
N_f	Number of applied equivalent stress fluctuations	–
P	Power	watt
p	Number of pole pairs	–
p_t	Pressure	Pa
R	Process outcome	–
r	Radius	m
S	Stress	MPa
s	Cross-section area	m^2
T	Torque	Nm
u	Vector of behavior	–
V	Speed	m/s
z	Number of repetitions	–

Greek alphabet

α	Road slope	–
β	S–N curve slope	–
Δ	Variation	–
η	Efficiency	–
ρ	Air density	kg/m^3
σ	Stress	MPa
σ'_f	Fatigue strength coefficient	–
Φ	Magnetic flux	Wb
ω	Rotational speed	rad/s

Subscripts

<i>E</i>	Electrical
<i>eq</i>	Equivalent
<i>diss</i>	Dissipated
<i>LP</i>	Low power
<i>max</i>	Maximum
<i>PM</i>	Permanent magnet
<i>p</i>	Propulsion
<i>rpl</i>	Ripple
<i>S</i>	Sliding
<i>C</i>	Centrifugal
<i>ib</i>	Magnet pocket iron bridge

Abbreviations

CAMBUS	Lappeenranta University of Technology's Green Campus hybrid bus project
CVT	Continuously variable transmission
DTC	Direct torque control
DOF	Degree of freedom
EM	Electric motor
ERA	Electric RaceAbout
EV	Electric vehicle
FE	Finite element
FEA	Finite element analysis
FEM	Finite element method
FL	Front-left
FR	Front-right
FTP-75	Federal Test Procedure
HEV	Hybrid electric vehicle
HIL	Hardware in loop
HMI	Human-machine interface
ICE	Internal combustion engine
NEDC	New European Driving Cycle
PMSM	Permanent magnet synchronous motor
RL	Rear-left
RR	Rear-right
RWD	Rear wheel drive
rpm	Revolutions per minute
SIL	Software in loop

1 Introduction

Electric power can be seen as a green alternative to fossil fuels in many applications (such as transportation) when it is created from natural renewable sources, like the sun, wind, and water. The exploitation of renewable energy resources in electric energy production and the use of the green energy in everyday life are strongly promoted in transportation, which is one of the major energy-consuming sections. The main motivation for this development is to promote utilizing renewable energy resources, improve the efficiency of vehicles, and to reduce harmful exhaust emissions [1]. Considering the strict limitations adopted by governments for greenhouse-gas emission and global warming [2–4], the prospect for urban transportation does not leave any place for fossil fuel vehicles as air quality standards are increasingly expanding worldwide [5–7].

Alongside legislations that prohibit petrol and diesel vehicles' presence on urban roads, electric vehicles (EVs) and hybrid electric vehicles (HEVs) have several benefits over conventional vehicles promote electric mobility. According to [8], the life cycle maintenance costs of an EV are 1.75 times less than a conventional car. The silent operation of the electric motor (EM) conducts less noise to both persons on board and passers-by. More efficient operation and air quality improvement are other advantages of EVs. In order to minimize exhaust emission and maximize the trip range of HEVs, different driveline architectures have been developed as series and parallel drivelines. A schematic of a HEV driveline is shown in Figure 1.

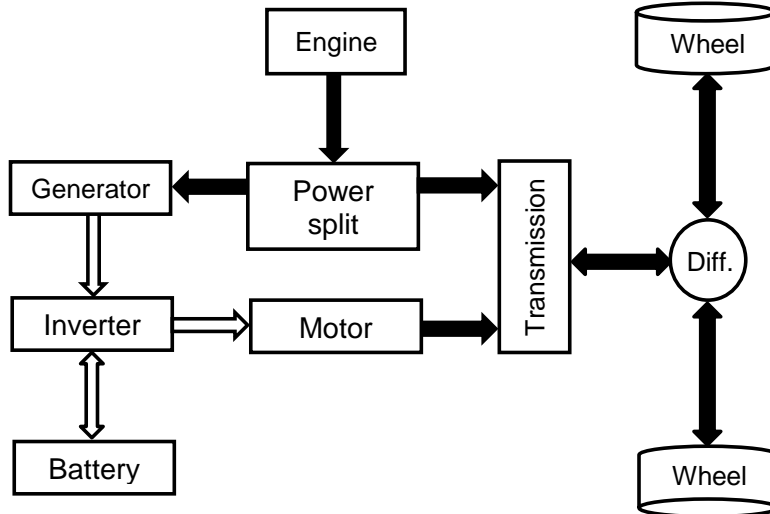


Figure 1. A schematic of a hybrid (series-parallel combination) driveline. Solid and hollow arrows indicate mechanical and electrical connections respectively.

Advancement in EV technology opens new horizons for the further application of electric powertrains in conventional vehicles, either on road or off road [9]. In our research at

Lappeenranta University of Technology, novel concepts and designs have been developed to fulfill new demands for electric mobility (e.g., hybrid city buses and fully electric agricultural tractors). In order to validate concepts and designs, the functionality and dynamic behavior of the electric and hybrid powertrain should be examined beforehand.

1.1 The motivation for the study

EVs and HEVs are taking the place of conventional vehicles by utilizing the advantages of EM operation over internal combustion engines (ICEs) in both performance and efficiency. In EVs and HEVs, not only is the fuel consumption reduced, the use of the regenerative brakes allows the kinetic energy of the vehicle to be converted into electricity and stored in batteries while decelerating. There are different types of EVs and HEVs according to their driveline architecture, which can improve the driving performance and the trip range. One way to increase the travel range of EVs and HEVs is to minimize mechanical power losses in the driveline. According to the studies during the last six years on the amount of dissipated energy in the tank-wheel process by Holmberg et al. [10] and Chong et al. [11], around five percent of engine mechanical power is wasted in transmission. Taking into account the amount global fuel consumption and emission distribution, even a minor improvement in the efficiency of transmission as part of powertrain would not only save a considerable amount of money, but also lower the health hazards to human life.

With the advance of electric mobility technology, various combinations of electric machines and the ICE have been designed according to the HEV category in order to minimize the need for ICE's role in traction. In general, if the electricity is the only applicable propulsive power in the vehicle driveline, the vehicle is called an EV, and when more than one distinct power type is employed for traction (e.g., an ICE and an EM), a HEV is formed.

In all EVs and HEVs there is an EM that provides or contributes to vehicle propulsion. A variety of EMs are used in EV's and HEVs drivetrains regarding to desired application. Permanent magnet synchronous motors (PMSMs) are the most expensive type of electric machines; however, they are commonly applied in electric powertrain design because of their ability to deliver high torque and their compact size, as well as their constant power at high speeds [12]. Furthermore, since the traction control method in EVs is direct torque control (DTC), PMSMs can be considered to offer an optimal option because they can be controlled quickly and efficiently [13]. Unlike an ICE, where maximum torque and power are produced at high rotation speeds, in a PMSM maximum torque is available even at the lowest rotation speeds, allowing the power production to be constant.

In an HEV's powertrain an ICE is placed in order to be used as range extender, genset, or as an assistive power for the main EM. The combination of an EM and an ICE can be either in series configuration or parallel configuration. In a series HEV there is a genset that charges the batteries and an EM that runs the wheels, while in parallel HEVs an EM

and an ICE both contribute to traction. In parallel HEVs, applying a combination of two or more propulsion sources permits management of the operation of the EM and the ICE at optimal efficiency [14]. By contrast, in series hybrid and all-electric powertrains, the EM has to spin at the corresponding road speed, regardless of the required torque.

In the electric and hybrid powertrain the EM is the critical component because of its dominant role as the tractive component, thus a conservative and precise design manner is postulated to avoid malfunctions and failures in both electromagnetic performance and mechanical endurance. The mutual interaction of mechanical and electrical phenomena in hybrid and EV powertrains demands a coherent bilateral approach that simultaneously considers electric machines' principles and mechanical engineering's basis in order to achieve an efficient and durable design. In this dissertation the main focus is on the mechanical aspects of hybrid and electric powertrain design; however, the electrical context is inseparable from the studies and accomplishments. In all design steps not only the electrical engineering prerequisites are considered when the structure had to be modified due to mechanical engineering requisites, the consequence of the structural change on the electrical characteristics of the system is also foreseen at the same time.

The objective of this dissertation is to propose guidelines for the mechanical design of hybrid and electric powertrain based upon comprehensive sets of electro-thermomechanical models that indicate an optimal selection of preliminary parameters, instruct the development of the initial design, and finally, verify the functionality and efficiency of the powertrain. Since the advancement of technology and correlating regulation changes in EVs and HEVs are quite rapid nowadays, a modular design guideline that is compatible with different applications, working environments, and operation legislations will be valuable in terms of decreasing manufacturing expenses.

1.2 Electric and hybrid powertrains

Like conventional vehicles, EVs' and HEVs' powertrains consist of three main components—namely the power source, propulsion unit, and gearbox—with which different types of power source and propulsion unit can be combined to form various kinds of powertrain architecture. The power source in EVs can be fuel cells or batteries of different kinds, and in HEVs a fuel tank is also needed to feed the ICE. According to the studies of [15–17], PMSMs are often used in traction applications, because they provide flexibility with respect to certain important machine design parameters. Their typical properties include high torque and power densities, a high torque capability at low speeds, a wide operating speed range, high efficiencies over the speed range, high reliability, and an acceptable cost [18, 19]. Boldea et al. [20] and Dorrell et al. [21] have studied the different kinds of EMs and generators used in EVs and in their proposed technique, applying permanent magnet machines to improve the efficiency of the machine is the prime criterion during the design of automotive drive motors. PMSMs and

permanent-magnet-assisted synchronous motors have been studied with EV traction drive applications and with different drive cycles [22–24].

In an electric machine's design process, one important parameter is cooling; Polikarpova et al. [25] have done numerical and empirical investigations into an indirect hybrid cooling solution for a small-scale permanent magnet machine, aiming to decrease the magnet's operational temperature in order to improve the efficiency and life cycle. A direct cooling solution for large-scale turbine-generator armature windings was studied by Kilbourne and Holley [26], and according to their results, the output range of the generator can be improved by a more efficient cooling system. According to the results from both studies, the thermal behavior of the electric machine has a dominant role in the efficiency, performance, and endurance of the electric machine.

As the fleet of EVs is increasing, the modern drivetrain architecture has developed to enhance the efficiency and drivability of EVs [27–30]. Sharma et al. [31, 32] have done a technical and financial comparison of conventional vehicles and their equivalent HEVs and fully EVs in different classes. Several hybrid electric powertrain topologies have been introduced for vehicles in order to reduce emissions and improve energy efficiency in the transportation sector. In EVs, power consumption is a major concern in powertrain design, as it affects the life cycle and trip range of the EV.

In particular, these benefits are exceedingly important in city transportation, which has led to the development of hybrid electric busses. As part of the Lappeenranta University of Technology Green Campus project, electric transportation was demonstrated by designing a novel hybrid bus (CAMBUS). The bus is run on a new hybrid electric powertrain that is more energy efficient than the existing powertrains available on the market since it only utilizes a 2.5 liter diesel engine and has a larger battery capacity. The powertrain designed for the hybrid bus is capable of operating in pure electric, series, and parallel hybrid modes. The purpose of the CAMBUS's powertrain design (shown in Figure 2) is to reduce local emissions in the campus area, so the most desirable driving mode is pure electric traction. However, in order to ensure a longer operation range, the diesel engine is kept in the drivetrain. In addition, the diesel engine can be used to assist the electric traction in case more power is needed.

Beside the on-road applications (e.g., in passenger cars and buses), applying the electric powertrain application in heavy off-road vehicles has become interesting because of its advantages compared to conventional powertrains—they have higher efficiency, less local emissions, and silent operation. Nowadays most of the heavy-duty off-road vehicles—like agricultural tractors, wheel loaders, and excavators—have electrically controlled hydraulic or hydro-mechanical drivelines. In general, due to the limitations of the operational range of EMs, they are often incapable of functioning as the hub motors of an off-road machine. In light-road vehicles, such as passenger cars, a gearbox is normally not needed as the starting torque's ratio to the top speed torque is typically in the range of 5–6, while in off-road applications this ratio can be in the range of 10–30. The integration of a two-speed gearbox and a PMSM in one compact package enables

usage of hub motors in off-road vehicles and other heavy machinery, and gives the full benefits of an electric powertrain to the system.

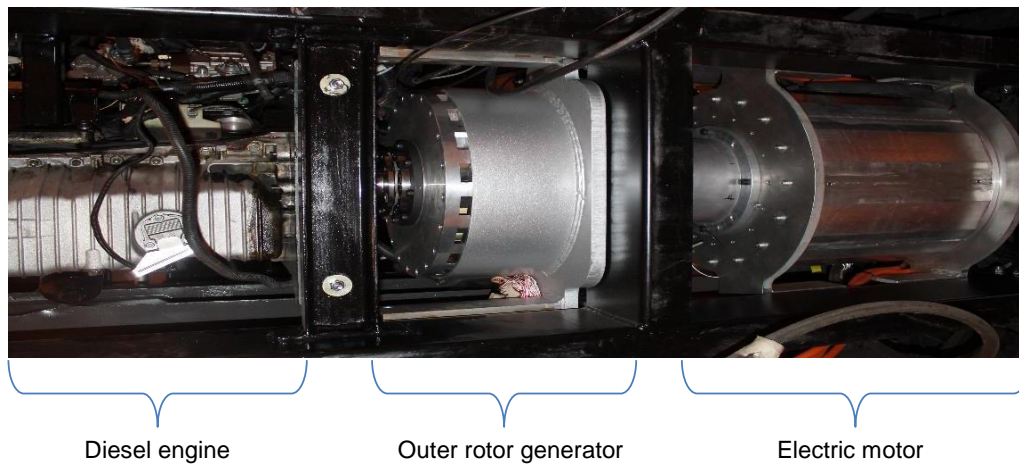


Figure 2. The CAMBUS hybrid powertrain layout (seen from below).

In view of this characteristic of PMSMs, conventional transmission is not required because the EM can provide similar power at different speeds. However, EM efficiency is not homogeneous over equivalent power points, which means that although the same power can be achieved by different torque–speed combinations, the efficiency can vary considerably. The study by Minav et al. [33] on the energy efficiency of hybrid systems showed that the overall efficiency may change by up to 30% by operating the EM in a more efficient pattern. Improving the EM’s efficiency (without consideration of auxiliary components) by shifting the operation point along constant power curves by means of a variable transmission is studied in [34], [35], and [36]. Despite the direct drive systems where the output shaft is directly connected to the payload, in all other applications of electric drives and ICEs, one gear or a set of gears are required to proportionate the desired torque and speed with the produced power. In EVs and HEV, various types of gearsets are utilized to increase the torque, reduce the speed, and let the powertrain operate in parallel mode. However, because the output power of a PMSM is constant after reaching the base speed, in most EVs that are currently available, variable transmission is omitted in the powertrain. Even if the EM power is constant, the efficiency varies significantly by different torque–speed combinations; thus, in EVs a variable gearbox may not be needed from the performance point of view—it can vary the powertrain efficiency considerably.

Definitive conclusions about the overall efficiency of the powertrain cannot be drawn if power losses from the transmission (e.g., the effect of friction) are not taken into account. Thus, a precise model of the gearbox is needed in order to be able to predict power dissipation. According to the studies [37] and [38], to be able to monitor how power losses due to downstream components in the driveline compromise the total efficiency and trip range of an EV requires an agile mathematical model that predicts both electrical and

mechanical efficiency instantaneously. Such a model would enable assessment of the feasibility of applying a variable transmission in an EV powertrain. In most EVs that are currently available, variable transmission is omitted from the powertrain because, from the performance point of view, the output power of the PMSM is constant while the output torque is fixed. However, EV powertrain efficiency is a significant factor that cannot be neglected.

One of the most critical mechanical aspects that should be taken into consideration is the fatigue life of the rotor laminations under actual duty cycles and the maximum stresses at the highest operation speed. These have to be at an acceptable level without sacrificing the useful magnetic flux. However, it should be noted that both the fatigue life and the maximum stress level are significantly affected by the geometric stress concentrations in the rotor laminations. Both of these issues can be significantly influenced by a proper design. The electromechanically important aspects considered are the maximum available torque, the amount of losses, and tolerance for failure situations. From an economic point of view, the price of permanent magnets is naturally important, and thus, the minimum magnet weight is preferred. From the mechanical point of view, a light weight often means less supporting structures, and therefore, special attention has to be paid to ensure the mechanical durability of the structure [39]. The EM is the traction source of an EV and it should be designed, manufactured, and assembled precisely in order to avoid any crucial failures. In the design procedure, these aspects were weighted and the final rotor design was chosen. The affecting terms on the total stress and fatigue life of the EM rotor are mainly centrifugal forces, tangential forces due to torque, and the temperature gradient along the rotor. The rapid increase of heat due to sudden variation of the electric current and the different thermomechanical characteristics of components lead to non-uniform strain in the assembly. Considering the thermal and mechanical stresses imposed on the structure, a multidisciplinary approach that takes to account the transient mechanical and thermal strain simultaneously is required in order to derive the equivalent stress for fatigue life analysis.

1.3 Scientific contribution

In HEVs' and EVs' powertrains, electric machines have the determinant role in the total performance and efficiency. During the electric machine design many parameters need to be considered that affect each other simultaneously. The affecting terms can be named as the electric, electromagnetic, thermal, and mechanical loads. Making change in each of these parameters will influence others, so in order to study electric machines precisely, a comprehensive model that can be updated by any variation in any of the affective terms needs to be developed. This comprehensive model can be built by forming solitary simulation models for the electrical, electromagnetic, thermal, and mechanical behaviors that are capable of interacting with each other upon a common protocol.

The main scientific contribution in this dissertation is developing mechanical design guidelines to improve the performance, efficiency, and durability of an EV powertrain. The improvements are achieved by compiling different approaches for analyzing dynamic

behavior, optimizing geometry, calculating efficiency, and estimating the life cycle of the EV powertrain, based on applications and drive cycles. Based on the **Publications I-VI**, the author's scientific contribution can be summarized in four categories as follow:

- The electric motor is the most dominant component in electric and hybrid drivelines. During the EM rotor geometry design, avoiding mechanical failure of the structure compromises the electromagnetic efficiency and performance of the EM. A new methodology to attaining comprehensive mechanical design process instructions for an EM for a hybrid driveline that considers the electrical, mechanical, and financial aspects is presented in this study. In this methodology an exquisite and acquisitive approach that considers electrical, thermal, and mechanical loads that impose stress on the rotor during the drive cycle is used to analyze EM rotor fatigue life by the superpositioning of mechanical and thermal strain. In the studied cases, the discrepancy between the fatigue life of the rotor under solely mechanical or thermal stress and under combined stresses has been evaluated and the consideration of thermal stress has been found essential for accurate fatigue life calculation. The proposed methodology is explained in detail in **Publications V and VI**.
- Embedding a variable transmission or a fixed ratio gearset has been a challenge in EV driveline design because of the advantages and drawbacks of either solution considering the efficiency and performance aspects. To address this issue, the overall efficiency of the driveline is calculated by modeling the efficiency of gearbox components, power electronics, and electric machines simultaneously. This state of the art gives the opportunity to evaluate the efficiency of a predesigned EV driveline in order to find the most energy efficient solution. The efficiency modeling process is described in **Publication IV**.
- Furthermore, the dynamic behavior and torsional vibration of an innovative hybrid powertrain embedded in a city bus in both series and parallel modes is derived from the driveline. The torsional vibration analysis of hybrid electric drivetrains gets a short shrift as most of the publications consider the torsional vibrations of turbomachinery or reciprocating machines. A model is developed in order to study the dynamic behavior of a novel hybrid powertrain consisting of an ICE, a generator, an EM, a coupling, a clutch, gears, and drive axles. The presented model can be utilized as an instruction for hybrid powertrains in order to avoid failures due to torsional vibration resonances. **Publication I** investigates the modeling techniques and the sensitivity analysis of the novel hybrid driveline.
- Benchmarking the designed driveline is the final step in the design process. In this dissertation a dynamic model of an integrated hub-wheel EM with a two-step planetary gearset for off-road applications is developed by the utilization of multibody dynamics theory. Considering the abrupt and unpredictable change of terrain alongside the EM complication, a precise and agile synchronization of driving and driven clutch halves is vital in order to engage and disengage the clutch properly. In

order to verify the new driveline mechanical functionality and its compatibility with an off-road application, a dynamic model for an integrated two-speed gearbox with an EM is developed and its functionality and quality in off-road application over a given drive cycle are tested and verified by a smart combination of simulation tools. **Publications II** and **III** provide explanation of the modelling of driveline dynamics and the off-line and real-time simulator utilization procedure.

1.4 Dissertation outline

This dissertation consists of four chapters. In the first chapter, an introduction to EVs' and HEVs' advantages over conventional fuel-based automobiles is given and the powertrain architecture is explained. The current advancements and topologies in electric and hybrid powertrains are discussed and challenges for the improvement and development of existing drivelines is presented. In the second chapter a set of methods are presented for verifying the compatibility, functionality, efficiency, and durability of the EV and HEV powertrains used for on-road and off-road applications. In this chapter, instructions are given for an EM rotor lamination geometry design that enables the electromagnetic field to produce the maximum possible torque while the rotor endures under electromagnetic torque. In the third chapter, the presented methods are applied in order to study the dynamic behavior, clutch shifting functionality, fatigue life, and gearbox design of four different powertrain topologies in a hybrid bus, electric tractor, electric race car, and an electric passenger car respectively. Eventually, the achievements are discussed and further possible studies are proposed in the last chapter. The presented publications in the earlier section, **Publications I–VI**, to which the author has contributed, support this dissertation content.

2 Design methods and materials

In vehicle powertrain design, the desired application and performance are the main parameters to take into account in the initial calculation and in component selection. In the preliminary design steps, considering higher safety factors and overestimating the requirements is done, and later, when the overall system compartments fit each other, optimization of the design by modifying each component is carried out. In the design of an EV powertrain, different fields of engineering are applied in order to evaluate the strength, durability, efficiency, and performance of the powertrain. On many occasions a multidisciplinary approach should be adopted in order to be able to consider the interaction of the concerns on each other. Whereas making an everlasting and flawless system with 100% efficiency is not possible, various methods have been presented to increase the lifecycle and safety factors, and to maximize the efficiency. In this dissertation electric and hybrid powertrains are analyzed from efficiency, performance, and durability points of view by applying the FEM, analytical fatigue formulation, and simulation tools respectively. A schematic layout of an HEV driveline design is shown in Figure 3.

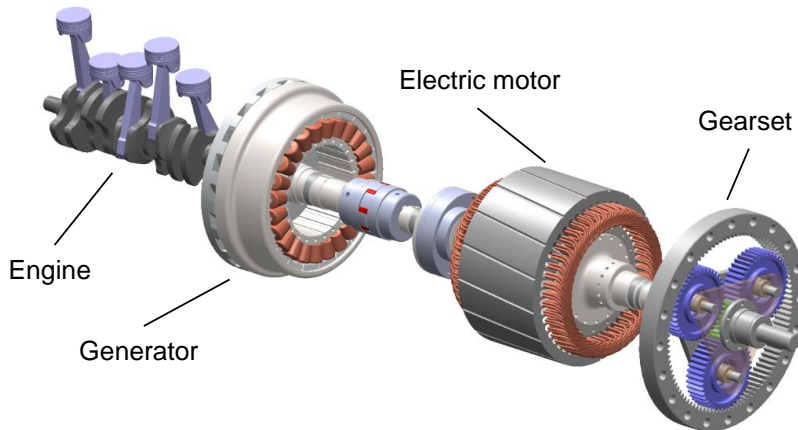


Figure 3. A schematic layout of an HEV driveline design.

2.1 Finite Element Analysis

Finite element analysis (FEA) was originally developed for solving solid mechanics problem by using advancements in computer processors; it is widely used in multiphysics problems for thermal and electromagnetic analysis. FEA is a numerical method that offers a means to find an approximate solution. In the FEM, the final action is approximated by a set of simultaneous algebraic equations [40]:

$$[\mathbf{K}]\{\mathbf{u}\} = \{\mathbf{R}\}, \quad (1)$$

where \mathbf{K} is the material property matrix that governs the system, \mathbf{u} is the vector of behavior of the element, and \mathbf{R} is the outcome of process. The application of the concept of the FEM in different field of physics is illustrated in Table 1 [41].

Table 1. Applications of finite element methods in physics

Application	Property [\mathbf{K}]	Behavior $\{\mathbf{u}\}$	Action $\{\mathbf{R}\}$
Elastic	Stiffness	Displacement	Force
Thermal	Resistance	Temperature	Heat transfer
Fluid	Density	Velocity	Jet thrust
Electrostatic	Permittivity	Electric potential	Charge flow

In the electric and hybrid powertrain, EM is the most critical component because of its inherent multiphasic characteristics and its main role in the traction. In order to design an efficient rotor geometry for the EM rotor, different states of the art have been developed. During the rotor geometry design, three main terms should be regarded simultaneously: durability, functionality, and efficiency. In order to make a durable, effective, and efficient design, the stress flow through the rotor lamination stack should be kept smooth, magnets should be close to the surface, and magnetic flux leakage between magnets should be banned as much as possible respectively.

When finding a solution for a multi-criteria problem, FEA is a powerful means that is applicable to static mechanics, electromagnetic fields, thermodynamics, and rotor dynamics eras. In the following chapters, the utilization of FEA in different design steps is presented. The more detailed explanation can be found in **Publications I, V, and VI**.

2.1.1 Static loads

In the design process of electric and hybrid drivelines, at the EM design step, different concepts and geometries for the EM rotor are initiated by electrical engineers. In order to reduce repetitive calculation, the symmetry of the structure is used and a section that represents the whole rotor is subjected to finite element (FE) study. A formulation for the distributed mechanical load on a beam was applied to calculate the effective stresses on the model. A similar phenomenon also occurs in slitted solid rotors, as it was shown in [39].

In the analysis, the effect of adhesives (i.e., glue or resin) between the magnet and the rotor is neglected. In other words, it is assumed that the magnets are only retained in their pockets by the mechanical structure of the rotor. As a result of this assumption, the external load resulting from the magnet mass at the maximum speed is applied to the upper face of the magnet housing. As shown in Figure 4, considering the centrifugal

forces due to the mass of the magnet pocket iron bridge (F_{ib}) and permanent magnet mass (F_{PM}), the total force is carried by the tension bars.

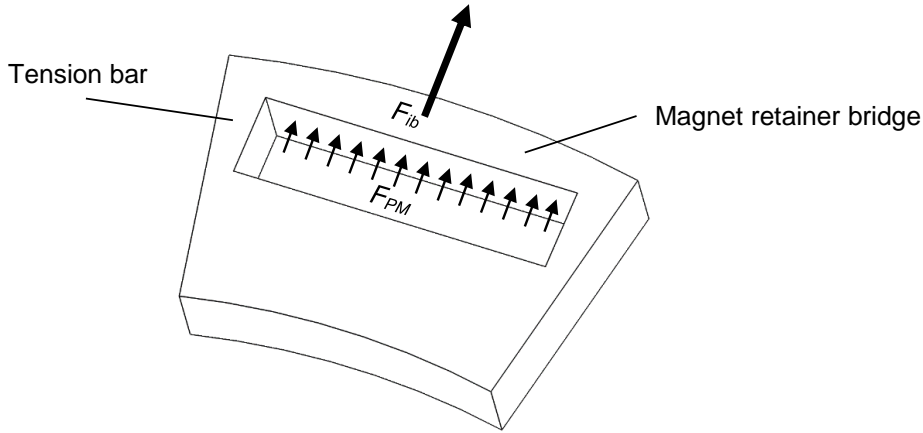


Figure 4. Load modeling and distribution on the rotor section.

The nominal stress caused by the centrifugal force, can be calculated as

$$\sigma = k_t \frac{F_c}{s}, \quad (2)$$

where F_c is centrifugal force, s is the tension bar cross-sectional area, and k_t is the stress concentration factor. In the case of simple geometries, the stress concentration factors can be obtained from mechanical engineering charts. In a general case of complicated geometry, the stress concentration factors can be calculated, applying the FEM. The latter approach is adopted in this study to calculate k_t . The centrifugal force and the stresses caused by it vary in relation to the square of the angular velocity. As a result, the relationship between the EM speed profile and the resulting stress profile can be obtained.

In the PMSM, traction torque is the result of electromagnetic force between the permanent magnets and the magnetic field generated by windings, and the closer the magnets are to the rotor surface, the more efficiently the EM operates. Thus, from the electromagnetic efficiency point of view, magnets should be as close as possible to the rotor surface. But, from mechanical point of view, the deeper the magnets go, the stronger the design is. Considering both electromagnetic force and mechanical strength leads to a multidisciplinary design approach. In this dissertation, three magnet pocket geometry designs have been taken as samples and subjected to a multilateral comparison to enable smart and efficient selection.

2.1.2 Torsional vibration analysis

Rotating machinery can develop excessive dynamic stress if it spins close to their natural torsional frequency. Thus, in order to avoid resonance due to overlapping operational speed and system harmonics, the natural frequencies of the system should be known [42]. The most common modeling method for torsional systems is the mass-elastic model, where the system components are described by the mass moment of inertia and torsional stiffness. By forming the mass-elastic model, the equation of motion is then derived. By solving the equation of motion and finding eigenvalues in the equation, the eigenfrequencies or natural frequencies of the system will be known. The next step is to calculate the excitation loads and frequencies that are imposed upon the system. Possible resonance speeds can be found by combining the information about the system's natural frequencies with excitation frequencies. In most cases, this is accomplished using a frequency interference diagram. In order to decide if the torsional vibration amplitude at the found resonance speed is harmful, a forced vibration analysis should be performed.

Applying FEA, studying powertrain mechanical vibration is quite practical when the geometry becomes complicated. In torsional vibration, the element of the degree of freedom (DOF) is limited to rotation around pivoting axis. Employing FEA makes it possible to calculate powertrain natural torsional frequencies under different drive modes and modeling strategy quite fast. This allows the calculation of the various configurations of modeling technics and drive modes in order to derive the system's natural frequency spectrum and spot those components that the system is sensitive to. Specifically, when a novel custom-designed powertrain that has not been investigated before is subjected to the vibration study. In this dissertation three different techniques for modeling distributed mass and defining equivalent stiffness are presented, calculated, and verified.

In hybrid drivelines, excitations from the combustion engine and electric machines cogging torque influence the torsional vibration. In the well-known four-stroke engine operation principle, the expansion occurs in every half-revolution of the crankshaft. As a result, the working cycle of a four-stroke engine is two crankshaft revolutions, so the engine harmonics i are multiples of 0.5 (e.g., $i = 0.5, 1, 1.5, 2, 2.5$). The excitation torque caused by the gas pressure can be presented as a Fourier series. Each Fourier component of the torque is of the form

$$T_i = \frac{\pi D^2}{4} p_{ii} r, \quad (3)$$

where D is cylinder diameter, r is crank radius, and p_{ii} is the corresponding tangential pressure harmonic component. Alongside the excitation due to the combustion engine, excitation from electric machines affect the driveline. The mechanical frequency of permanent magnet synchronous machine is calculated as follows:

$$f_{rpl} = \frac{f_E}{p}, \quad (4)$$

where f_E is electrical frequency and p is the number of pole pairs.

2.1.3 Electromagnetic study

In a PMSM the electromagnetic efficiency usually is compromised to minimize the risk of mechanical failure. A comprehensive methodology in which electromagnetic efficiency is maximized alongside the mechanical strength is the missing link in the EM design process chain. Finding solutions to the permanent magnet housing pocket in the rotor, with a special focus on the height of the steel bridge covering the pocket and the shape of the hollow space, which are essential both from the mechanical and electromagnetic aspects, is something carried out in this dissertation. The motor design optimization process takes into account the magnet shape, the magnet embedding depth, and the leakage-flux-minimizing air pocket (cavity) areas on magnet sides. The mechanical stresses and the electromagnetic forces are calculated by FEA. The effects of the embedding depth of the magnets on torque, efficiency, demagnetization risk, and mechanical stresses are reported. The results provide guidelines for permanent magnet traction motor design.

The value of the armature reaction magnetic flux Φ depends greatly on the effective air-gap length, which is not easy to obtain accurately by analytical equations when the magnets are embedded and the rotor is non-uniform. Therefore, the FEM was applied to solve Φ . The motor inductances are the most critical parameters when calculating the maximum torque achieved from the motor, because the torque is inversely proportional to the inductance. The inductances presented in this study are computed from the flux values obtained by the FEM and then divided by the current values, as shown in [43].

2.1.4 The thermomechanical solution

The FEM is used to model the transient temperature distribution and stress calculation. The FE study is done in two steps: first, the transient thermal study is carried out to calculate the temperature distribution over the FE rotor model. In the second step, the temperature distribution history is applied as an initial thermal condition for every simulation time step along other mechanical loads in the mechanical study. The FE model of the rotor is built in Ansys. Considering the computational effort of a combined transient thermal and mechanical study of this size, a cyclic symmetry is applied to the FE model.

The measured track data are applied in the calculation of both the instantaneous rotor heat losses and the calculation of the convection constraints in the transient thermal model, as well as being applied in order to determine the torque and rotational speed in the mechanical model [44]. The proposed procedure for the thermomechanical analysis of a rotor under mechanical and thermal loads consists of three main stages. First, the sources

of heat and power conversion causing thermal stresses are formulated, the applied FEM is presented, and finally, the data processing and fatigue life calculation are explained. In Figure 5 a schematic of thermomechanical FEM modeling steps, with a description of the inputs and output, is presented.

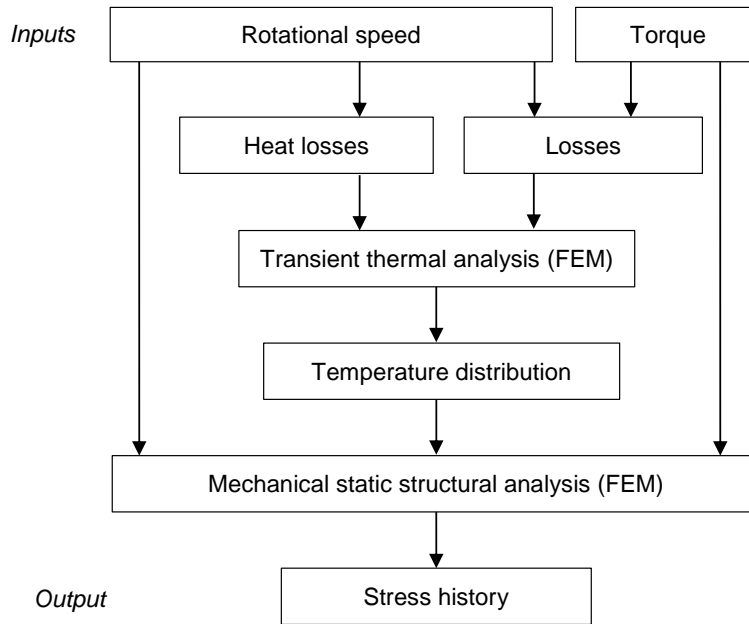


Figure 5. The process of thermomechanical FEM analysis.

When modeling the stresses imposed on the rotor, von Mises stress formulation is used to calculate both mechanical and thermal maximum stress. It may not always be possible to neglect thermal loads, and on the other hand, neglecting them increases uncertainty in the stress calculation. Consequently, higher design safety factors have to be used for the components. In many cases, this results in a too conservative estimation of the actual stresses and leads to the application of more material or a more complex design, thereby increasing the weight and cost of the structures.

An estimation using constant cooling air temperature in the rotor air gap is used. Therefore, by applying proper convection constraints on the outer boundary surfaces of the rotor, only the FE model of the rotor has to be modeled in this study. Because stator losses are efficiently removed by combined liquid and forced-air cooling, the stator losses are not considered as a heat sources in the analysis. However, the losses acting as heat sources in the rotor structure have to be defined.

The most critical section with respect to temperature variation is at the midpoint in the axial direction. This is due to the fact that the rotor laminations create thermal resistance in the axial direction and thus reduce the heat transfer rate in that direction.

2.2 Equivalent stress calculation

Evaluating the durability of the system, a fatigue life calculation is carried out using the stress history calculated in FEM process. The fatigue life is calculated then with thermal loads (**Publication VI**) and without thermal loads (**Publication V**) in order to analyze the influence of temperature variation on the rotor lifecycle.

The Palmgren-Miner linear damage hypothesis method is applied, along with rainflow cycle counting, in order to evaluate the equivalent stress cycle, $\Delta\sigma_{eq}$, out of a complex and non-uniform stress history. The equivalent stress will be employed to identify stress reversals and the damage summation for the structure [45, 46]. The equivalent stress cycle that causes similar fatigue to the rotor as cumulative fatigue damage along the load cycle can be formulated as

$$\Delta\sigma_{eq} = \sqrt[\beta]{\frac{\sum_i^k z_i \Delta\sigma^{\beta}}{N}}, \quad (5)$$

where N is the number of load cycles, k is the quantity of rainflow stress classes, z_i is the number of repetitions in class i , $\Delta\sigma$ is the stress variation in that class, and β is the $S-N$ curve slope.

Following the Basquin equation for the number of applied equivalent stress fluctuations that the structure tolerates until fatigue damage is developed, N_f , this can be solved using the following equation [47]:

$$N_f = 0.5 \left(\frac{\Delta\sigma_{eq}}{2\sigma'_f} \right)^{\frac{1}{b}}, \quad (6)$$

where σ'_f is the fatigue strength coefficient and b is the Basquin exponent or fatigue strength exponent, which varies for most metals between -0.05 and -0.12. Regarding Eq. (4), a smaller b results in a longer fatigue life [48, 49].

The model is also studied in a situation of solitary thermal and mechanical loads to observe the contribution and interaction of either load to the resultant equivalent von Mises stress. A precise numerical calculation with a fine mesh that takes into account both the mechanical and thermal loads is time-consuming, and the repetition of calculations after each modification will make the simulation process even longer. Thus, finding a way to speed up and minimize the design process will save lots of time and money. In this study, a rough model that correlates with a detailed and precise model with a constant scale is developed to make the initial studies faster and more convenient. Finally, an exact simulation with very fine meshing is performed for a model that combines both the mechanical and thermal modifications.

2.3 The simulation platform

The behavior of any system can be evaluated in a virtual environment by simulating real-life circumstances. In order to validate the applicability of the proposed powertrains in different vehicle architectures (e.g., electric drivelines as well as hybrid or all electric drivelines), a generic model needed to be developed. The generic model should be capable of modifying all parameters in integrated simulation software; in this study these are Matlab Simulink, ADAMS, and Mevea. The advantages of utilizing a parametric and dynamic design are that models do not need to be designed from scratch every time and further optimization will proceed quite fast. The main purpose of the generic model is to hasten the modeling processes of the same kinds of product. The benefits of a generic model are more apparent when a variety of products need to be modeled. It will also save a lot of money and time, which can afterwards be spent on other targets [50].

In the following compartment, the utilization of a simulation platform to calculate the efficiency of an EV driveline is described, as is the evaluation of the functionality and performance of driveline mechanisms and a tractor in offline and real-time simulation. More descriptive information can be found in **Publications II, III, and IV**.

2.3.1 Tractive power calculation

Thanks to the advancement in the computational capacity of processors, simulation is an inevitable method for benchmarking a design before production. Utilizing simulators in the powertrain design process of EVs and HEVs is also quite prevalent; they are used to minimize production costs and errors, as well as being used to increase the efficiency and reliability of the final products. Despite the fact that simulation software and hardware have eased the design validation process, the simulation itself needs to be designed efficiently and smartly in order to catalyze the design modification stages. Hence, a generic vehicle dynamic simulation model for electric power consumption over a given driving cycle is developed that enables comparison of the effect of the powertrain configuration on power consumption. The model is composed of electrical component efficiency, drivetrain inertias, gearbox efficiency, regenerative braking, and a shifting scheme that selects the gear ratio according to the vehicle's road speed. In the powertrain design process of EVs and HEVs, a precise dynamic model of the vehicle is vital in order to make it possible to benchmark the efficiency and compatibility of the powertrain components in different powertrain architectures [51].

The EM design for EV and HEV powertrains is done according to the vehicles' dynamic model and the aimed drive cycle. Newton's second law of motion can be applied when initiating the required propulsion power and geometry. However, the required power can be calculated by having resistive forces and inertias, the realistic amount of power that can be extracted from energy reservoir in the vehicle is higher than the power that is gained from calculation, due to losses in the powertrain component (e.g., in the EM, the gear train, etc.). The real consumed power is the summation of power dissipation in each stage of powertrain and the demanded power required to overcome road and air

resistances. The dissipated power in the powertrain consists of power losses in the tr. The propulsion power required to follow the drive cycle for the sample vehicle is calculated as below:

$$P_p = (C_r + \sin \alpha)mgV + \frac{1}{2}\rho C_d AV^3 + (m + m_{eq})aV + P_{diss}, \quad (7)$$

where C_r is the coefficient of normal rolling resistance, α is the road slope, m is the vehicle's total mass, g is gravitational acceleration, V is the vehicle's longitudinal speed, ρ is air density, C_d is the air drag coefficient, A is the vehicle's frontal area, a is the vehicle's longitudinal acceleration and m_{eq} is equivalent translational mass of the rotational inertias of rotating components. In the equation (7), P_{diss} is the dissipated power in the powertrain such as in the traction motor, in the transmission, the tire slippage and tire rolling resistance, etc.

Losses due to friction in support bearings and the gear mesh are called *load-dependent losses*, and losses that come from air resistance and the lubricant used are termed *load-independent losses*. Figure 6 provides a diagram of the power losses of the studied components.

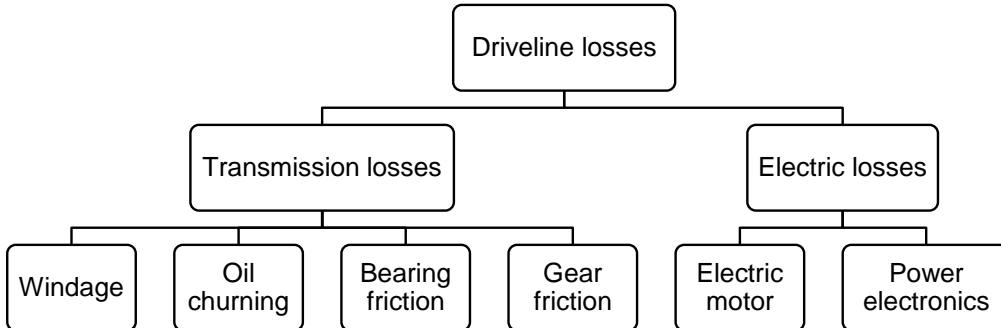


Figure 6. A classification of driveline power losses.

The gearbox has a dominant role in the driveline since it transforms and transfers the produced traction power to the wheels. Since power consumption in EVs is a major concern in powertrain architecture design (as it affects the life cycle and trip range of the EV), in order to have an efficient and durable powertrain, all of the components have to be investigated precisely,

The challenge in the formulation of load-dependent losses comes from the need to derive a friction coefficient that varies during the mesh cycle. In Coulomb's law, the friction coefficient (μ) is a constant value and the resistive force is dependent on normal force variation. In gear tooth pairing, the friction coefficient varies according to the mesh cycle sequence. For this reason, the time dependent method for calculating the friction coefficient that was proposed by [52] is applied in this work in a modified version of Coulomb's law for friction, proposed by [53], which was developed for estimating the resistive force. The methodology developed by [54] is applied in the calculation of load-independent losses, which are divided into oil churning and windage power losses, which represent power losses due to the interaction of individual gears with lubrication fluid and the pumping of oil at the gear mesh.

In order to have a model that considers both rolling and sliding interaction between the gear teeth, a modification of Coulomb's law is applied to obtain the equivalent kinetic friction coefficient. Resistive frictional torque in the supporting bearings is also considered, based on the construction of load-carrying shafts and gears in the gearbox. The load-dependent power losses are defined as a function of the rotating speed and applied torque, while load-independent losses vary by rotational speed.

A number of friction models have been proposed for the calculation of the friction coefficient, such as the Coulomb model, the Benedict and Kelley model, Xu's full model, and the Smoothed Coulomb model, based on the work of Anderson and Loewenthal; it is clear that the friction coefficient is crucial in the calculation of sliding power losses (P_s). In this work, the formulation suggested by Xu [52] is utilized for calculation of the friction coefficient, and the friction type is assumed to be *fully lubricated* in all cases. The detailed formulation of the calculation of the friction coefficient can be found in **Publication IV**.

In a stepped type of gearbox architecture, the gear parameters need to be defined beforehand in the mathematical model in order to form the efficiency maps of each gear pair. The mathematical model for gear efficiency calculation is run over a variety of main parameters (i.e., speed and torque), considering the driveline limitations in order to form the gear efficiency map. By utilizing parameters that do not vary with time (e.g., the gear module, etc.), the simulation model can give instantaneous gear efficiency, based on the applied torque and operating speed, by interpolating the data from the gear efficiency map.

For continuous transmission types, for example, variable pulley diameter systems, power losses are higher than with geared transmissions [22]. In the modeling of such configurations, there are two options for efficiency calculation: having a fixed value or using an equivalently geared model. In the equivalent geared model, by defining the boundary ratios—the minimum and maximum ratio required—and the equivalent gear-pinion parameters, based on the desired accuracy, the ratio range is discretized into very small steps and the gear parameters are interpolated correspondingly.

The efficiency of components is then interpolated from readymade tables and multiplied by passing power through it. At every simulation step the required propulsion power is divided by the total efficiency of the powertrain and the cumulative power consumption is calculated accordingly. According to the block diagram shown in Figure 7, the electrical efficiency is interpolated from the electric machines efficiency map and will be multiplied by the power the vehicle demands, as well as gearbox efficiency, in order to provide the real value of extracted power from the batteries in a real-time manner. In the simulation model, the gear selection logic is based on the on the reference speed profile and between possible gear ratios, the gear in which the driveline operates in the more energy efficient situation is selected.

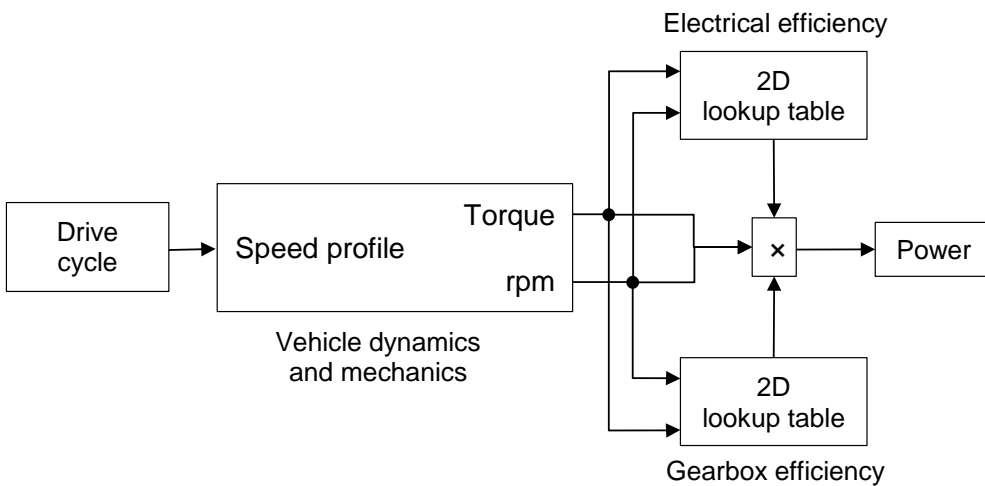


Figure 7. The layout of the EV simulation model in a block diagram.

The efficiency calculator gives the total efficiency of the powertrain at any arbitrary working point. The power consumption of different transmissions can be evaluated at the end of the driving cycle. The simulation model also enables comparison of the total efficiencies of the drivelines under study, which in this work are a single reduction gear, a five-step gearbox, and a continuously variable transmission (CVT).

2.3.2 Co-simulation utilization

In either of the automobiles classifications *on road* or *off road*, the amount of torque required to initiate movement is relatively much higher than the average in the drive cycle. If the EM is solely supposed to provide all the torque levels, then the rotor geometry must be bigger in order to be able to provide high torque at low speeds. Furthermore, the problem with a gearless vehicle is that if there is an obstacle, such as a ramp, in front of the wheel or if a tire is in a sharp pit, the torque may not be adequate when starting from

standstill. In commercial applications with unknown load data, more conservative dimensioning is preferable. On the other hand, the fault tolerance of the traction drive is high when the fault in one inverter does not prevent driving. Thus, in order to avoid big radius rotors, a speed reduction gear set is attached to the EM output to magnify the torque in low speeds. In Figure 8 the two driving modes of the integrated hub-wheel EM with a planetary gearset (InHuGOR) is described. The direct mode is when the red clutch is engaged with the sun gear and torque is delivered along the red arrow, and the reduction mode is when the blue clutch is coupled with the planet carrier and torque is conducted along the blue arrow.

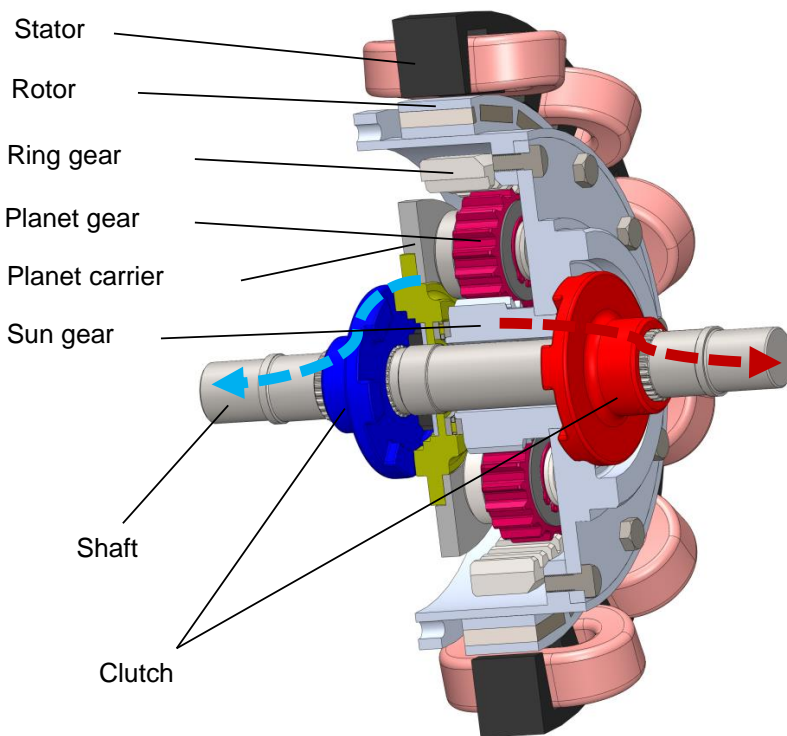


Figure 8. InHuGOR in a cutaway diagram layout.

The controllability of any kind of mechanism is vital in all kinds of systems and is the interest point of both designers and operators. In EVs and HEVs, the smooth and agile functionality of powertrains is also quite important for driveability and safety, which are highly dependent on the compatibility of one component to the other components. The proper operation and control of an integrated planetary gearset with an EM shaft that engages with dog clutch couplings in the absence of a mechanical synchronizer is a challenging task.

In order to increase the agility and accuracy of the control process, mechanical and electrical modeling and calculation is done using different software. The dynamic model of the gearbox with clutches is implemented in a multibody simulation software application (ADAMS [55]). The multibody simulation model includes the kinematical descriptions as well as the masses and mass moments of the inertias of gearbox components. The operation of clutches was described using contact force elements. The simulation model of the EM, motor controller, power electronics, and control logic of the whole system was implemented in Simulink.

The gear shifting procedure is studied using the co-simulation approach, where a detailed mechanical model, and an electric drive and control model are analyzed simultaneously. In the co-simulation, these two simulation models are combined, as illustrated in Figure 9. In the control unit, the input is the speed reference (ω) and Simulink is the master that sends selected signals to ADAMS at certain intervals. ADAMS calculates a new dynamic situation and sends defined signals back to Simulink.

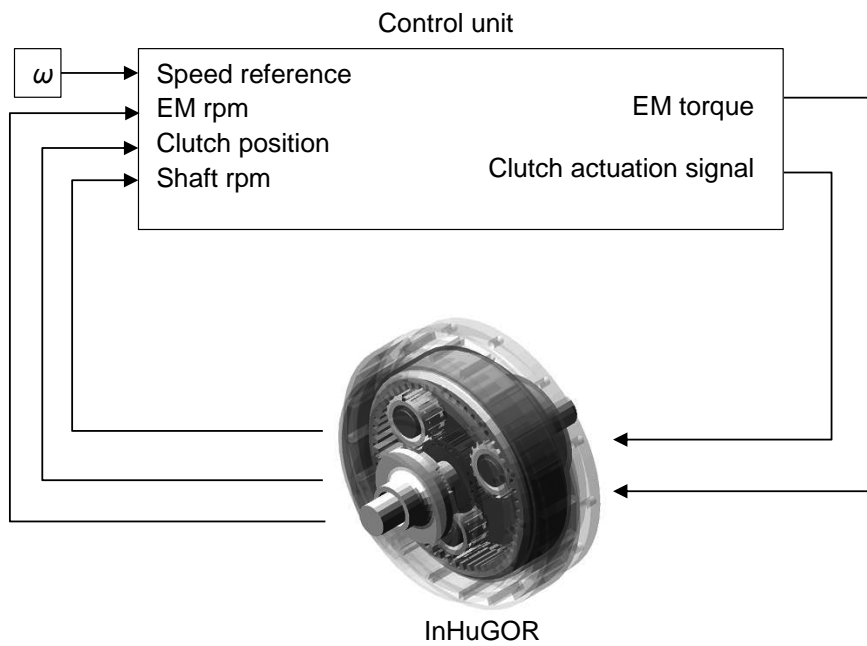


Figure 9. The principle of the co-simulation model.

Current vector control is used to control the electric machine current under inverter operational limits. Simulink will allow the usage of special algorithms, such as maximum torque per ampere control below nominal speed and the field weakening at speeds higher than the rated one. Park-Clarke transformations are used to get the most simplified two-axis model for the electric machine and its control instead of three phase quantities. The current components can be controlled as pairs inside the voltage and the current limits of

the inverter at the needed torque and speed state. In particular, below the rated speed the selection of the current component can be selected in a way which utilizes the reluctance and excitation torque of the machine in an optimal way. Electrical machine design details can be found from [56]. The more detailed information about the co-simulation technique and results can be found in the **publication II**.

2.3.3 Real-time simulation

As the final step of the design process, to observe the results of final design performance, a real-time simulator tool is applied. The real-time simulator tool not only reacts to the given inputs, but also makes it possible to measure the sent output data. The real-time simulation model can also be connected to a motion platform so that a professional driver can really test the driving conditions [57]. In the employed real-time simulator, the multibody system approach is applied for vehicle dynamics modeling. A multibody system may consist of both rigid and flexible bodies, which are connected to each other by using kinematic joint constraints while force components are used to describe the actuators. Bodies compose kinematic chains whose behavior is analyzed in simulation [58]. The simulation environment that is used in this study can also be used for simulations of multibody systems containing mechatronic components, such as hydraulics, actuators, motors, and transmissions.

As can be seen in Figure 10, all the electrical components are modeled in Simulink, while every mechanical component is modeled inside the Mevea program. The co-simulation is timed from the multibody dynamic simulation side and is synced with its time step. During this, the time step positions, orientations, and velocities of the simulated bodies are calculated. The same applies for the hydraulic system as well as mechanical powertrain values. Once in every time step, the multibody dynamic simulation sends the output values of the external interface to Simulink and waits for the return value. At this time Simulink calculates the corresponding amount of calculation loops to match the time. In this way the simulation goes hand in hand with the two programs.

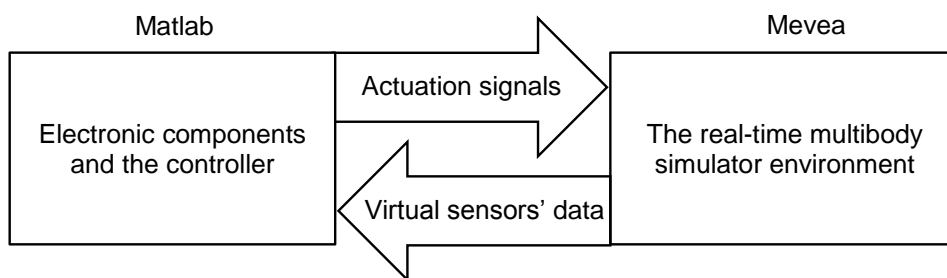


Figure 10. The interface between the Mevea simulation environment and Matlab/Simulink.

A modern software-in-loop (SIL) and hardware-in-loop (HIL) simulator was built in a cooperation of LUT, a heavy-duty electrical and hybrid electrical driveline manufacturer

(Visedo), and a simulation product provider (Mevea). In this chapter a combined (SIL) simulation approach is applied, as is a generic model that makes the different combinations of the vehicle model and simulation fast and effective. A solution for hybrid working machine system simulation is introduced. The system includes a human-machine interface (HMI) with high quality virtual reality modeling of the dynamic behavior of the mechanical components of working machines and tire friction modeling, as well as electrical drive models, including converter control. The application of the real-time simulation platform is explained in more details in **Publication III**.

3 A summary of the findings

The methods introduced in the above chapters are utilized in five study cases: a hybrid city bus (CAMBUS), an Electric RaceAbout (ERA), an integrated hub-motor drivetrain (InHuGOR), a fully electric passenger car, and an electric tractor. Analytical and numerical methods are applied to initiate the design, in which simulation tools are used to observe and validate the system's operation, comparing it to design expectations.

The above-mentioned studies are described in detail in the following compartments. In the "The initial design process" chapter, the results of CAMBUS EM rotor design is presented. In the "Lifetime calculation" chapter, the fatigue life calculation process of an ERA traction motor rotor is discussed. In the chapter "Energy consumption and efficiency", an off-line simulation tool is applied to analyze the power consumption of an EM driveline with different transmission architecture. An off-line simulation tool was also utilized to validate the functionality and controllability of an integrated planetary gearset with an electric hub-motor, which will be described in the "Electromechanical system functionality" chapter. In the "Electric tractor performance" chapter, an electric tractor driveline is benchmarked in a real-time simulation environment and its performance with different drive modes is surveyed.

3.1 The initial design process

A hybrid bus was designed and manufactured at Lappeenranta University of Technology. The combustion engine, a 2.5-liter diesel engine, rotates a generator (a 55 kW outer rotor permanent magnet generator). The traction motor is connected with a cardan shaft that runs the differential and drive shafts. In the series, hybrid, or EV modes, a mechanical coupling between the generator and the traction motor is open. In the parallel hybrid mode, the clutch is closed so that all the active components are running at the same rotational speed and can relay torque to the wheels. The parallel mode is available when the speed of the bus exceeds 20 km/h (970 min⁻¹). In the parallel mode, the generator and the traction motor are either at load or at no load. A more detailed description of the mechanical driveline, which enables multiple driving modes, can be found in **Publication V**.

The maximum traction torque needed was estimated to be 1600 Nm, while the maximum speed of 80 km/h was calculated to be 3920 min⁻¹. The maximum speed of the diesel engine, 4500 min⁻¹, is selected as the highest possible speed according to the mechanical stress analysis. At this speed, the bus should reach a speed of 92 km/h if the mechanical coupling is enabled. Typically, the maximum operating speed is about 60 km/h, and at the rated traction motor speed, the city bus runs at 45 km/h. The speed and torque requirements were also investigated for this hybrid bus application by recording an actual drive cycle of a bus route in Lappeenranta [59]. Figure 11 illustrates the data recorded on the speed profile of Bus Route 1 in Lappeenranta, a 47 km route. From the cycle it was

calculated that the torque demand is approximately 640 Nm at the rated speed of 2240 min^{-1} .

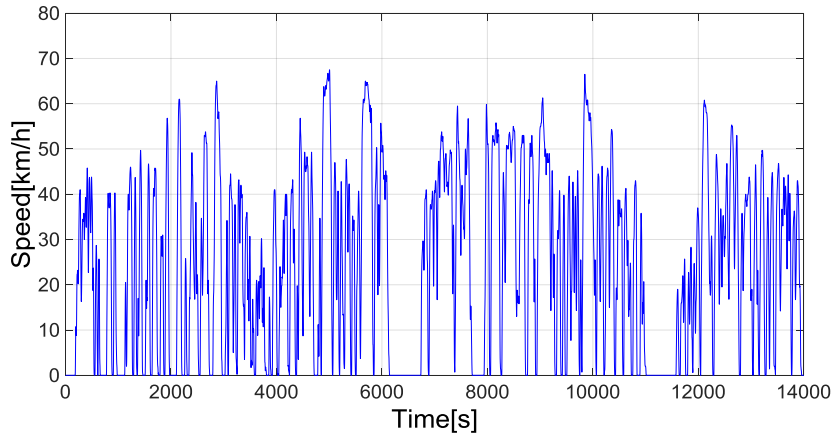


Figure 11. The speed profile of Bus Route 1 [59].

In the initial design step, several magnet volumes and their air-pocket styles are analyzed, the embedding depth of the magnets is considered, ways to increase the inductance ratio are investigated, and the mechanical stresses of the rotor are studied. From the machines studied, as can be seen in Figure 12, three of the most promising rotor designs were chosen for further analysis.

In the initial design steps, the magnet-retaining bridge was one of the optimizing targets and three different designs were initiated. The final agreement for Design A was a 5 mm thickness at the bridge midpoint and 2 mm thickness of the lateral walls. The second proposed design, Design B, with wedge-shaped slots, takes the magnets 1 mm deeper than the first design, but larger magnets are embedded in the rotor. The lateral wall thickness is 2 mm, and the outer diameter is the same. The third analyzed design, Design C, is a modified version of the second design with the same outer diameter but deeper embedded magnets, thinner lateral walls, and smaller magnets. This magnet housing offers a good path for the main magnetic flux and, at the same time, suitable mechanics that minimize the stresses. The air pockets are more complicated, and lower grooves are stretched towards the rotation axis to minimize the magnet leakage.

All of the designs are capable of carrying the required loads without reaching the yield area. The final conclusion, from the mechanical point of view, depends on how frequently the traction motor will reach 4500 rpm.

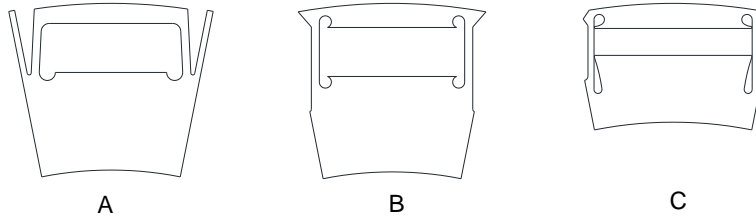


Figure 12. A comparative illustration of the initial rotor designs. More detailed geometry can be found in [60].

In the study, the stress levels caused by the combination of the tangential and centrifugal forces at different speeds were also calculated. It was observed that the stresses caused by the tangential forces are negligible compared with those caused by the centrifugal forces at high speeds. As was discussed in regard to Eq. (3), the centrifugal force, and consequently the von Mises stress, is mainly due to rotor spin, and as can be seen in Figure 13, the maximum calculated stress increases by the square of the rotational speed.

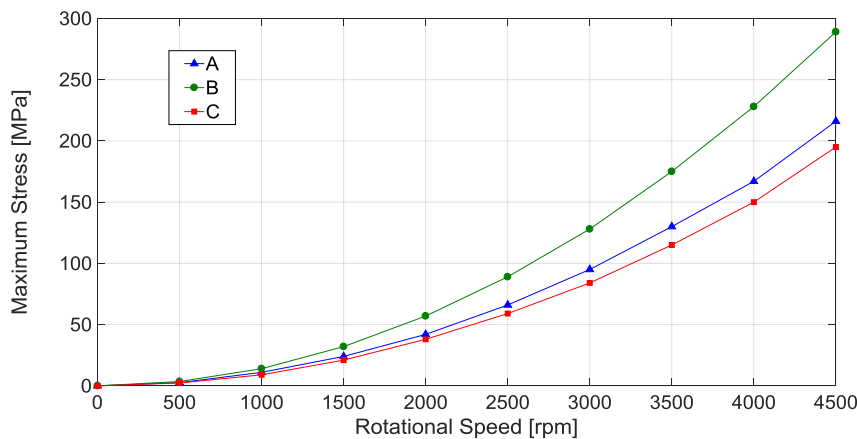


Figure 13. Maximum von Mises stresses in the rotor at rotational speed instances.

According to the rotor design parameters (detailed in Table 2), if durability is considered as the only criterion for evaluation, the Design C would be the foremost option. Considering the results of Table 2, Design C is preferential, not only because of the lower costs, but also because of the longer fatigue life.

However, for multi-criteria optimization, a selection table with weights and precise of mechanical and electrical properties, as well as material and manufacturing costs, is used. For the selection, Table 2 is proposed. Important issues are the maximum available torque, the efficiency at the rated point, and the magnet price. The other manufacturing

costs were almost the same for all rotors as the most expensive items were the neodymium magnets; their price at the time of the manufacturing (in 2014) being 175 €/kg. From the mechanical point of view, the key issues are the stresses caused by the centrifugal force and torque loads, and the fatigue life length.

In the selection table, the determinant factor in each design is divided by the corresponding mean value of all designs in order to achieve a relative index. The relative index in each criterion is then weighted based on its importance in this hybrid bus application in the Lappeenranta drive cycle.

Table 2. The rotor design parameter optimization table.

	Rotor A	Rotor B	Rotor C	Weight %
Max. torque	0.96	1.06	0.98	25 %
Efficiency at the rated point	1	1	1	20 %
Durability	0.57	0.02	2.4	25 %
Magnet cost	-1.09	-1.20	-0.71	15 %
Manufacturing cost	-0.94	-0.97	-1.08	15 %
Total score	0.28	0.14	0.78	\sum 100 %

Based on the optimization, Rotor Design C was selected, the fatigue life of which was long and which yields good electromagnetic performance and the lowest manufacturing costs (because of using the smallest amount of the expensive permanent magnet material when compared with the other rotor designs).

By finalizing the EM design step, the driveline's dynamic behavior regarding the traction motor's operational characteristics, along with other driveline components, is essential in the design process. As described above, the designed PMSM is supposed to be embedded in a hybrid city bus. The studied hybrid bus driveline is introduced and its modeling parameters for torsional analysis are described in this chapter. The first component is the 2.5 liter, five-cylinder diesel engine that operates the generator. The diesel engine and generator can be connected or disconnected from the electric traction motor by employing the magnetically actuated clutch. In fact, the clutch makes it possible to have multiple driving modes in the driveline. Driving modes are generally categorized into two main modes: series and parallel modes.

In series drive mode, the clutch between the generator and traction motor is deactivated and the drivetrain is split into two separate systems: engine-generator system and traction motor, drive shafts and tires. The engine-generator part starts to run when the battery charge level is low or when extra power is required. The traction motor transmits driving power through drivetrain components—such as the cardan shaft, rear differentials, and rear axles—to the tires. This is the most common driving mode, and supply power and

electrical excitations' harmonics are the most dominant excitations in the vibratory system.

The parallel drive mode is employed in conditions where all possible power is required by the operator; in that case, the diesel engine and EM collaborate synchronously. In addition, there is also a driving mode where only the diesel engine supplies power to the tires. This can be both feasible and the most energy-efficient driving mode in cases when the bus is driving at a constant speed on the highway (at speeds from 60 km/h to 80 km/h). In that case, it is neither feasible nor efficient to convert mechanical energy into electrical energy and consume it in the traction motor. In this case the produced torque from the diesel engine is transmitted to the tires by means of electric machine shafts while there is no electric torque interference. In a direct drive, all the driveline components, from beginning to end, are carrying the load and a long multi-material shaft including a coupling is the transmitting axle. This driving mode could be also used in the situation where all the batteries are depleted.

The results of the torsional analysis are shown in *Chapter 3*. As in the design stage, the torsional vibration analysis has some uncertainties. In order to validate the design's robustness and to find the weak points of the system, a parametric sensitivity analysis is performed (i.e., several cases with different parameters are analyzed). Parameter variations are based on the error estimates of the model input data.

The layout of the CAMBUS driveline's active components is shown in Figure 14a. According to [61], the drive train can be adequately modeled with as few elements as just the bar and mass elements. As shown in the illustration of discretized FE (Figure 14b), defining the input variables in a rotor-bearing dynamics (RoBeDyn) analysis tool is done by discretizing the driveline into stiffness and mass elements. In the driveline, the components having parts that do not bear any torsional forces are modeled in two steps. The part of the component that carries the torsional load is modeled as a shaft and the portion that only imposes inertia around the axis is modeled as a mass element. By having the material-inherent properties, the mass moment of inertia and torsional stiffness of elements are calculated by the element's inner and outer diameter [62].

The numerical analysis of the driveline's torsional vibration is done by computer software [63], using the FEM. Applying the in-house RoBeDyn toolbox enables the visualization of the elements and mode shape graphs through the transparent 3D model of the system. It helps to diagnose the modal variation with its correspondent nodes in the drivetrain in order to modify the points that cause resonance in the system.

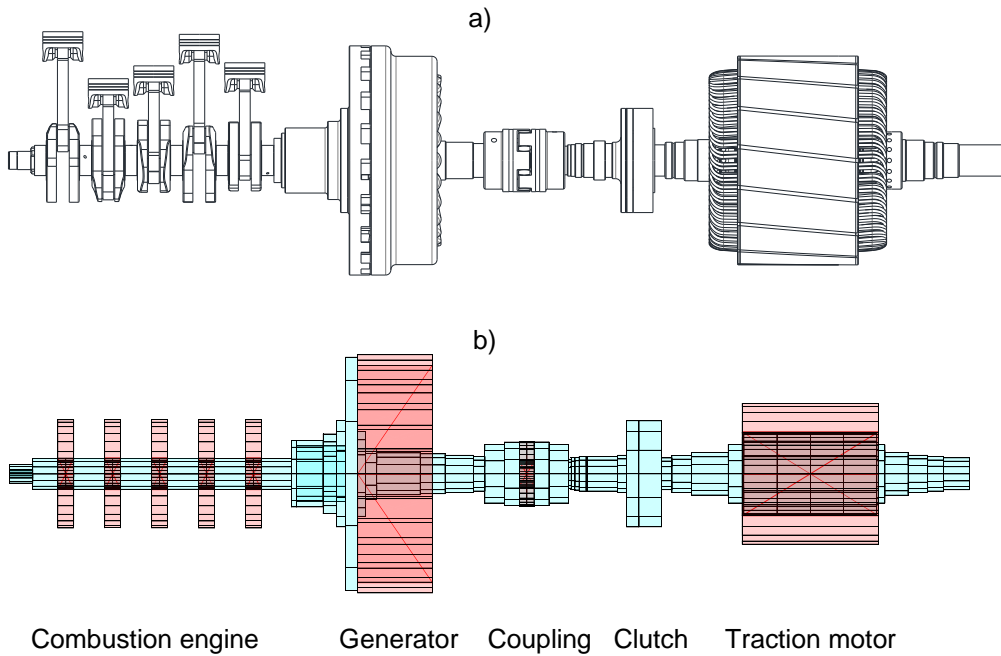


Figure 14. a) The CAMBUS hybrid powertrain layout: a combustion engine, a 55 kW outer rotor PM generator, the coupling, a clutch, and a 150 kW permanent magnet traction motor. b) A visualization of FE discretization of the CAMBUS driveline.

The first two studied cases are the open and closed clutch conditions with the nominal driveline parameters. The three lowest torsional natural frequencies and mode shapes in these cases are shown in Figure 15 and Figure 16. Open clutch conditions correspond to the serial driving mode, while the closed clutch configuration is active in the parallel or diesel-only driving mode. The natural frequencies are higher in the series drive mode, as was expected since the drivetrain is split into two parts in this mode. By studying the mode shapes, it can be seen that the tires which carry the bus load behave as fixed ends, and the largest deformation occurs either in the traction motor or in the diesel engine.

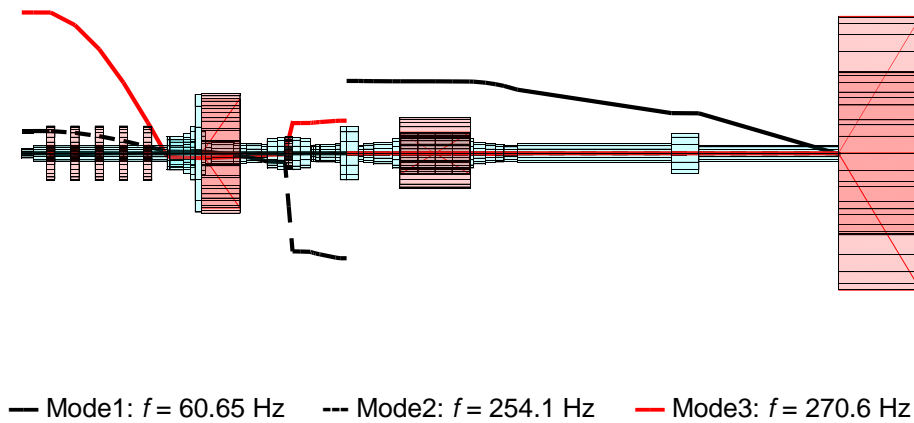


Figure 15. The driveline's basic model in *open clutch* status.

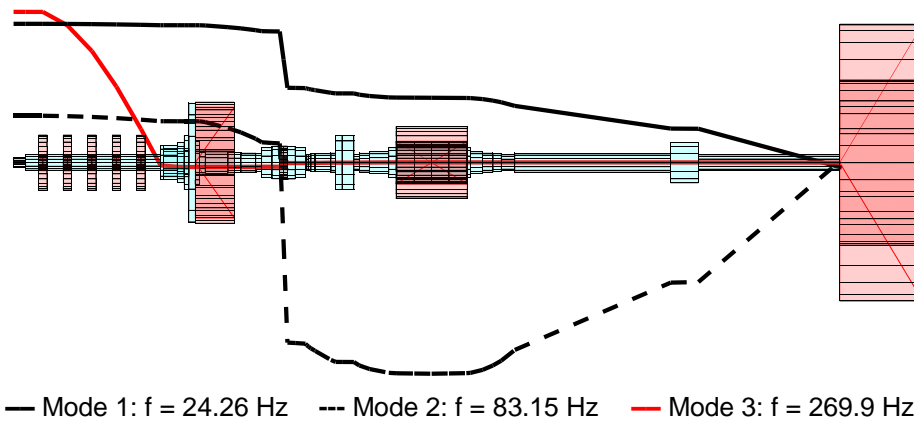


Figure 16. The driveline's basic model in *closed clutch* status.

The sensitivity analysis is conducted by varying the model parameters that have uncertainties. The selected variations are: the diesel engine's inertia, the stiffness of the hub joint between the engine and generator, the coupling's stiffness and inertia, and the traction motor's inertia modeling.

Regarding the calculated frequencies for the different study cases in **Publication I**, the system is robust at low speeds, since the first natural frequency stayed almost constant, even when the assumptions were modified. From the studied cases, it can be concluded that the system is sensitive to coupling stiffness in the second mode.

Engine harmonics are graphically shown together with the system's overall three lowest natural frequencies in Figure 17. The purpose of this diagram is to visualize and detect the possible resonance operation speeds. At present, it only displays the frequencies of five harmonic components ($i = 0.5 \dots 2.5$), but more can easily be added [64, 65].

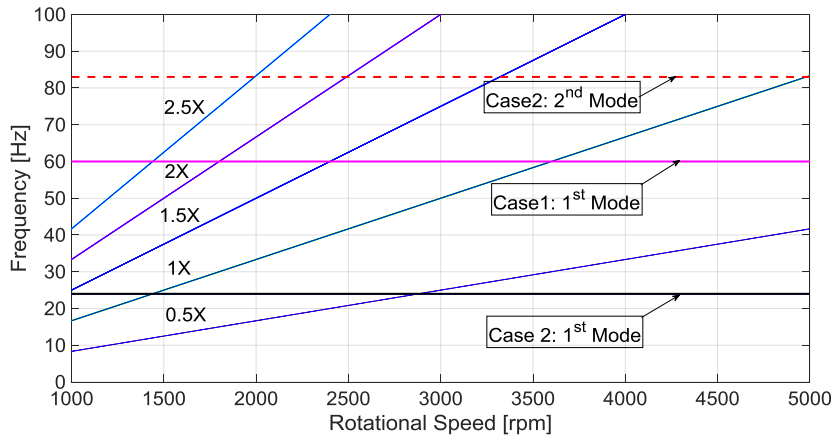


Figure 17. A frequency interference diagram showing the first five harmonic components of engine rotational speed.

The torsional excitations of the studied driveline arise from two different sources. The reciprocating diesel engine causes engine harmonics, and electrical machines cause torque ripple and cogging torque harmonics. The excitation frequencies are discussed in **Publication I**; however, a detailed forced response analysis is left for future studies

3.2 Lifetime calculation

The life span of the designed driveline is dependent on the structure material properties and operational situation and pattern. However at the initial steps of design process, ultimate and harsh situations with a magnification factor are modeled to avoid failure in the structure; operational conditions and operator manner can affect the life span. In this dissertation, the fatigue life of the EM rotor is studied in two different applications of electric and hybrid drivelines (in city bus transportation and in a high-performance sport car) by taking into account the phenomena that aggregate overloads in the structure.

The first study is of a hybrid city bus's EM rotor. There are three rotor designs that are subjected to fatigue life study. The calculated equivalent stress cycles, $\Delta\sigma_{eq}$, and the number of cycles, N_f for Designs A, B, and C, considered over the driving cycle depicted in Figure 11, are given in Table 3.

Table 3. Fatigue life results for the Lappeenranta Bus Route 1 driving cycle.

	Rotor A	Rotor B	Rotor C
$\Delta\sigma_{eq}$ (MPa)	293	440	252
N_f (cycles)	4×10^6	6×10^6	20×10^6
Life cycle (km)	5.3×10^{12}	5.4×10^{10}	6.4×10^{13}

To validate the design's fatigue life for a standard drive cycle, rather than the recorded drive cycle on the local track, a fatigue study was also conducted also for the New European Driving Cycle (NEDC). It should be noted that the NEDC is a very smooth drive cycle that is usually performed on a flat road, in the absence of wind and or traffic jam and may not cover all the real-life driving conditions. Here it is taken to demonstrate modeling methods and used as a commonly known benchmark to compare different results. Since the maximum speed of the bus is 92 km/h, the low-powered vehicle cycle is applied to the Extra Urban Driving Cycle [66]. Figure 18 shows the NEDC_{LP} speed profiles; it can be seen that the maximum speed is higher than on Lappeenranta Bus Route 1.

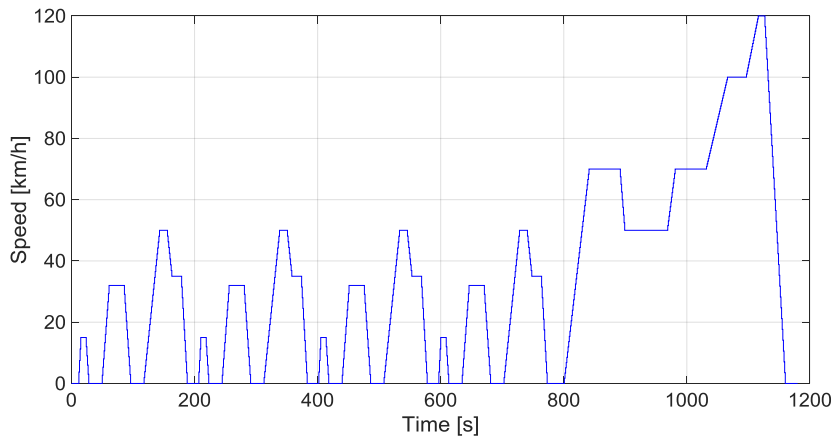


Figure 18. The NEDC speed profile for the low-powered vehicle cycle [67].

The fatigue analysis results for the NEDC drive cycle are shown in Table 4. It can be pointed out that the number of cycles and drivability values are equal as the NEDC_{LP} length, 994 m, which is very close to one kilometer.

In the second case study, a high-performance sport car was studied. In this case, rapid acceleration and the elevation of the electric current rate in the stator windings cause temperature gradient fluctuation in the rotor, thus stresses due to thermal loads needed to be considered while calculating fatigue life.

Table 4. Fatigue analysis results for NEDC_{LP}.

	Rotor A	Rotor B	Rotor C
$\Delta\sigma_{eq}$ (MPa)	224	304	194
N_f (cycle)	71×10^6	2.8×10^6	3×10^6
Life cycle (km)	7.1×10^7	2.8×10^6	3.1×10^8

The FEM is applied to calculate the thermomechanical stress level for transient analysis, and measured data from the rear right (RR) wheel of ERA on the Nürburgring Nordschleife track is taken as a load history pattern. As can be seen in Figure 19, the drive cycle of ERA on the track is recorded and by employing the FE results and measured data, the fatigue life of the rotor is calculated. In the case when the stress level is in the allowable range but the fatigue life is shorter than the designed life cycle, the geometry of magnet housing can be modified accordingly.

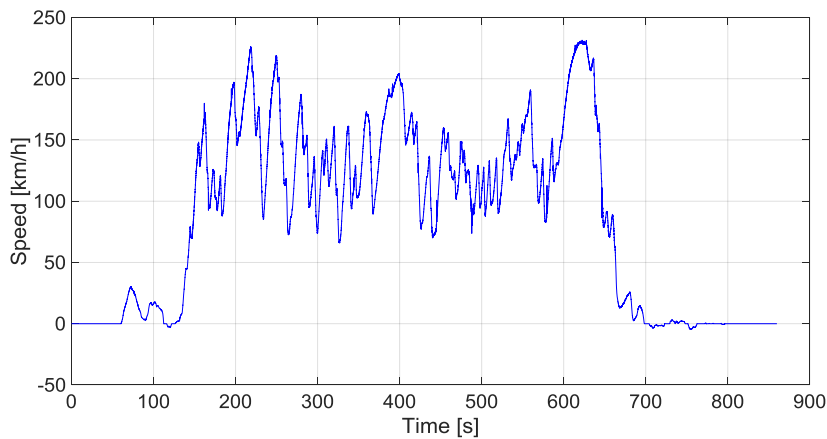


Figure 19. The ERA speed profile on the Nürburgring Nordschleife track.

Figure 20 shows the studied rotor assembly that is part of the three-phase 8-pole double deck embedded permanent magnet motor for a 4×4 fully electric race car ERA. The FE model of the rotor was built in Ansys.



Figure 20. ERA's EM rotor's assembly.

The lamination bridges around the magnets shown in Figure 21 are designed to be mechanically durable at the expense of electromagnetic performance due to design requirements. Consequently, a low level of mechanical stresses and long fatigue life are expected.

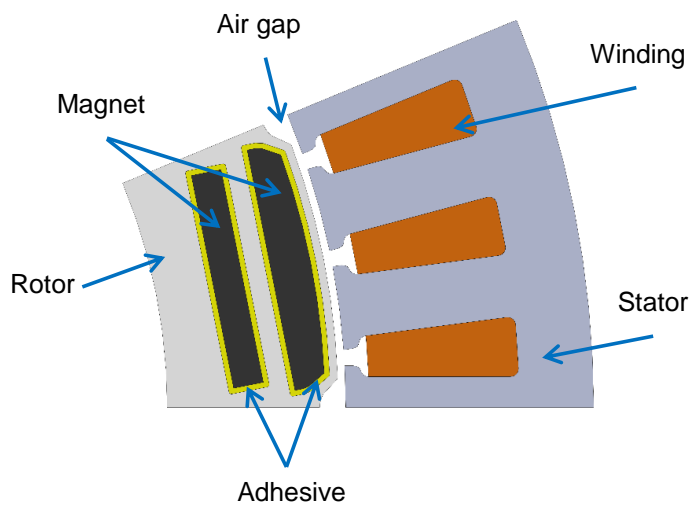


Figure 21. The structure of one pole of the designed PMSM.

In the FE study, a 1/16 slice of real rotor stack with cyclic symmetric constraints around the main axis is modeled in order to simplify the model and reduce calculation time. Heat losses as functions of current are added to both lower and upper magnets and iron losses for rotor laminations. Heat convection boundary conditions are added on the rotor sides

and the air gap in order to simulate real conditions and the ambient temperature is set to 22°C. Cooling of the PMSMs is carried out by combining air cooling in the air gap region and liquid cooling in the stator frame. A transient thermal study is run for a 530 second drive cycle at one-second time increments and the corresponding stresses are transferred to a transient mechanical study as preliminary stress. In the mechanical study, besides the imported thermal loads from the previous study, the measured torque and rotation speed that were measured from track test are added to the model.

As a result of stress calculation, according to the stress distribution as it is shown in Figure 22, the critical areas are the magnet pocket upper fillets. Furthermore, the magnetic flux is denser around the air barriers in the magnet housing, thus more eddy currents are induced there and it heats up faster. This stress parallax raises the importance of thermal influence in stress analysis.

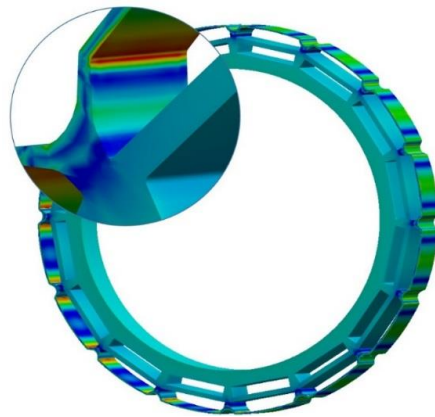


Figure 22. Critical areas are shown in red—areas where maximum stress appeared during the Nürburgring test drive.

Figure 23 shows the measured temperature from the windings [15] and the calculated temperature in the area of the highest stresses in the rotor-critical area. The scale of the temperatures is clearly different since the temperature of the windings rises up to 145°C and the temperature of the rotor up to 40°C. Even though the temperatures are obtained from the different locations, the trends of the curves are comparable. The calculated temperature increases relatively faster between 70 and 100 seconds. After the first 100 seconds, the temperature in the rotor core increases relatively slower than in the windings until time point of 240 seconds, when it starts to increase again relatively faster than the temperature in the windings. Then, after 40 seconds, at time point 280 seconds, it starts to increase relatively slower until the final rush, just before the end of the cycle. In **Publication VI** the calculation process and FEM modeling is explained in detail.

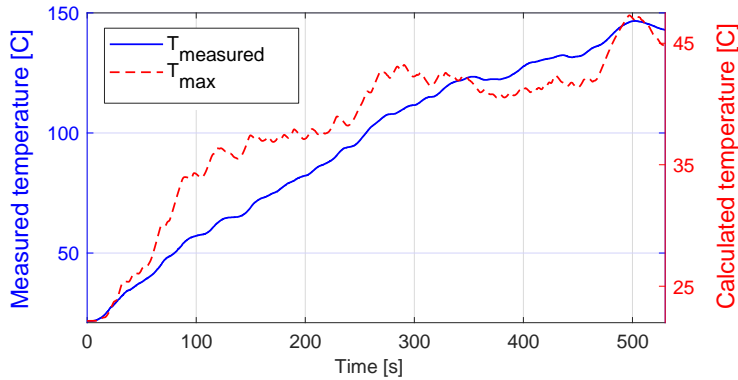


Figure 23. Measured winding temperature vs. calculated rotor temperature.

Figure 24 shows the maximum von Mises stress due to mechanical, thermal, and combined loads during the studied load cycle. The curves are sketched with a dotted black line, a dashed red line, and a solid blue line respectively. The mechanical stress strictly follows the rotational speed of the rotor. The centrifugal forces are the main contributors for the mechanical stress and the tangential forces, while torque plays a minor role. The maximum mechanical stress during the drive cycle is not more than 43 MPa.

The thermal stresses appear due to the temperature gradient along the structure. Increasing the load of the motors, the losses around the magnets increases, which further causes a higher temperature gradient. The time spans in which the structure experiences faster heat increase (70–100, 240–280, and 475–500 seconds), and the thermal stresses increase faster as well. Between the higher temperatures rising when the temperature is increasing more steadily, the structure heats up more steadily, resulting in a lower temperature gradient and a hardly noticeable increase in thermal stress levels.

To conclude regarding the behavior of the mechanical and the thermal stresses solely, the loading of the motors increases both stress types. However, it does not tell the whole truth if the stresses are observed separately and considering the total stress level using superposition principle by summing the stress components together. In general, Figure 24 shows that the thermal stresses increase the base level of the combined stresses and the stress variation of the combined stress curve is caused by the mechanical stresses. The comparison between the fluctuation of the mechanical stress and combined stress curves shows that the mechanical stresses by themselves experience more dramatic changes along the drive cycle, and the residual thermal stresses clearly equalize the combined stress peaks. During the studied drive cycle, the combined stress levels are lower than the thermal stress levels. Figure 24 shows that thermal and mechanical strain, regarding direction, may negate each other or amplify the overall strain and combined stress consequently. Therefore, using the superposition principle in evaluating the stress levels from the mechanical and the thermal stresses dramatically overestimates the stresses and results in a too conservative design.

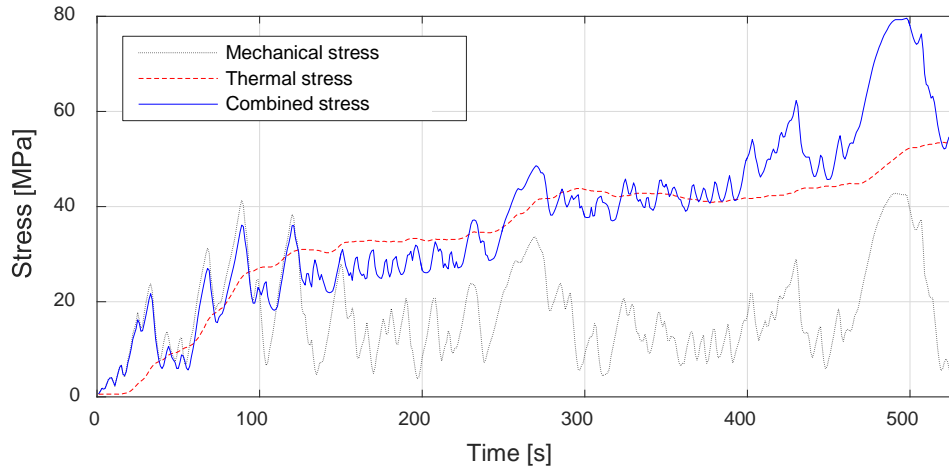


Figure 24. The von Mises stress history in different loading conditions: mechanical load, thermal load, and combined load.

Based on the published fatigue test results for similar rotor laminate material in [68], the following fatigue strength coefficient and fatigue strength exponent are adopted in this study: $\sigma'_f = 673.25$ MPa and $b = -0.09559$.

The plot of stress (S) against the number of cycles to failure (N) of electrical steel (M270–50A) is shown in Figure 25. Forming the S–N curve needs to take into account various parameters, such as the aspect ratio, temperature, and influences on the surface condition. The S–N curve is the foundation for a fatigue assessment on the basis of the load spectrum.

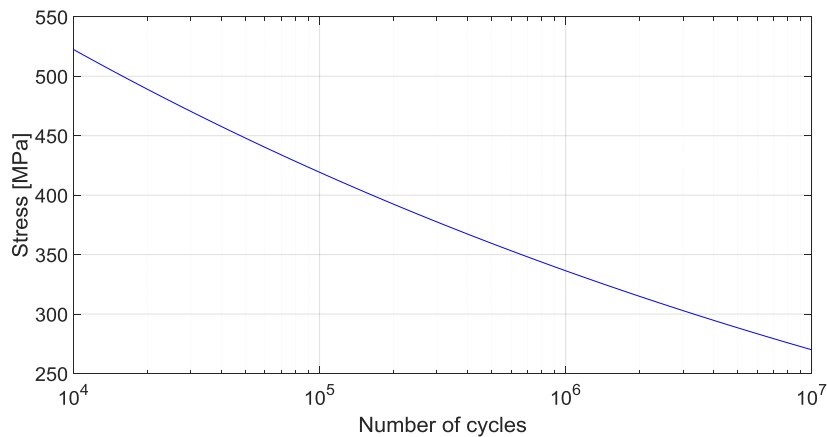


Figure 25. The S–N curve of electrical steel M270–50 A.

A comparison between the maximum stresses in the drive cycle, maximum stress σ_{\max} , and the equivalent stresses σ_{eq} —caused by mechanical, thermal, and combined loads—calculated for the fatigue study are illustrated in a bar chart (Figure 26). As can be seen in the bar chart, the maximum thermal stress is higher than mechanical stress, while the equivalent mechanical stress is higher than the equivalent thermal stress. This contrast is because of the amplitude and number of stress fluctuation instances. As can be seen in Figure 24, mechanical stress's inclination trend is rapid, while thermal stress increases quiet smoothly.

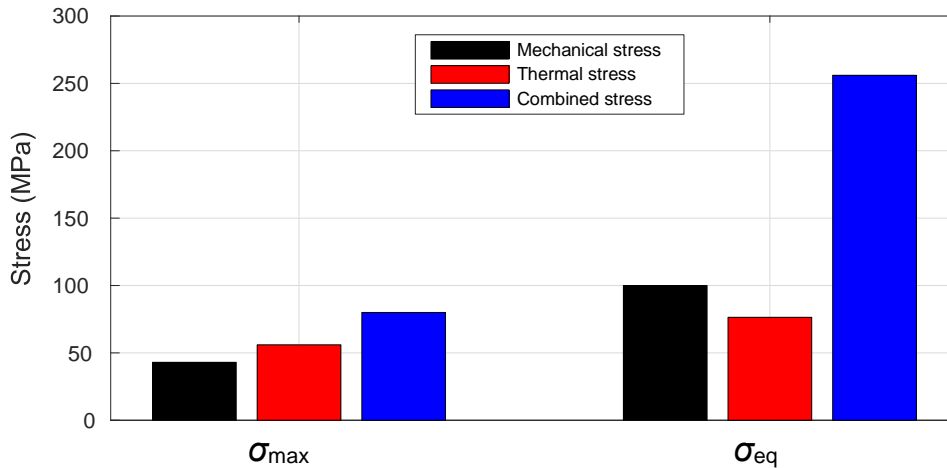


Figure 26. A stress level comparison bar chart in the ERA rotor.

The results show a significant change in both stress levels and in the predicted fatigue life, depending on if the thermal stresses are accounted for or not. In the studied traction motor, the total stresses are on an acceptable level, even when the thermal stresses are included. This is due to the conservative approach adopted in the design process, but it should be mentioned that the mechanical durability of the rotor was increased by sacrificing some portion of the electromagnetic performance. Therefore, a comprehensive thermomechanical analysis is essential for a precise and optimal design. This can be accomplished by employing the procedure proposed in this dissertation.

3.3 Energy consumption and efficiency

In this section a simulation tool is utilized as a tool to benchmark the efficiency of electric drivelines. The results regarding the power consumption efficiency of an electric passenger car are presented in this chapter.

The presented transmission model was run and archived for the gear pairs that are used in the vehicle model over the EM operation points (i.e., 0 to 10 000 rpm and -350 Nm to +350 Nm). The obtained transmission efficiency data were then embedded into the corresponding vehicle model in order to derive the efficiency at any arbitrary power point.

Because of difference in European and US driving patterns, the simulation model was run for two different driving cycles in order to validate the compatibility of the model with both the NEDC and the American Federal Test Procedure (FTP-75). The Speed profile of the NEDC and FTP-75 are shown in Figure 27.

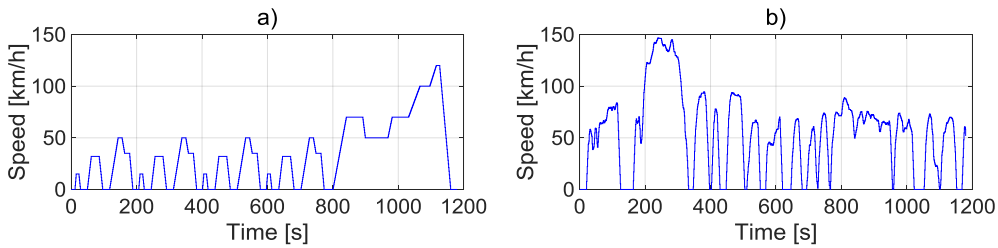


Figure 27. The driving cycle profile of a) the NEDC b) FTP-75.

The power required for the driving cycle is given in the EM-generator efficiency map (η_E) for the single reduction gear, for the five-step gearbox, and for a CVT in Figure 28a, Figure 28b, and Figure 28c respectively. Applying FTP-75, the energy consumption seems to be similar in the five-step gearbox and CVT, but the single gear transmission exhibits a clear difference. The EM-generator operation points over the EM efficiency map for FTP-75 can be found in **Publication IV**.

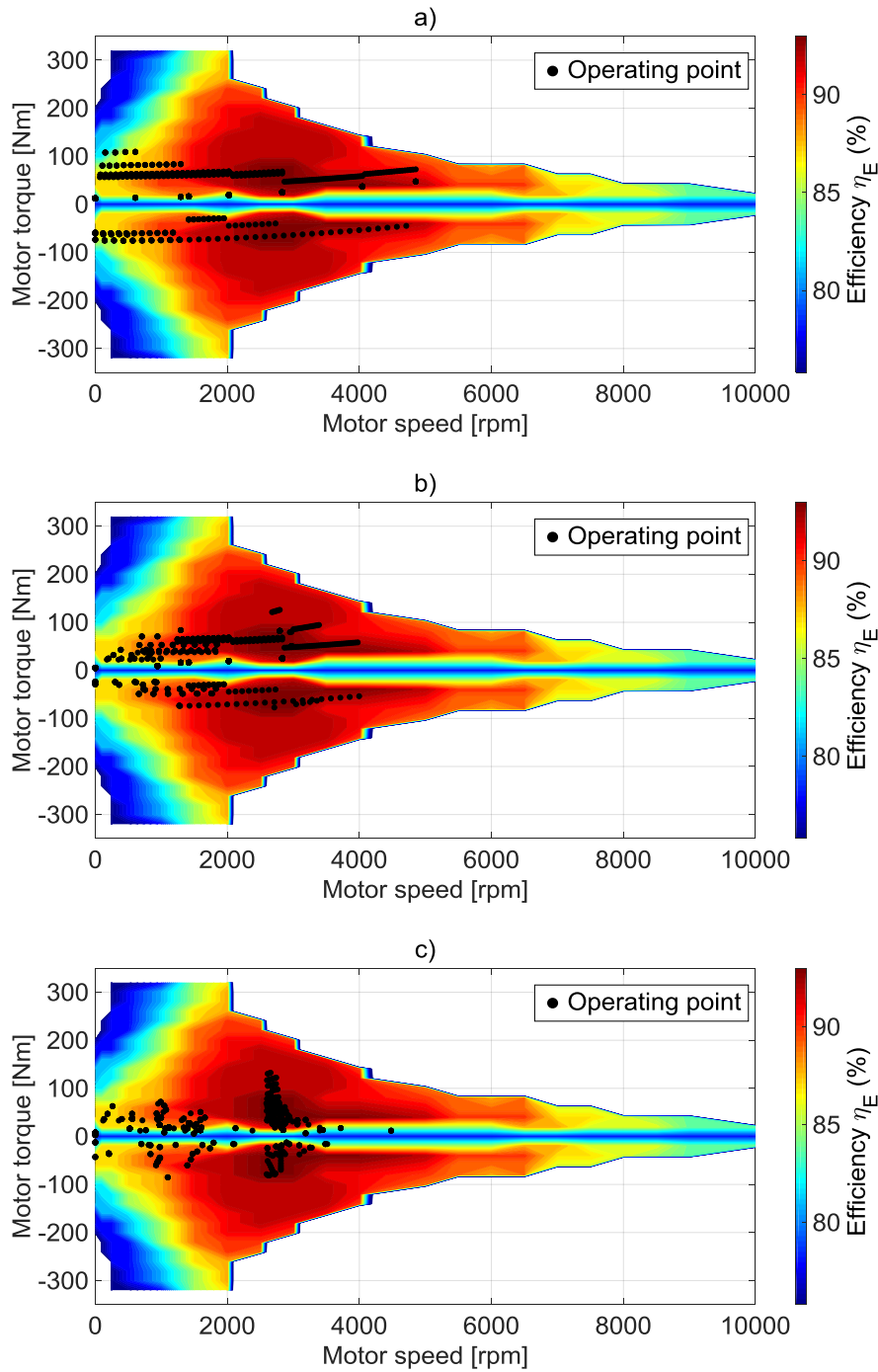


Figure 28. The operating points of EM during the NEDC over the electric motor-generator efficiency map (η_E) with a) a single reduction gear, b) a five-step gearbox, and c) a CVT.

It should be mentioned that the EM operation map is plotted in nominal condition, whereas the maximum output power is almost double the nominal power. However, there are some operation points (specifically for the FTP-75 drive cycle) that are off the map in Figure 28, but it does not mean that the EM is not capable of producing the corresponding power. The correlating efficiency is also calculated by extrapolating the given values from the nominal operation range. However the cumulative energy consumption in all three drivetrain architectures seems to be similar in Figure 29; in the magnified scope, a minor difference can be seen that shows the single reduction gear design depletes batteries more than the other drivetrain designs.

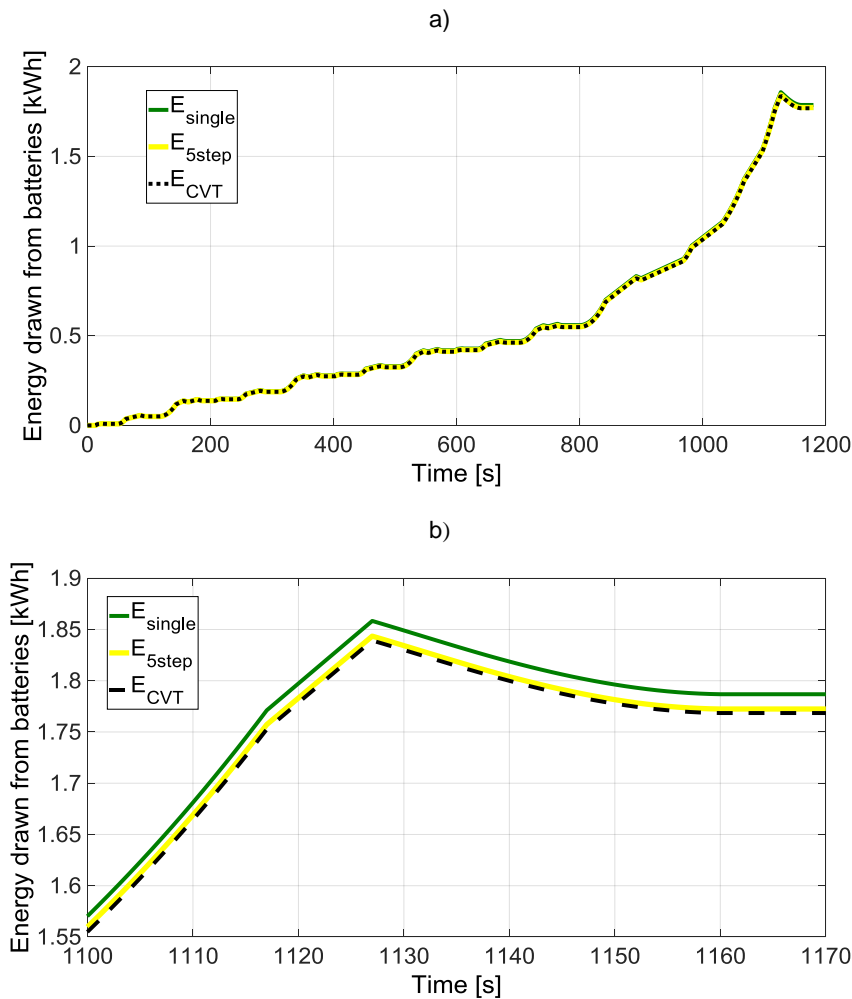


Figure 29. a) Cumulative energy consumption during the NEDC with a single reduction gear (E_{single}), a five-step gearbox (E_{5step}), and a CVT (E_{CVT}). b) Zoomed scope.

Comparing the cumulative power consumption curve (shown in Figure 30) and driving cycle fluctuation (shown in Figure 27), it can be seen that at high speeds the low efficiency of a single reduction gear causes higher power consumption.

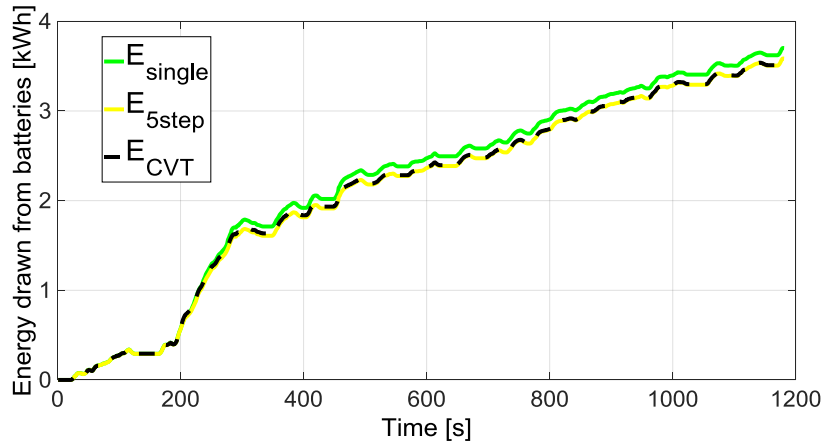


Figure 30. Cumulative energy consumption during FTP-75 with a single reduction gear, a five-step gearbox, and a CVT.

The simulation model was run in both an ideal situation, where the efficiency of the non-electrical components was set to 100 percent, and in realistic situations, for which the proposed model was employed to calculate the power losses due to mechanical components (e.g., transmission). The simulation results for ideal transmissions indicated that the trip range of an EV in which a CVT is embedded improves by 2.5% for the NEDC and 3% for FTP-75 compared to a single reduction gear. The EV equipped with a five-step manual transmission has a trip range improved by 1.5% and 3% for the NEDC and FTP-57 driving cycle respectively. In order to illustrate the contrast in energy consumption levels across different driving cycles and transmission configurations in both ideal and real situations, the results are plotted as a bar chart in Figure 31.

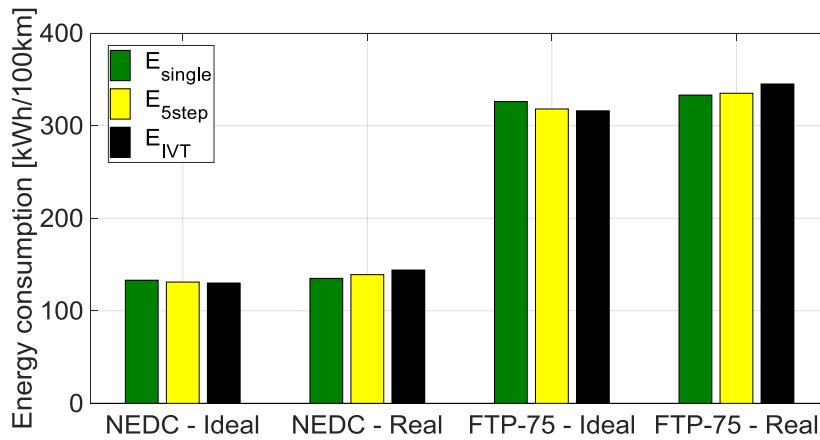


Figure 31. An EV energy consumption comparison bar chart.

However, although the CVT seems to be a better option than a single reduction gear in an ideal situation, in realistic conditions, when the gearbox power losses are taken into account, the efficiency of the driveline drops by 6.6% for the NEDC and 3.6% for FTP-75. As can be seen from Figure 31, in the real situations, the power consumption increases as the driveline architecture gets more complicated. The reason for the simulation with a CVT resulting in higher energy consumption in both the NEDC and FTP-75 (as can be seen in Figure 31) is that the mechanical power losses in a CVT are relatively higher and will cancel out the achieved improvement in electrical efficiency. Even though the results vary for different driving cycles and gear ratio selections, this simulation shows that with equivalent settings, extra component power losses outweigh any downstream efficiency gained by the more efficient operation of the EM.

3.4 The validation of the functionality of electromechanical systems

In this section the dynamic behavior of an integrated planetary gear with a PMSM during gear shifting is studied by using multibody system simulation software (ADAMS). As is explained in the upper compartment of Figure 8, the direct mode happens when the output shaft is connected to the sun gear and the rotor consequently by the the red dig clutch, and the reduction mode is when the planet carrier delivers the torque via the blue dog clutch to the drive shaft. The main focus is to observe the proper functioning and check the controllability of gear shifting, which is a determinant factor in the duty life of the driveline. The duty cycle for the simulation is summarized in accelerating, operating in a constant speed, and shifting. Since the gear shifting process should be carried out in a small time period, any failure in the synchronization of the rotor and clutches leads to severe shocks and vibration that may consequently lead to the fatigue or fracture of the mechanical components. The multibody simulation approach is used to verify the

functionality of the dog clutch shifting mechanism in an integrated electric hub motor and a planetary gearset, as well to verify its performance in a tractor for the dynamic analysis of the electric driveline and vehicle.

The simulation is run for 4 seconds and there is interaction between Simulink and the mechanical plant in ADAMS every 10 microseconds. According to the defined sample drive cycle, three shifting signals are sent to clutches and, as shown in Figure 32, in every disengagement there is an overshoot in the sun gear rotational speed that illustrates that the rotor speed increases dramatically when it is unloaded immediately. So, the EM control should be modified to set the torque to zero before sending gear shifting signals to the clutches, which not only decreases the tooth clutch sliding friction but also prevents immense shocks to the system.

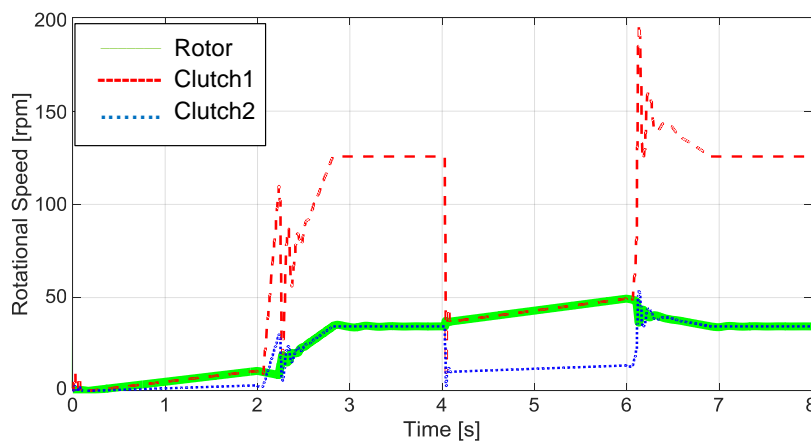


Figure 32. Three-gear shifting in the sample drive cycle.

In this study, the functionality of the gear shifting procedure of a novel two-step gearbox integrated with an electric hub motor (**Publication II**) was validated using a co-simulation approach where a detailed mechanical model, and an electric drive and a control model are surveyed simultaneously. The main result of this study was discovering that it is possible to perform gear shifting as planned; however, electric synchronization and control play a significant role.

3.5 Electric tractor performance

After the functionality of gear shifting is validated, a simulation model of an electric tractor that utilizes four integrated electric hub motors was developed to observe its performance in real application. In this study a real-time simulator was used as a virtual dynamometer and an electric tractor was taken as a sample to compare the power consumption between two different driveline configurations; the first one comprises two

double-powered InHuGORs in rear wheels and the second one has a InHuGOR drive in all four wheels.

The latter driveline model, which is rear-wheel drive (RWD), consists of two InHuGORs mounted on the rear wheels with double-rated power, providing the same total accessible power as a four-wheel hub-motor. Some minor simplifications are applied in modeling the double-power InHuGORs—such as rotor mass and EM efficiency—that do not have a considerable effect on results. The rotor mass is negligible compared to wheel complex mass, and full throttle operation efficiency is almost the same in a double-powered EM. The simulation track is dry asphalt and the tire dynamic friction coefficient is set to 0.8. In the initial moments that the model is created in the simulator environment, it has some initial speed in the opposite direction of the track. That is why at around the first second of the simulation, the speed value is negative in Figure 33. However the top speed in this simulation is 115 km/h, which may not be suitable for tractors, the results can be utilized for other vehicles types.

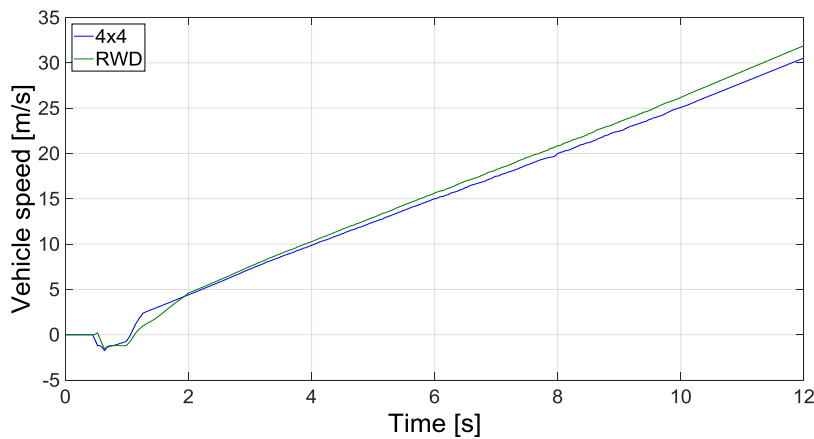


Figure 33. The vehicle's longitudinal speed for two different drivelines.

According to the rear and front tires radii and widths, chassis geometry, and the center of mass location (which is 10% inclined to the rear), the normal force at tire contact and the rolling friction of rear tires are higher than front tires eventually. The effect of that can be seen in Figure 33 where the vehicle's longitudinal speed with a RWD driveline is higher than the 4x4 model, whereas the acceleration is pretty much the same and this is because of the initial tire slipping in 4x4 mode. The instant power consumption of EMs on each wheel [front-left (FL) wheel, front-right (FR) wheel, rear-left (RL) wheel, and rear-right (RR) wheel] are plotted in Figure 34 for both proposed drivelines. Comparing plots *a* and *b* in Figure 34, it can be seen that the cumulative power consumption is almost the same for either 4x4 drive or RWD, but the tire slipping duration is double in RWD because of two times higher power of the EMs in this mode. More detailed information about the electric agricultural driveline architecture can be found in **Publication III**.

In Figure 34 the instant power consumption on each wheel is illustrated. In Figure 34b, the power consumption on the RR and RL wheels is slightly higher and that is because less slippage of the rear wheels leads to more electric power consumption than the front wheels, which can pivot with less resistive force.

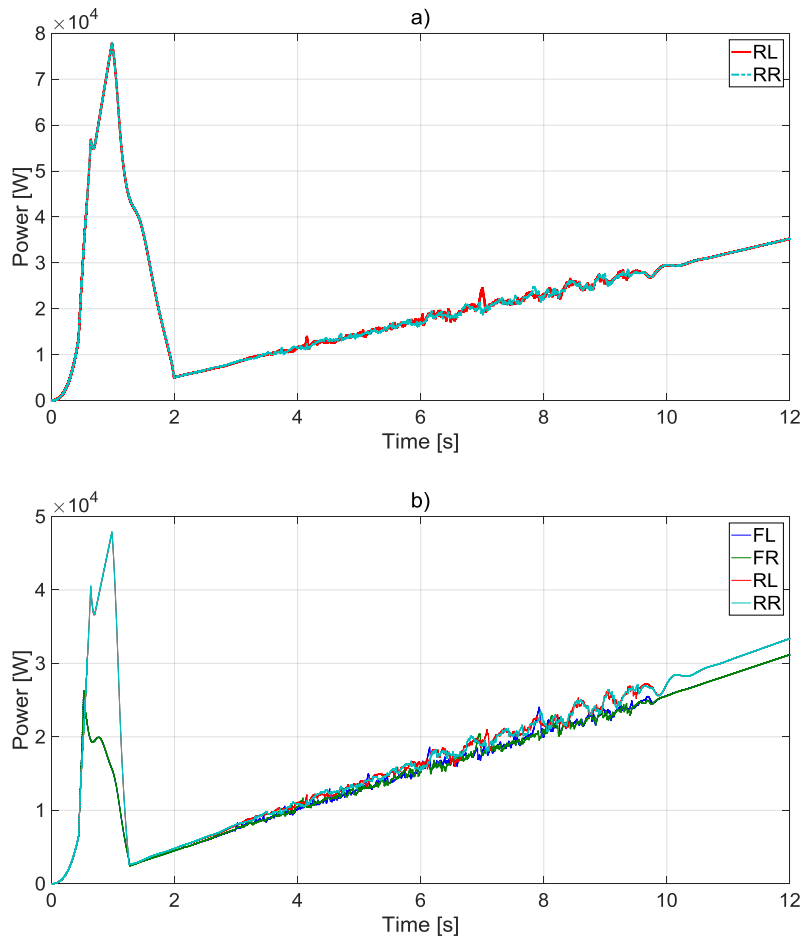


Figure 34. Instant power consumption on wheels: a) RWD, b) four-wheel drive.

The total power consumption of the modeled tractors are calculated according to the torque on wheels and the drive shaft speed, and are printed in Table 5. Regarding the power consumption plots, the necessity for an efficient traction control system is sensed. According to the results in Table 5, the total energy efficiency of the RWD driveline is still better than that of the proposed 4×4 driveline, while there is no mechanical differential that imposes extra power loss to the system without an effective traction control that prevents spinning of tires.

Table 5. The power consumption of vehicle wheels (kWh).

Wheel	4x4	RWD
Front-Left	0.9323	-
Front-Right	0.9293	-
Rear-Left	1.0270	1.2319
Rear-Right	1.0280	1.2323
Total	3.9166	2.4643

The simulation process is functionalized by using a Mevea and Matlab/Simulink interface. The EM is calculated inside the Matlab script and only torque and rotational speeds are inside the Simulink model. This makes the simulation process faster, for example when inductances, flux linkages, and currents are inside the script and Simulink only uses efficiency maps. All the other electrical components are handled in the same way.

4 Conclusion

The importance of EVs and their benefits over conventional vehicles are explained and a methodology for driveline design for EVs and HEVs for a passenger car, a city bus, a racing car, and a tractor in on-road and off-road applications is developed in this dissertation. In this methodology, a comprehensive approach to different fields of mechanical engineering and electrical engineering is taken and different scientific methods and techniques are utilized to form a multidisciplinary guideline for the EV driveline mechanical design.

So far, various combinations of EMs and a combustion engines have been formed to make hybrid drivelines, but synchronous operation of a diesel engine, a generator, and an EM mounted on a common shaft is the novel hybrid driveline solution that is analyzed in this dissertation. The electromagnetic efficiency and mechanical strength of the initial geometrical designs are later evaluated for an optimum final production. The application of such a driveline in a city bus requires precise evaluation of every single component in order to avoid failure due to torsional vibration. Hence, an analytical model of driveline components is developed as well as numerical model, that is, FEM, to calculate the driveline torsional natural frequencies and excitation frequencies generated by a five-cylinder diesel engine and electric machines in order to find out the probability of torsional resonances in the system. More than a hundred cases with a smart combination of driveline components with higher and lower mass and stiffness values were carried out to analyze the sensitivity of the driveline to uncertainties during the FE modeling. By analyzing the torsional mode shapes in basic model simulation, the critical components are spotted and the critical operation ranges of the diesel engine are detected.

In a high-performance EV like ERA, because of rapid temperature inclination, thermal stress can cause early wear and malfunction. To study the effect of thermal and mechanical stress on the EM's lifespan, the FEM is applied to calculate the thermomechanical stress history over the load cycle and then outcomes are subjected to analytical fatigue life calculation. The results show that thermal loads may dampen or amplify the mechanical loads regarding the load direction. Thus, considering thermal stress along with mechanical stress is essential when calculating the lifecycle. Comparing the hybrid city bus's operational situation and the ERA driving pattern shows that in a low-performance application, with smooth acceleration and deceleration, and steady thermal condition, modeling the centrifugal load as the main stress source as a function of rotational speed, gives a straightforward solution to the stress history. Whereas in a high-performance application in which sudden change in operational condition leads to rapid temperature escalation, a more detailed and transient thermodynamic analysis is required for obtaining temperature variation and consequently thermal stress. Considering both thermal and mechanical strain, the stress history of the EM in high-performance status is calculated and finally the life span of the EM is calculated.

The feasibility of applying variable transmission versus a single reduction gear in pure EVs has been one of the concerns of EV driveline designers. The efficient solutions are

mostly compromised to improve the performance of EVs, so a new bilateral approach that considered both the electrical and mechanical efficiency of the EV was developed. The efficiency spectrum of an EV driveline section is analytically derived by modeling various and detailed possible power losses, and these are implemented in a simulation model to validate the driveline design feasibility from the efficiency point of view. By analyzing the final results, the most efficient solution for transmission in the EV is selected.

The design of an electric and hybrid driveline is a time-consuming process because of uncertainties about the functionality the design and its compatibility with the application. A generic and smart simulation platform is developed in this dissertation to establish a bridge between each design step and the final structure. The proposed simulation platform updates the final design with any minor modification of any design step and provides feedbacks with which to evaluate the applied changes simultaneously. In this dissertation, the operation of the clutch mechanism in an integrated hub motor with a gearbox, as well as the operation of an electric tractor consisting of four integrated hub motors with a gearbox is analyzed by the proposed simulation model. The assured functionality of the clutch mechanism and drive compatibility in the tractor driveline application promote taking further steps towards the manufacturing process.

The findings of this study cover a variety of vehicle categories (i.e., the passenger car, the public transportation bus, the racing car, and the off-road tractor). By utilizing scientific solutions to optimize the engineering method and tools, a novel approach to EV and HEV driveline design is proposed in this dissertation. Furthermore, since the simulations' results, along with prototype test outcomes, comply with all the design expectations, the proposed guidelines can be taken to be a reliable plan of action for designing EV and HEV driveline in similar applications.

4.1 Future studies

Electric mobility is expanding according to different criteria thanks to the advancements in the renewable energy harvesting methods and battery manufacturing technology. However, in order to exploit the former accomplishments and to overcome the future challenges, a systematic comprehensive approach should be taken. However, in this dissertation, an approach to electric driveline design process that considers many different aspects of mechanical and electrical characteristics is presented, yet some may have been omitted. In the following some recommendation for future studies are listed:

Electromagnetic forces, alongside thermal and mechanical loads, should be studied in order to observe the stresses due to electro-thermomechanical strain. The further development of transient thermal analysis will improve solving the electro-thermomechanical coupling problem of PMSMs.

In the torsional vibration analysis of electric and hybrid drivelines, a more reliable outcome will be achieved by considering the terrain counter load on the driveline (e.g.,

slippage and bump modeling, and empirical vibration tests and measurements on hybrid drivelines).

The limited power source in mobile and off-grid electric applications requires a precise approach in order to have a longer operation cycle, so an efficiency calculator model integrated with battery management systems will lead to more accurate results. In real-time simulations, taking into account the wear factor will help to build a more extensive model with more realistic and efficient feedbacks.

5 References

- [1] P. Pisu, K. Koprubasi, and G. Rizzoni, “Energy Management and Drivability Control Problems for Hybrid Electric Vehicles”, in *44th IEEE Conference on Decision and Control, 2005 and 2005 European Control Conference. CDC-ECC '05*, 2005, pp. 1824–1830.
- [2] *Directive (EU) 2015/2193 of the European Parliament and of the Council of 25 November 2015 on the limitation of emissions of certain pollutants into the air from medium combustion plants (Text with EEA relevance)*, vol. OJ L. 2015.
- [3] “EUR-Lex - 52013SC0528 - EN - EUR-Lex.” [Online]. Available: <http://eur-lex.europa.eu/legal-content/EN/TXT/?qid=1524658448294&uri=CELEX:52013SC0528>. [Accessed: 25-Apr-2018].
- [4] M. Meinshausen et al., “Greenhouse-gas emission targets for limiting global warming to 2 °C,” *Nature*, vol. 458, no. 7242, pp. 1158–1162, Apr. 2009.
- [5] D. Nield, “Oxford is creating a world first zero emission zone by 2035,” *ScienceAlert*. [Online]. Available: <https://www.sciencealert.com/oxford-wants-the-world-s-first-zero-emission-zone-in-place-by-2035>. [Accessed: 25 April 2018].
- [6] “German push to ban combustion-engine cars by 2030 wins support,” *Reuters*, 08-Oct-2016.
- [7] D. Matsui, “H.R.5226 – 115th Congress (2017–2018): Clean and Efficient Cars Act of 2018,” 09-Mar-2018. [Online]. Available: <https://www.congress.gov/bill/115th-congress/house-bill/5226>. [Accessed: 25-Apr-2018].
- [8] G. J. Offer, D. Howey, M. Contestabile, R. Clague, and N. P. Brandon, “Comparative analysis of battery electric, hydrogen fuel cell and hybrid vehicles in a future sustainable road transport system,” *Energy Policy*, vol. 38, no. 1, pp. 24–29, Jan. 2010.
- [9] A. Lajunen, P. Sainio, L. Laurila, J. Pippuri-Mäkeläinen, and K. Tammi, “Overview of powertrain electrification and future scenarios for non-road mobile machinery,” *Energies*, vol. 11, no. 5, p. 1184, May 2018.
- [10] K. Holmberg, P. Andersson, and A. Erdemir, “Global energy consumption due to friction in passenger cars,” *Tribology International*, vol. 47, pp. 221–234, Mar. 2012.

- [11] W. W. F. Chong, J.-H. Ng, S. Rajoo, and C. T. Chong, "Passenger transportation sector gasoline consumption due to friction in Southeast Asian countries," *Energy Conversion and Management*, vol. 158, pp. 346–358, Feb. 2018.
- [12] M. Zeraouia, M. E. H. Benbouzid, and D. Diallo, "Electric motor drive selection issues for HEV propulsion systems: A comparative study," *IEEE Transactions on Vehicular Technology*, vol. 55, no. 6, pp. 1756–1764, Nov. 2006.
- [13] J. Nerg, M. Niemela, J. Pyrhonen, and J. Partanen, "FEM calculation of rotor losses in a medium speed direct torque controlled PM synchronous motor at different load conditions," *IEEE Transactions on Magnetics*, vol. 38, no. 5, pp. 3255–3257, Sep. 2002.
- [14] P. Immonen, P. Lindh, H. Niemela, J. Pyrhonen, S. Sinkko, and M. Kasurinen, "Energy Saving by Hybridization of a City Bus," in *2014 16th European Conference on Power Electronics and Applications (EPE'14-ECCE Europe)*, 2014, pp. 1–8.
- [15] J. Nerg, M. Rilla, V. Ruuskanen, J. Pyrhonen, and S. Ruotsalainen, "Direct-driven interior magnet permanent-magnet synchronous motors for a full electric sports car," *IEEE Transactions on Industrial Electronics*, Vol. 61, no. 8, pp. 4286–4294, Aug. 2014.
- [16] X. Chen, J. Wang, B. Sen, P. Lazari, and T. Sun, "A high-fidelity and computationally efficient model for interior permanent-magnet machines considering the magnetic saturation, spatial harmonics, and iron loss effect," *IEEE Transactions on Industrial Electronics*, vol. 62, no. 7, pp. 4044–4055, Jul. 2015.
- [17] K. Yamazaki and M. Kumagai, "Torque analysis of interior permanent-magnet synchronous motors by considering cross-magnetization: Variation in torque components with permanent-magnet configurations," *IEEE Transactions on Industrial Electronics*, vol. 61, no. 7, pp. 3192–3201, Jul. 2014.
- [18] L. Chong, R. Dutta, and M. F. Rahman, "Field Weakening Performance of a Concentrated Wound PM Machine With Rotor And Magnet Geometry Variation," *Power and Energy Society General Meeting*, July 2010.
- [19] G. Pellegrino, A. Vagati, P. Guglielmi, and B. Boazzo, "Performance comparison between surface-mounted and interior pm motor drives for electric vehicle application," *IEEE Transactions on Industrial Electronics*, Vol. 59, no. 2, pp. 803–811, Feb. 2012.
- [20] I. Boldea, L. N. Tutelea, L. Parsa, and D. Dorrell, "Automotive electric propulsion systems with reduced or no permanent magnets: An overview," *IEEE*

-
- Transactions on Industrial Electronics*, Vol. 61, no. 10, pp. 5696–5711, Feb. 2014.
- [21] D. Dorrell, L. Parsa, and I. Boldea, “Automotive electric motors, generators, and actuator drive systems with reduced or no permanent magnets and innovative design concepts”, *IEEE Transactions on Industrial Electronics*, Vol. 61, no. 10, pp. 5693–5695, 2014.
- [22] V. Ruuskanen, J. Nerg, J. Pyrhönen, S. Ruotsalainen, R. Kennel, “Drive cycle analysis of a permanent-magnet traction motor based on magnetostatic finite-element analysis,” *IEEE Transactions on Vehicular Technology*, vol. 64, no. 3, pp.1249–1254, Mar. 2015.
- [23] V. Ruuskanen, J. Nerg, A. Parviainen, M. Rilla, and J. Pyrhönen, “Design and drive-cycle based analysis of direct-driven permanent magnet synchronous machine for a small urban use electric vehicle,” in *2014 16th European Conference on Power Electronics and Applications*, 2014, pp. 1–10.
- [24] X. Hu, N. Murgovski, L. M. Johannesson, and B. Egardt, “Optimal dimensioning and power management of a fuel cell/battery hybrid bus via convex programming,” *IEEE/ASME Transaction on Mechatronics*, Vol. 20, no. 1, pp. 457–468, Feb. 2015.
- [25] M. Polikarpova et al., “Hybrid cooling method of axial-flux permanent-magnet machines for vehicle applications,” *IEEE Transactions on Industrial Electronics*, vol. 62, no. 12, pp. 7382–7390, Dec. 2015.
- [26] C. E. Kilbourne, C. H. Holley, “Liquid cooling of turbine-generator armature windings,” *Electrical Engineering*, Vol.75, no. 5, pp. 436–441, May 1956.
- [27] M. Gerami Tehrani, J. Kelkka, J. Sopanen, A. Mikkola, and K. Kerkkänen, “Electric vehicle energy consumption simulation by modeling the efficiency of driveline components,” *SAE International Journal of Commercial Vehicles*, vol. 9, no. 2016-01–9016, pp. 31–39, Apr. 2016.
- [28] M. Gerami Tehrani et al., “Application of Hub-Wheel Electric Motor Integrated With Two Step Planetary Transmission for Heavy Off-Road Vehicles,” in *ASME 2015 International Design Engineering Technical Conferences and Computers and Information in Engineering Conference*, 2015, pp. V003T01A044–V003T01A044.
- [29] S. M. Shaahid and I. El-Amin, “Techno-economic evaluation of off-grid hybrid photovoltaic–diesel–battery power systems for rural electrification in Saudi Arabia—a way forward for sustainable development,” *Renewable and Sustainable Energy Reviews*, vol. 13, no. 3, pp. 625–633, Apr. 2009.

- [30] B. Bala and S. A. Siddique, "Optimal design of a PV-diesel hybrid system for electrification of an isolated island—Sandwip in Bangladesh using genetic algorithm," *Energy for Sustainable Development*, vol. 13, no. 3, pp. 137–142, Sep. 2009.
- [31] R. Sharma, C. Manzie, M. Bessede, M. J. Brear, and R. H. Crawford, "Conventional, hybrid and electric vehicles for Australian driving conditions – Part 1: Technical and financial analysis," *Transportation Research Part C: Emerging Technologies*, vol. 25, pp. 238–249, Dec. 2012.
- [32] R. Sharma, C. Manzie, M. Bessede, R. H. Crawford, and M. J. Brear, "Conventional, hybrid and electric vehicles for Australian driving conditions. Part 2: Life cycle CO₂-e emissions," *Transportation Research Part C: Emerging Technologies*, vol. 28, pp. 63–73, Mar. 2013.
- [33] T. A. Minav, J. J. Pyrhonen, and L. I. E. Laurila, "Permanent magnet synchronous machine sizing: Effect on the energy efficiency of an electro-hydraulic forklift," *IEEE Transactions on Industrial Electronics*, vol. 59, no. 6, pp. 2466–2474, Jun. 2012.
- [34] Q. Ren, D. A. Crolla, and A. Morris, "Effect of transmission design on Electric Vehicle (EV) performance," in *IEEE Vehicle Power and Propulsion Conference*, 2009. VPPC '09, 2009, pp. 1260–1265.
- [35] T. Holdstock, A. Sorniotti, M. Everitt, M. Fracchia, S. Bologna, and S. Bertolotto, "Energy Consumption Analysis of a Novel Four-Speed Dual Motor Drivetrain for Electric Vehicles," in *2012 IEEE Vehicle Power and Propulsion Conference (VPPC)*, 2012, pp. 295–300.
- [36] T. Hofman and C. H. Dai, "Energy Efficiency Analysis and Comparison of Transmission Technologies for an Electric Vehicle," in *2010 IEEE Vehicle Power and Propulsion Conference (VPPC)*, 2010, pp. 1–6.
- [37] A. Haddoun, M. E. H. Benbouzid, D. Diallo, R. Abdessemed, J. Ghouili, and K. Srairi, "A loss-minimization DTC scheme for EV induction motors," *IEEE Transactions on Vehicular Technology*, vol. 56, no. 1, pp. 81–88, Jan. 2007.
- [38] M. Gerami Tehrani, J. Kelkka, J. Sopenan, A. Mikkola, and K. Kerkkanen, "Transmission Configuration Effect on Total Efficiency of Electric Vehicle Powertrain," in *2014 16th European Conference on Power Electronics and Applications (EPE'14-ECCE Europe)*, 2014, pp. 1–9.
- [39] T. Aho, J. Nerg, J. Sopenan, J. Hupponen, and J. Pyrhönen, "Analyzing the effect of the rotor slit depth on the electric and mechanical performance of a solid-rotor

- induction motor,” *International Review of Electrical Engineering (IREE)*, vol. 1, no. 4, pp. 516–525, Sep./Oct. 2006.
- [40] R. D. Cook et al., *Concepts And Applications of Finite Element Analysis*, vol. 4. Wiley New York, 1974.
- [41] D. Wallace, O. De Weck and P. Young, “MITOpenCourseWare: Lecture Notes 15 | Engineering Design and Rapid Prototyping | Aeronautics and astronautics.” [Online]. Available: <https://ocw.mit.edu/courses/aeronautics-and-astronautics/16-810-engineering-design-and-rapid-prototyping-january-iap-2005/lecture-notes/15.pdf>. [Accessed: 22 Dec. 2016].
- [42] J. S. Rao, *Rotor Dynamics*, New Age International, 1996.
- [43] P. Immonen, P. Lindh, H. Niemelä, J. Pyrhönen, S. Sinkko, and M. Kasurinen, “Energy Saving by Hybridization of a City Bus,” in *2014 16th European Conference on Power Electronics and Applications*, 2014, pp. 1–8.
- [44] J. Nerg, M. Rilla, V. Ruuskanen, J. Pyrhönen, and S. Ruotsalainen, “Direct-driven interior magnet permanent-magnet synchronous motors for a full electric sports car,” *IEEE Transactions on Industrial Electronics*, vol. 61, no. 8, pp. 4286–4294, Aug. 2014.
- [45] P. M. Lindh, P. Immonen, Y. Alexandrova, M. G. Tehrani, J. J. Pyrhönen, and J. T. Sapanen, “The Design of Rotor Geometry in a Permanent Magnet Traction Motor for a Hybrid Bus,” in *2014 International Conference on Electrical Machines (ICEM)*, 2014, pp. 310–315.
- [46] A. Kulkarni, S. A. Ranjha, and A. Kapoor, “Fatigue analysis of a suspension for an in-wheel electric vehicle,” *Engineering Failure Analysis*, vol. 68, pp. 150–158, Oct. 2016.
- [47] A. Hobbacher et al., *Recommendations for Fatigue Design of Welded Joints And Components*, Springer, 2009.
- [48] F. C. Campbell, “Elements of metallurgy and engineering alloys,” *ASM International*, 2008, pp. 243–251.
- [49] A. Fatemi and L. Yang, “Cumulative fatigue damage and life prediction theories: a survey of the state of the art for homogeneous materials,” *International Journal Of Fatigue*, vol. 20, no. 1, pp. 9–34, Jan. 1998.
- [50] G. W. Winch and D. J. W. Arthur, “User-parameterised generic models: a solution to the conundrum of modelling access for SMEs,” *System Dynamics Review*, vol. 18, no. 3, pp. 339–357, Sep. 2002.

- [51] B. K. Powell, K. E. Bailey, and S. R. Cikanek, "Dynamic modeling and control of hybrid electric vehicle powertrain systems," *IEEE Control Systems*, vol. 18, no. 5, pp. 17–33, Oct. 1998.
- [52] H. Xu, A. Kahraman, N. E. Anderson, and D. G. Maddock, "Prediction of mechanical efficiency of parallel-axis gear pairs," *Journal of Mechanical Design*, vol. 129, no. 1, pp. 58–68, Jun. 2006.
- [53] N. E. Anderson and S. H. Loewenthal, "Design of spur gears for improved efficiency," *Journal of Mechanical Design*, vol. 104, no. 4, pp. 767–774, Oct. 1982.
- [54] S. Seetharaman and A. Kahraman, "Load-independent spin power losses of a spur gear pair: Model formulation," *Journal of Tribology*, vol. 131, no. 2, pp. 22201–22201, Feb. 2009.
- [55] "Adams" [Online]. Available: <http://www.mscsoftware.com/product/adams>. [Accessed: 16 Jan. 2015].
- [56] J. Montonen, S. Sinkko, P. Lindh, and J. Pyrhönen, "Design of a Traction Motor With Two-Step Gearbox for High-Torque Applications," in *2014 International Conference on Electrical Machines (ICEM)*, 2014, pp. 1069–1075.
- [57] J. Bélanger, P. Venne, and J.-N. Paquin, "The What Where and Why of Real-Time Simulation," *IEEE PES General Meeting*, 2010, pp. 25–29.
- [58] A. A. Shabana, *Dynamics of Multibody Systems*, Cambridge: Cambridge University Press, 2005.
- [59] P. Immonen, J. Pyrhönen, and P. Lindh, *Report of Lappeenranta City Bus Cycle: Lappeenranta Route 1*, Lappeenranta University of Technology, Nov. 2013.
- [60] J. Montonen et al., "Electric Drive Dimensioning for a Hybrid Working Machine by Using Virtual Prototyping," in *2012 XXth International Conference on Electrical Machines (ICEM)*, 2012, pp. 921–927.
- [61] J. Vance, F. Zeidan, and B. Murphy, "Computer simulations of rotordynamics," in *Machinery Vibration and Rotordynamics*, John Wiley & Sons, Inc., 2010, pp. 119–170.
- [62] M. Leader and R. Kelm, "Practical implementation of torsional analysis and field measurement," in *National Technical Training Symposium of the Vibration Institute*, 2004.

-
- [63] Math Works, *MATLAB, Computer Program*, Natick, MA, USA, The Math Works Inc., 2013.
- [64] M. Geveci, A. W. Osburn, and M. A. Franchek, “An investigation of crankshaft oscillations for cylinder health diagnostics,” *Mechanical Systems and Signal Processing*, vol. 19, no. 5, pp. 1107–1134, Sep. 2005.
- [65] M. A. Corbo and S. Malanoski, “Practical Design Against Torsional Vibration,” in *Proceedings of the Twenty-Fifth Turbomachinery Symposium*, 1996, pp. 189–222.
- [66] S. Suresh, *Fatigue of Materials*, Cambridge University Press, 1998, p. 223.
- [67] T. J. Barlow, S. Latham, I. S. Mccrae, and P. G. Boulter, “A reference book of driving cycles for use in the measurement of road vehicle emissions,” *Transport Research Laboratory Public Project Report.*, 2009.
- [68] Y. Gao, R. Long, Y. Pang, and M. Lindenmo, *Fatigue Properties of an Electrical Steel and Design of EV/HEV IPM Motor Rotors for Durability and Efficiency*, SAE Technical Paper 2010-01–1308, doi: 10.4271/2010-01-1308, Apr. 2010.

Publication I

Gerami Tehrani, M., and Sapanen, J.

Torsional Vibration Analysis of Multiple Driving Mode Hybrid Bus Drivetrain

Reprinted with permission from

ASME Proceedings IDETC,

*International Design Engineering Technical Conferences and Computers and Information in
Engineering Conference.*

Buffalo, USA, 17.-20.8.2014,

© 2014 American Society of Mechanical Engineers.

DETC2014-34539

Torsional Vibration Analysis of Multiple Driving Mode Hybrid Bus Drivetrain

Mohammad Gerami Tehrani
Department of Mechanical Engineering
Lappeenranta University of Technology
Skinnarilankatu 34
53850 Lappeenranta, Finland
Email: mohammad.gerami.tehrani@lut.fi

Jussi Sopanen
Department of Mechanical Engineering
Lappeenranta University of Technology
Skinnarilankatu 34
53850 Lappeenranta, Finland
Email: jussi.sopanen@lut.fi

ABSTRACT

Several hybrid electric driveline topologies have been introduced for vehicles in order to reduce emissions and improve energy efficiency in the transportation sector. This study introduces a novel configuration for a hybrid electric bus driveline. The designed driveline is capable of operating in pure electric, series and parallel hybrid modes. The torsional vibration analysis of the proposed drivetrain is performed for different driving mode configurations. The finite element method is applied to solve the torsional natural frequencies and mode shapes of the driveline. The model contains mass-elastic data of drive shafts, a diesel engine, a permanent magnet generator and a traction motor, as well as clutches and couplings. Different modelling strategies are discussed, and a sensitivity analysis is performed in order to determine the effect of different modelling parameters on the system's torsional frequencies and mode shapes. Different excitation frequencies arising from the diesel engine and electric drives are identified and compared to the natural frequencies.

Keywords: Hybrid Bus, Multi-Driving Mode, Torsional vibration analysis.

1 INTRODUCTION

With the advance of electric mobility technology, various combinations of electric machines and the internal combustion engine (ICE) are designed according to the hybrid electric vehicle (HEV) category. The main motivation for this development is to improve the efficiency of vehicles and to reduce harmful exhaust emissions [1]. In particular, these benefits are exceedingly important in city transportation, which has led to development of hybrid electric busses.

Energy efficiency has also been the main motivation in Lappeenranta University of Technology's Green Campus project [2], which promotes the usage and production of renewable energy. As part of the Green Campus project, electric transportation is demonstrated by designing a novel hybrid bus (CAMBUS). The bus will include a new hybrid electric system that is more energy efficient than the current versions available on the market since it only utilizes a 2.5-litre engine and has a larger battery capacity. The designed driveline for the hybrid bus is capable of operating in pure electric, series and parallel hybrid mode. The purpose of the CAMBUS' powertrain design is to reduce local emissions in the campus area, so the most desired driving mode is the pure electric traction. However, in order to ensure longer operation range, the diesel engine is kept in the drivetrain. In addition, the diesel engine can be used to assist the electric traction in case more power is needed.

In this study, the torsional vibration analysis of the designed hybrid bus driveline is presented. In rotating machinery, the power is transmitted by delivering the torque through the rotating drivetrain components. Common driveline components are shafts, couplings, gears, motors and generators for example or other work machines, such as blowers. Typically, the drivetrain components are selected and acquired from different manufacturers [3]. Corbo and Malanoski [4] have presented practical design steps for rotating machinery and they emphasized the importance of comprehensive torsional analysis at the design stage. Torsional vibration is an oscillatory angular motion causing shaft twisting that is superimposed on the steady rotational motion of rotating components [3]. Stress fluctuations can lead to metal fatigue and crucial failures if the system is not designed properly. This is especially true in the case where different torque excitation sources affect the drivetrain.

Feese and Hill [5] presented case histories of various problems in reciprocating machinery that had been caused by torsional vibration. In prevention of problems, a dynamic model of the whole driveline needs to be analyzed for different driving modes. Sapanen et al. [6] have studied the dynamic torque of a direct driven wind turbine drive train and surveyed the role of excitation due to electric machines on the system.

An adequately rigid crankshaft, a solitary operating engine and a constantly applied load are the common assumptions in the automotive industry that are also adopted in Williams' study [7]. Gawande and Navale [8] have studied power imbalance in a multi-cylinder inline diesel engine generator set and modeled the engine dynamics by discretizing the engine components into individual torque resources. Therefore, the crankshafts can be modeled as solid shafts that have the equivalent torsional stiffness of throws in series. The significance of torsional vibration and two measurement approaches is described in Adamsons' study [9]. Schulz [10] has studied the power split HEV drive train at low frequency, mainly concentrating on the controllability of the system.

According to literature survey, publications related to torsional vibration analysis of hybrid electric drivetrains are short-shrived as most of the publications consider torsional vibrations of turbomachinery or reciprocating machines. However, torsional vibration may affect the duty life and maintenance of the HEV considerably. This paper introduces a novel configuration of a hybrid bus driveline that is capable of operating in multiple driving modes (i.e. series, parallel and diesel engine only). Torsional natural frequencies and mode shapes are determined utilizing a finite element model of the drivetrain. An analysis of natural torsional frequencies and mode shapes of the powertrain is conducted. In addition, a parametric sensitivity analysis is also shown in order to determine the optimization possibilities.

2 TORSION VIBRATION ANALYSIS OF DRIVELINES

The most common modeling method for torsional systems is the mass-elastic model, where the system components are described by their mass moment of inertia and torsional stiffness. The first step in the torsional vibration analysis is to obtain the natural frequencies and torsional mode shapes of the system. Possible resonance speeds can be found by combining the information about the system's natural frequencies with excitation frequencies. In most cases, this is accomplished using a Frequency Interference Diagram. In order to decide if the torsional vibration amplitude at the found resonance speed is harmful, a forced vibration analysis should be performed.

For configuring the equation of motion of the system, the vibration model can be defined as follows:

$$\mathbf{M}\ddot{\mathbf{q}} + \mathbf{C}\dot{\mathbf{q}} + \mathbf{K}\mathbf{q} = \mathbf{T}(\mathbf{q}, t), \quad (1)$$

where \mathbf{M} is the mass matrix, \mathbf{C} is damping matrix, and \mathbf{K} is stiffness matrix. The vector \mathbf{q} contains the torsional degrees of freedom while \mathbf{T} is the vector of external torques. The mass and

stiffness matrices can be obtained from the mass-elastic data of the system using the standard finite element formulation.

The consistent mass matrix of the torsion bar element can be obtained employing the element shape functions as follows

$$\mathbf{m}_e^j = I_p \int_0^L \rho \mathbf{N}^T \mathbf{N} dx \quad (2)$$

where \mathbf{N} is the shape function matrix, I_p is the polar moment of inertia of the cross-section, ρ is the density of the material and L is the length of the torsion bar element. Using linear interpolation functions, the shape function matrix can be written as follows

$$\mathbf{N} = \left[1 - \frac{x}{L} \quad \frac{x}{L} \right] \quad (3)$$

Employing Equations (2) and (3), the consistent mass matrix of torsion bar element can be written as

$$\mathbf{m}_e^j = \frac{\rho I_p L}{6} \begin{bmatrix} 2 & 1 \\ 1 & 2 \end{bmatrix} \quad (4)$$

The global mass matrix of the system, \mathbf{M} , can be obtained from the element matrices using a standard finite element assembly procedure. The stiffness matrix \mathbf{K} can be assembled from the element matrices \mathbf{k}_e^j that can be defined as follows

$$\mathbf{k}_e^j = \frac{GI_{xx}}{L} \begin{bmatrix} 1 & -1 \\ -1 & 1 \end{bmatrix} \quad (5)$$

where G is the modulus of the rigidity of the material, I_{xx} and L are the torsion constant and the length of the element, respectively. It should be noted that in the case of a symmetric circular cross-section, parameters J_p and I_{xx} are equivalent. In general, the determination of the damping matrix \mathbf{C} is not as straightforward as in the case of the mass and stiffness matrices. One possibility to determine a full damping matrix is to use the estimated modal damping factors. In this procedure, the undamped eigenvalues and -modes of the system must be solved from

$$(\mathbf{K} - \omega_i^2 \mathbf{M}) \boldsymbol{\varphi}_i = \mathbf{0} \quad (6)$$

where ω_i is the angular frequency and $\boldsymbol{\varphi}_i$ is mode shape vector of mode i . The mode shape matrix $\boldsymbol{\Phi}$ can be constructed using the solved mode shape vectors as

$$\boldsymbol{\Phi} = [\boldsymbol{\varphi}_1 \quad \dots \quad \boldsymbol{\varphi}_n] \quad (7)$$

It must be noticed that the modes are normalized with respect to the mass matrix as follows

$$\boldsymbol{\Phi}^T \mathbf{M} \boldsymbol{\Phi} = \mathbf{I} \quad (8)$$

where \mathbf{I} is an identity matrix. The modal damping matrix \mathbf{C}_m is a diagonal matrix, the elements of which can be calculated as

$$c_i = 2\xi_i\omega_i \quad (9)$$

where ξ_i is the modal damping factor of mode i .

In general, the damping factors of steel or cast iron structures vary between 1% and 5%, depending on the material properties and the number of friction joints. On the other hand, an analytical model can be used to determine sufficient damping values that result in acceptable response levels. According to [11], a damping factor of 2% can be used in a conservative design. A full damping matrix can be obtained from the modal damping matrix using the inverse transformation as follows

$$\mathbf{C} = (\mathbf{\Phi}^T)^{-1} \mathbf{C}_m \mathbf{\Phi}^{-1} \quad (10)$$

At this point, it is important to point out that in the case of slightly damped torsional systems, the undamped and damped natural frequencies differ only moderately. Therefore, by putting $\mathbf{T} = \mathbf{0}$ in Equation (1), the natural frequencies of the system can be derived with a fair degree of accuracy.

2.1 Crankshaft modelling

For modeling the reciprocating machinery and specifically internal combustion engines, the most complicated task is to model the crankshaft. The equations used for calculating the torsional stiffness of the crankshaft are based on the dimensions of the journals, webs and crank pin and the shaft material's shear modulus. [5]

The basic equations for the shaft element's polar area moment of inertia (I_p) and torsional stiffness (K_t) are

$$\left. \begin{aligned} I_p &= \frac{\pi D^4}{32} \\ K_t &= \frac{GI_p}{L_e} \end{aligned} \right\} \Rightarrow K_t = \frac{\pi G}{32} \left[\frac{L_e}{D} \right] \quad (11)$$

where D is shaft diameter, G is shear modulus and L_e is the equivalent shaft length. Various modifications of Equation (11) for the crankshaft with complicated geometry are proposed, in this study, the Ker Wilson and the Carter formulae [12] are applied for deriving the torsional stiffness of the crankshaft

$$K_{t,KerWilson} = \frac{\pi G}{32} \left[\frac{L_j + 0.4D_j}{D_j^4 - d_j^4} + \frac{L_c + 0.4D_c}{D_c^4 - d_c^4} + \frac{R - 0.2(D_j + D_c)}{L_w W_c^3} \right] \quad (12)$$

where D_j and d_j are journal outer and inner diameters respectively, while D_c and d_c are crankpin outer and inner diameters, respectively. Note that if the crankshaft is made of a solid journal and crank pin, d_j and d_c are zero. Correspondingly, L_j , L_c and L_w are journal, crank pin and web lengths. R is the throw radius as shown in Figure 1. The equivalent web width W_c can be obtained using the following equation [13]

$$\frac{1}{W_c^3} = \frac{1}{2} \left(\frac{1}{W_{min}^3} + \frac{1}{W_{max}^3} \right) \quad (13)$$

The Ker Wilson formula gives more accurate results when the web stiffness is relatively higher than that of the journals and crank pin. This occurs especially in this case since the web of the crankshaft is 8-shaped and wide. Another equation for the crankshaft's torsional stiffness is proposed by Carter. Carter's formula is more applicable when the webs are deforming the most, as can be seen in the following equation

$$K_{t,Carter} = \frac{\pi G}{32} \left[\frac{L_j + 0.8L_w}{D_j^4 - d_j^4} + \frac{0.75L_c + 1.5R}{D_c^4 - d_c^4} + \frac{1.5R}{L_w W_c^3} \right] \quad (14)$$

The polar mass moment of inertia at each throw is a function of rotary inertia and the effect of reciprocating mass. The effect of reciprocating mass on the total moment of inertia varies in each revolution of the crankshaft. In this case, it can be neglected due to the relative high speed working point in which the crankshaft's angular acceleration variation is smooth. In addition, the operation definition does not allow excessive load to be imposed onto the ICE at low rotational speeds [14].

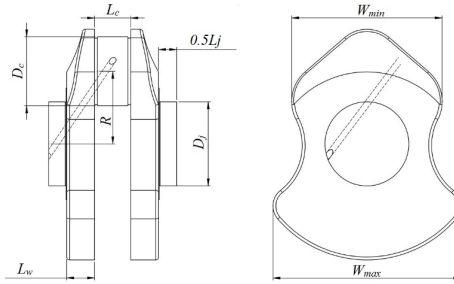


Figure 1 Crankshaft geometry

An equivalent moment of inertia (J_{eq}), including reciprocating mass (piston head, piston rod), can be estimated by adding half of reciprocating mass (M_{recp}) times the throw radius squared to the rotating inertia (J_{rot}) of crankshaft part as follows

$$J_{eq} \approx J_{rot} + 0.5R^2 M_{recp} \quad (15)$$

According to the geometry of the piston rod, the mass distribution on the piston rod is denser around the crankpin. Thus, the amount of mass that is located on two-thirds of the piston rod length, nearby the throw, is assumed as a rotary part and the rest is reciprocating with a piston complex [5].

3 MULTI DRIVING MODE HYBRID BUS DRIVELINE

In this section, the studied hybrid bus' driveline is introduced and its modelling parameters for torsional analysis are described. The layout of driveline's active components is

shown in Figure 2. The first component is a 2.5-litre, five cylinder diesel engine that operates the generator. The diesel engine and generator can be connected or disconnected from the electric traction motor by employing the magnetically actuated clutch. In fact, the clutch makes it possible to have multiple driving modes in the driveline. Driving modes are generally categorized into two main modes: series and parallel but in this case, a hybrid parallel drive is also possible.

In series drive mode, the clutch between the generator and traction motor is deactivated and the drivetrain is split into two separate systems: engine-generator and traction motor, drive shafts and tires. The engine-generator part starts to run when the battery charge level is low or extra power is required. The traction motor is transmitting driving power through drivetrain components such as the cardan shaft, rear differentials and rear axles to the tires. This is the most common driving mode, and supply power and electrical excitations harmonics are the most dominant excitations in the vibratory system.

The parallel drive mode is employed in a condition where the entire possible power is required by the operator; in that case, the diesel engine and electric motor are collaborating synchronously. In addition, there is also a driving mode where only the diesel engine is supplying power to the tires. This can be feasible and the most energy efficient driving mode in cases when the bus is driving at a constant speed on the highway at speeds from 60 km/h to 80 km/h. In that case, it is neither feasible nor efficient to convert mechanical energy to electrical energy and consume it in the traction motor. In this case the produced torque from the diesel engine is transmitted to the tires by means of electric machine shafts while there is no electric torque interference. In direct drive, all the driveline components, from beginning to end, are carrying the load and a long multi-material shaft including a coupling is the transmitting axle. This driving mode could be also used in the situation where all the batteries are depleted.

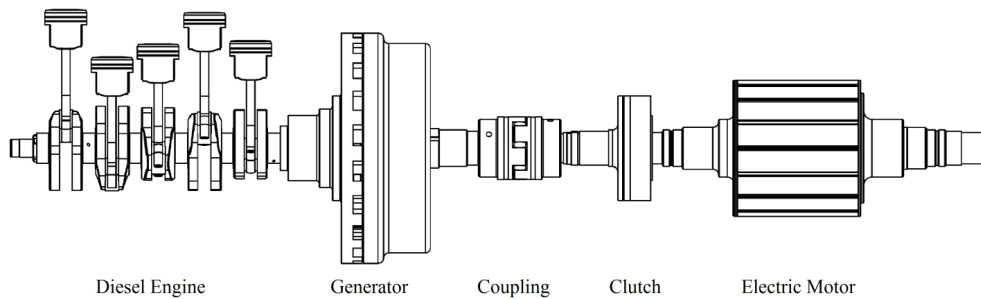


Figure 2 Driveline layout (cardan shaft, differential, wheels are omitted).

The numerical analysis of the driveline's torsional vibration is done by computer software [15] using the finite element method. Applying the in-house rotor dynamics toolbox (RoBeDyn) enables the visualization of the mode shape graphs through the transparent 3D model of system. It helps to diagnose the modal variation to its correspondent nodes in the drivetrain to modify the points that cause resonance in the system.

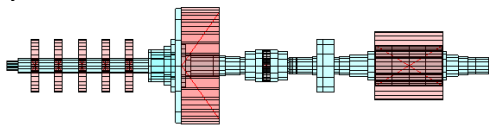


Figure 3 Visualization of finite element discretization

According to [16], the drive train can be adequately modeled with just a few elements as bar and mass elements. Defining the input variables in RoBeDyn is done by discretizing the driveline into stiffness and mass elements. In the driveline, the components having parts that do not bear any

torsional forces are modeled in two steps. The part of component that carries the torsional load is modeled as a shaft and the portion that only imposes inertia around the axis is modeled as a mass element. By having the material-inherent properties, the mass moment of inertia and torsional stiffness of elements are calculated by the element's inner and outer diameter. [17]

3.1 Crankshaft

For modeling the crankshaft, a massless beam that has the journal diameter and equivalent torsional stiffness of a throw (K_t) is defined. The mass moment of throw inertia is calculated numerically and the equivalent moment of inertia (J_{eq}) is defined on the corresponding nodes on the beam element. Despite the fact that some earlier studies [8] considered the crankshaft as one rigid body, in this study, each throw is modeled as an individual mass that has a separate torsional degree of freedom. As a result, the crankshaft and generator rotor assembly contains six degrees-of-freedom that refer to crankshaft throws and the rotor of the generator.

The equivalent stiffness coefficients for the crankshaft of the diesel engine are calculated employing Eqs. (12)-(14). The parameters of the studied crankshaft are shown in Table 1.

In order to verify the crankshaft stiffnesses obtained by using Eqs. (12)-(14), a detailed finite element calculation of one throw is conducted. In Figure 4, the used finite element mesh and the boundary conditions that are applied to the model are shown. In the analysis, torque M is applied at the end of one journal while the other end is fixed. The resulting twist angle φ of the throw can be evaluated from the resulting displacements. Torsional stiffness can be obtained as follows

$$K_t = \frac{M}{\varphi} \quad (16)$$

Table 1 Crankshaft parameters

Parameter	Value
D_j	58 mm
D_c	47.50 mm
L_c	25 mm
L_j	25 mm
L_w	19.25 mm
W_{max}	130 mm
W_{min}	104 mm
R	50 mm
Modulus of Elasticity	210 GPa
Poisson ratio	0.3
Density	7600 kg/m ³

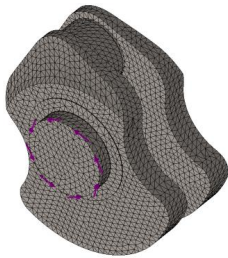


Figure 4 3D FEM model of one throw.

A comparison of the calculated equivalent stiffnesses is shown in Table 2. Regarding the studied crankshaft geometry in which the crank pin is more flexible than the web, it could be expected that the Ker Wilson formula is more accurate. Carter's formula seems to overestimate the stiffness because it is more suitable for models with a rigid crankpin and flexible web.

Table 2 Comparison of calculated torsional stiffnesses (K_t) of one throw (kNm·rad⁻¹)

Ker Wilson' Formula	Carter's Formula FEM	
565	798	533

Other attachments to the crankshaft that have considerable mass and inertia are the piston and the piston rod, as shown in Figure 5. The lower two thirds of the rod are considered as a rotary mass and should be added to the mass moment of inertia of the crank pin. The rest of the rod mass and piston mass are known as the reciprocating mass M_{rec} (see Eq. (15)), thus the equivalent moment of inertia that influences each throw is $J_{eq} = 0.0165 \text{ kgm}^2$.

It should be noted that the CAD model and mechanical properties of the piston and the piston rod are estimated based on the crankshaft's geometry. Correct values should be obtained for more accurate results.

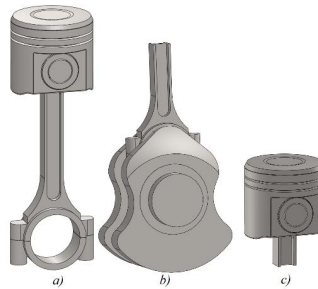


Figure 5 a) Piston and connection rod b) Rotating complex $J_{xx,rot} = 0.0145 \text{ kgm}^2$ c) Reciprocating part $M_{rec} = 1.629 \text{ kg}$

3.2 Outer rotor ferrite surface permanent magnet synchronous generator

The direct-driven generator is connected to the back of the diesel engine by means of an extension hub. The diesel engine flywheel is replaced by the generator rotor that has a larger mass and according to its bigger diameter; consequently, the moment of inertia which is carried by the crankshaft is increased. In this case, the capability of the crankshaft to run the generator rotor needs to be predicted. The difference between the flywheel's and the generator rotor's dimensions is apparent in Figure 6.

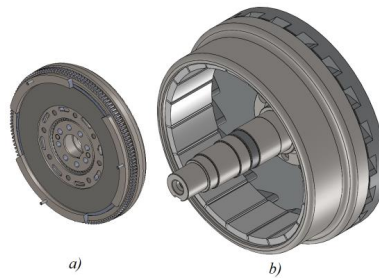


Figure 6 Size comparison of: a) original flywheel b) rotary components of the outer rotor generator

The rotating parts of the generator are a solid shaft, a back plate, the outer rotor hub and 20 permanent magnets. The total moment of inertia of the generator will be computed by the sum of constitutive components in Table 3.

Table 3 Generator components mass moment of inertia around main shaft

Component	Mass moment of inertia, J (kgm ²)
solid shaft	0.0136
back plate	0.5294
outer rotor hub	0.9161
magnets	0.2961
Total	1.7552

In order to model the generator, the solid shaft and the back plate that carry the torsion are modeled as beam elements, and those components that only rotate with a negligible share in total stiffness are modeled as a mass element (red ring in Figure 3). For the mass element, the moment of inertia is 1.2256 kgm² that is obtained by combining the inertias of the outer rotor hub and magnets. In comparison, this is significantly larger than the original flywheel with a moment of inertia of 0.1428 kgm².

3.3 Coupling

A coupling is added to the driveline mainly because the assembly of the driveline would be laborious without it. However, it has significant role in the dynamics of the driveline, since it adds flexibility and damping to the system. Most of the flexibility of the drivetrain is due to the spider rubber between the coupling forks. The material of the spider is selected from [18] considering maximum speed and torque transmissibility. The torsion spring stiffness of the spider according to the catalog is 114.73 kNm·rad⁻¹, and its damping ratio can be estimated to 6% based on the resonance factor data given by the manufacturer. This is also in line with published guidelines in the literature [3]. However, the actual damping should be determined with experimental measurements.

It should be noticed that the stiffness of the coupling forks is considerably higher than that of the spider. Since these are connected in series, the equivalent stiffness is quite close to the spider's stiffness. The spider's mass moment of inertia around the bore axis by applying polyurethane (PUR) as material is $J_{xx} = 0.0002$ kgm².

Two thirds of coupling hubs are assumed to be completely engaged with the generator shaft on one side and with the traction motor solid shaft on the other side. The linear relation between torsional stiffness and beam element length makes it simple to modify the complete coupling hub stiffness by multiplying by two. The rest of the coupling hub's mass moment of inertia is added to the spider inertia in order to have a concentrated mass at the middle. As shown in Figure 7 (a), the middle element is modeled according to the spider's characteristics and the portion (1/3) of coupling hubs that only have an inertial effect are modeled as rings at two ends.

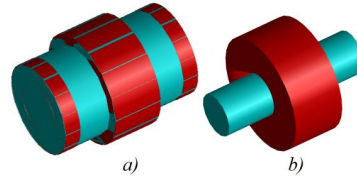


Figure 7 RoBeDyn model of coupling; a) considering hub coupling principles b) defining a spring element and one mass elements

In the second modeling approach, coupling modeling is done by defining a spring element at the coupling's mid-point; its stiffness is taken from a catalog. The inertial effect of the other parts of the coupling is halved and separately enclosed at the overlapped nodes at the coupling's mid-point (see Figure 7 (b)). The driveline is more torsionally flexible by applying this method because the relatively long and thin shaft between the generator and traction motor increases flexibility. These two methods are implemented in the model and compared in the sensitivity analysis.

In the spider selection chart, different stiffnesses are selectable according to the nominal load and speed. Since it is assumed that the flexibility of the spider is determinant in torsional vibration, this parameter is studied in the sensitivity analysis.

3.4 Electromagnetic clutch

The medium between the electrical traction and mechanical propulsion is an electromagnetic clutch that is actuated when the electrical power is not enough to run the bus and there is a demand for more torque on wheels. In both the parallel hybrid and the engine direct drive mode, the electromagnetic clutch is engaged. A schematic of the clutch (gray part) is shown in Figure 8. In the figure, the shaft (blue part) is connected to the generator and the diesel engine via a coupling and the electromagnetic clutch is connected to the traction motor shaft. Most of the torsional flexibility of the clutch is due to a shaft with a relatively long length.

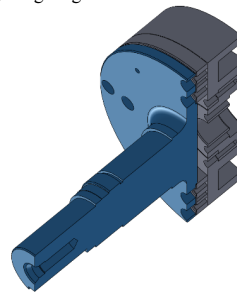


Figure 8 Cross-section view of electromagnetic clutch

The torsional stiffness of the shaft is 257 kNm·rad⁻¹ while the corresponding stiffness of the grey disk is 38911 kNm·rad⁻¹. The mass moment of inertia around the main axis for the blue disc is 0.0123 kgm², and for the grey disc 0.0286 kgm², respectively. In modeling the magnetic clutch, all the elements are defined as beam elements and for adding the possibility of analyzing the entire driveline in closed and open status, two individual nodes are defined at the discs' point of contact. A spring element with a relatively high stiffness is defined between the left and right elements in closed status, and in open status the spring element stiffness between two nodes is set to zero.

3.5 Permanent magnet synchronous motor

The main traction source of the bus is an electric motor (nominal speed 2241 rpm) that is designed to cover the defined driving cycle. The traction motor components' mass moment of inertias are listed in Table 4. The rotor consists of solid shaft, magnet housing and magnets.

Table 4 Inertia of traction motor components.

Component	Mass moment of inertia J (kgm ²)
solid shaft	0.2086
magnet housing	0.4786
magnets	0.1057
Total	0.7930

Solid shafts can be modeled easily, but there are three techniques for modeling the contribution of the magnet assembly to the total mass moment of inertia (Figure 9): a concentrated mass at the midpoint, multiple equal fractions of total mass that are evenly distributed on the solid shaft and an additional tubular beam element that provides not only mass but stiffness. These three different methods are implemented for the sensitivity analysis.

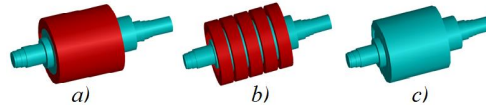


Figure 9 Different approaches for the inertia modeling of the traction motor

4 RESULTS

4.1 Torsional Natural Frequencies and Mode Shapes

The results of the torsional analysis are shown in this section. As the studied hybrid bus driveline is still at the design stage, the torsional vibration analysis has some uncertainties. In order to validate the design's robustness and to find the weak points of the system [19], a parametric sensitivity analysis is performed (i.e. several cases with different parameters are analyzed). Parameter variations are based on the error estimates of the model input data.

The driveline components omitted in Figure 2 are shown in Figure 10. The cardan shaft is modeled by taking into account the engine's cabin space and carrying torque. The steel gear tooth stiffness ($E=200$ GPa) is used to calculate an equivalent bar element to model the differential. The rear axles and tires are also modeled by using the given data from the existing bus. The differential reduction ratio (7:1) is used in the calculation of the equivalent stiffness and inertia of the drive axles and tires. The equivalent stiffness and inertia for the above-mentioned components are used for simplifying the entire driveline into one axis.

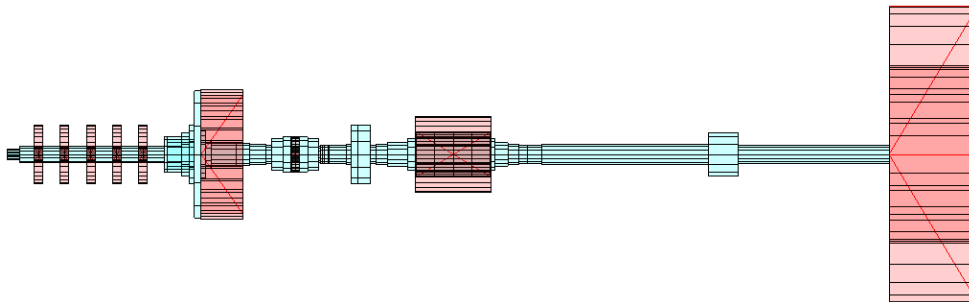


Figure 10 Complete driveline layout

The first two studied cases are the open and closed clutch conditions with the nominal driveline parameters. The three lowest torsional natural frequencies and mode shapes in these cases are shown in Figures 11 and 12. Open clutch conditions correspond to the serial driving mode, while the closed clutch configuration is active in the parallel or diesel only driving mode. The natural frequencies are higher in the series drive mode as was expected, since the drivetrain is split into two parts in this mode. By studying the mode shapes, it can be seen that tires which carry the bus load are behaving as fixed ends, and the largest deformation occurs either in the traction motor or in the diesel engine.

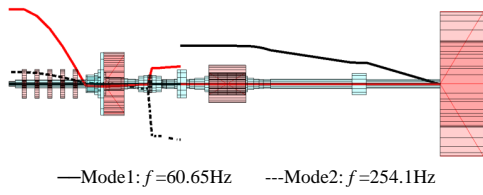


Figure 11 Driveline basic model in the open clutch status

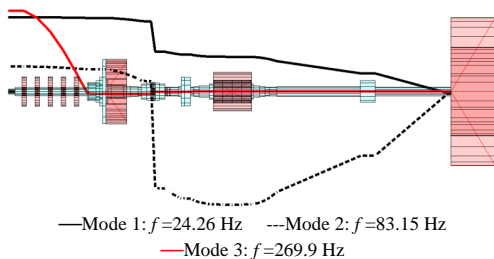


Figure 12 Driveline basic model in the closed clutch status

The sensitivity analysis is conducted by varying the model parameters that has uncertainties. The selected variations are: the diesel engine's inertia, the stiffness of the hub joint between the engine and generator; the coupling's stiffness and inertia; and the traction motor's inertia modeling

The results of the sensitivity analysis are shown in Table 5 for the open clutch configuration and in Table 6 for the closed clutch configuration.

Regarding the calculated frequencies in Table 5, the system is robust at low speeds, since the first natural frequency stayed almost constant even when the assumptions were modified. From cases 11 and 13, it can be concluded that the system is sensitive to the coupling stiffness at second mode. In cases three and five, it can be seen that variations in the crankshaft inertia parameters mostly affect the third natural frequency.

Table 5 Sensitivity analysis results in open clutch condition

Case#	1 st Mode (Hz)	2 nd Mode (Hz)	3 rd Mode (Hz)	Explanations
1	61	254	271	Basic Assumption
3	61	252	260	+10% $J_{eq,throw}$
5	61	255	284	-10% $J_{eq,throw}$
7	61	254	271	2×hub joint stiffness
9	61	254	271	-50% hub joint length
11	61	270	270	Coupling is modeled as a shaft (Figure 7a)
13	61	270	270	10×Spider stiffness
15	61	254	270	Motor mass divided into five (Figure 9b)
17	62	254	271	Equivalent motor rotor diameter (Figure 9c)

Table 6 Sensitivity analysis results in closed clutch condition

Case#	1 st Mode (Hz)	2 nd Mode (Hz)	3 rd Mode (Hz)	Explanations
2	24	83	270	Basic Assumption
4	24	83	258	+10% $J_{eq,throw}$
6	24	83	284	-10% $J_{eq,throw}$
8	24	83	270	2×hub joint stiffness
10	24	83	271	-50% hub joint length
12	29	126	270	Coupling is modeled as a shaft (Figure 7a)
14	29	128	270	10×Spider stiffness
16	24	83	270	Motor mass divided into five (Figure 9b)
18	24	85	270	Equivalent motor rotor diameter (Figure 9c)

4.2 Excitation frequencies

The torsional excitations of the studied driveline arise from two different sources. The reciprocating diesel engine causes engine harmonics, and electrical machines cause torque ripple and cogging torque harmonics. The excitation frequencies are discussed in this paper, however, a detailed forced response analysis is left for future studies.

In the well-known four-stroke engine operation principle, the expansion occurs in every half-revolution of the crankshaft. As a result, the working cycle of a four-stroke engine is two crankshaft revolutions, so the engine harmonics i are multiples

of 0.5 (e.g. $i = 0.5, 1, 1.5, 2, 2.5$). The excitation torque caused by the gas pressure can be presented as a Fourier-series. Each Fourier component of the torque is of the form

$$M_i = \frac{\pi D^2}{4} p_i r \quad (16)$$

where D is cylinder diameter, r is crank radius and p_i is the corresponding tangential pressure harmonic component.

Engine harmonics are shown graphically together with the system's overall three lowest natural frequencies in Figure 13. The purpose of this diagram is to visualize and detect the possible resonance operation speeds. At present, it only displays the frequencies of five harmonic components ($i = 0.5 \dots 2.5$), but more can easily be added [20],[4].

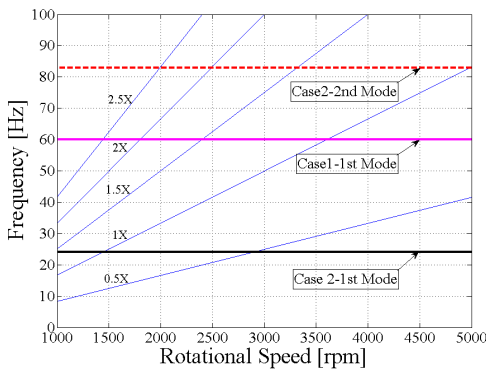


Figure 13 Frequency interference diagram showing the first five harmonic components of the engine rotational speed

The torque ripple frequency of permanent magnet synchronous machine is calculated as follows

$$f_{mec} = \frac{f_{el}}{P} \quad (17)$$

where f_{el} is electrical frequency and P is the number of pole pairs. Table 7 shows the major torque ripple harmonic components of the generator at the nominal point. When the electrical supply frequency is 500 Hz, the lowest generator torque ripple harmonic is the 6th harmonic. This means the torque ripple frequency affects the system at the rotational speed of 18000rpm, which is adequately far from the rated speed of the driveline. The generator reveals the cogging torque at the mechanical frequency of 6000 Hz that is also not a concern regarding the driveline operation range.

The lowest frequency in which the driveline is subjected to the traction motor's torque ripple is the 60th harmonic of the supply frequency. The cogging torque, due to counteraction between magnets and stator, manifests at 32th supply harmonic, which again is high enough to keep it out of the operation speed range.

Table 7 Harmonic spectrum of the torque ripple during one mechanical rotation

Harmonic number	Mechanical frequency [Hz]	Amplitude of torque harmonic [Nm]
6th	300	0.07
60th	3000	1.47
120th	6000	2.4
240th	12000	0.3

In summary, the electrical excitations in the studied driveline are significantly higher than the natural mechanical frequencies. Therefore, it is expected that the electrical excitations will not cause resonances in the system.

5 CONCLUSIONS

A novel multi-driving mode driveline for a hybrid bus that is capable of providing massive torque on wheels by means of the synchronous operation of three propulsion sources (diesel engine, generator and electric motor) in full parallel mode is introduced in this paper. Special focus is on the torsional vibration analysis of the driveline. The driveline components are modeled and analyzed employing the finite element method. Different strategies are applied to model the components as bar and mass elements. Torsional excitations due to diesel engine and electric machines are calculated in order to find out the probability of torsional resonances in the system. By analyzing the mode shapes from basic model simulation, the critical components are detected and different configurations of the driveline are analyzed regarding different strategies in modeling.

The uncertainties in the modeling at the design phase are due to a lack of an accurate input data. However, it was noticed that the behavior of the complete driveline model is not so sensitive to errors in some parameters. For example, it was noticed that $\pm 10\%$ difference in the equivalent inertia of the diesel engine's crankshaft throws did not have a significant effect on the results. Similar results were obtained for the coupling between the diesel engine and generator. This was noticed in both closed and open clutch conditions. In the sensitivity analysis, it was noticed that the most significant parameter affecting the natural frequencies is the stiffness of the flexible coupling.

Finally, the driveline's lowest natural frequency was determined to be 24 Hz in parallel mode and 61 Hz in serial mode. Diesel engine harmonics are in this range and they might lead to resonance vibrations. However, resonances due to torsional excitations of the electric machines are unlikely, since those frequencies are considerably higher than the system's natural frequencies.

Future studies include forced vibration analysis and experimental verification.

REFERENCES

- [1] P. Pisu, K. Koprubasi, and G. Rizzoni, "Energy Management and Drivability Control Problems for Hybrid Electric Vehicles," in 44th IEEE Conference on Decision and Control, 2005 and 2005 European Control Conference. CDC-ECC '05, 2005, pp. 1824–1830.
- [2] Lappeenranta University of Technology "Green Campus 2014." [Online]. Available: <http://www.lut.fi/web/en/green-campus>. [Accessed: 24-Apr-2014]
- [3] W. J. Chen and E. J. Gunter, Introduction to dynamics of rotor-bearing systems. Victoria, B.C.: Trafford Publishing, 2005.
- [4] M. A. Corbo and S. Malanoski, "Practical Design Against Torsional Vibration," Proceedings of the Twenty-Fifth Turbomachinery Symposium, 1996, pp. 189–222.
- [5] T. Feese and C. Hill, "Prevention of torsional vibration problems in reciprocating machinery," Proceedings of the thirty-eighth turbomachinery symposium, college station TX, Turbomachinery Laboratory, Texas A&M University, 2009, pp. 213–238.
- [6] J. Sopanen, V. Ruuskanen, J. Nerg, and J. Pyrhonen, "Dynamic Torque Analysis of a Wind Turbine Drive Train Including a Direct-Driven Permanent-Magnet Generator," IEEE Trans. Ind. Electron., vol. 58, no. 9, pp. 3859–3867, 2011.
- [7] J. Williams, "An Overview of Misfiring Cylinder Engine Diagnostic Techniques Based on Crankshaft Angular Velocity Measurements," SAE International, Warrendale, PA, SAE Technical Paper 960039, Feb. 1996.
- [8] S. H. Gawande, L. G. Navale, M. R. Nandgaonkar, and D. Butala, "Detecting power imbalance in multi-cylinder inline diesel engine generator set," in 2010 The 2nd International Conference on Computer and Automation Engineering (ICCAE), 2010, vol. 1, pp. 218–223.
- [9] S. Adamson, "Improved Approaches to the Measurement and Analysis of Torsional Vibration," SAE International, Warrendale, PA, SAE Technical Paper 2004-01-1723, Mar. 2004.
- [10] M. Schulz, "Low-frequency Torsional Vibrations of a Power Split Hybrid Electric Vehicle Drive Train," J. Vib. Control, vol. 11, no. 6, pp. 749–780, Jun. 2005.
- [11] "W. Reik, 'Torsional vibration in the drive train of motor vehicles principle consideration,' LuK Symposium, 1990." "Schaeffler Germany, Media Library, Publications." [Online]. Available: http://www.schaeffler.com/remotemedien/media/shared_media/08_media_library/01_publications/schaeffler_2/symposia_1/downloads_11/4_Torsional_Vibrations_Motor-Vehicles_1.pdf. [Accessed: 24-Apr-2014]
- [12] Z. Guangming and J. Zhengfeng, "Study on Torsional Stiffness of Engine Crankshaft," in International Forum on Computer Science-Technology and Applications, 2009. IFCSTA '09, 2009, vol. 3, pp. 431–435.
- [13] E. J. Nestorides, A handbook on torsional vibration, Cambridge: Cambridge University Press, 2011, pp. 55–75.
- [14] M. S. Pasricha and W. D. Carnegie, "Torsional Vibrations In Reciprocating Engines," J. Ship Res., vol. 20, no. 1, Mar. 1976.
- [15] Math Works, 2013, *MATLAB*, computer program, The Math Works Inc., Natick, MA, USA
- [16] J. Vance, F. Zeidan, and B. Murphy, "Computer Simulations of Rotordynamics," in Machinery Vibration and Rotordynamics, John Wiley & Sons, Inc., 2010, pp. 119–170.
- [17] M. E. Leader, R. D. Kelm, "Practical Implementation of Torsional Analysis and Field Measurement" Vibration Institute, 2004 Annual Meeting Proceedings.
- [18] KTR Company catalog, 2014, [Online]. Available: http://www.ktr.com/root/img/pool/pdf/produktkataloge/en/en_gesamt/001_rotex_en.pdf. [Accessed: 24-Apr-2014]
- [19] N. Bachschmid, P. Pennacchi, And A. Vania, "Identification Of Multiple Faults In Rotor Systems," J. Sound Vib., vol. 254, no. 2, pp. 327–366, Jul. 2002.
- [20] M. Geveci, A. W. Osburn, and M. A. Franchek, "An investigation of crankshaft oscillations for cylinder health diagnostics," Mech. Syst. Signal Process, vol. 19, no. 5, pp. 1107–1134, Sep. 2005.

Publication II

Sinkko, S., Juho M., Gerami Tehrani, M., Pyrhönen, J., Sopenan, J. and Nummelin, T.
Integrated hub-motor drive train for off-road vehicles

Reprinted with permission from
EPE'14 ECCE Europe,
European Conference on Power Electronics and Applications.
Lappeenranta, Finland, 26.-28.09.2014,
© 2014, IEEE.

INTEGRATED HUB-MOTOR DRIVE TRAIN FOR OFF-ROAD VEHICLES

Simo Sinkko¹, Juho Montonen³, Mohammad Gerami Tehrani², Juha Pyrhönen³, Jussi Sopenen^{2,3}, Tommi Nummelin¹

¹UNIT OF TECHNOLOGY, SAIMAA UNIVERSITY OF APPLIED SCIENCES, LAPPEENRANTA, FINLAND

Skinnarilankatu 36

Lappeenranta, Finland

Tel.: +358 / (20) – 4966 511

Fax: +358 / (20) – 4966 588

²DEPT. OF MECHANICAL ENGINEERING LAPPEENRANTA UNIVERSITY OF TECHNOLOGY (LUT), LAPPEENRANTA, FINLAND

³DEPT. OF ELECTRICAL ENGINEERING, LUT

Skinnarilankatu 34

Lappeenranta, Finland

Tel.: +358 / (294) – 462 111

Fax: +358 / (5) – 411 7201

E-Mail: simo.sinkko@saimia.fi, jussi.sopenen@lut.fi, mohammad.gerami.tehrani@lut.fi, juho.montonen@lut.fi, juha.pyrhonen@lut.fi, tommy.nummelin@saimia.fi

URL: <http://www.saimia.fi/>

URL: <http://www.lut.fi/>

Acknowledgements

Authors would like to thank the Centennial Foundation of the Technology Industries in Finland and Tekes – the Finnish Funding Agency for Technology and Innovation for their financial support.

Keywords

«Electrical drive», «Traction application», «Permanent magnet motor», «Automotive application», «Power transmission», «Simulation»

Abstract

A new concept that integrates a permanent magnet (PM) synchronous motor (PMSM) and a 2-step planetary gearbox for heavy machinery electric traction is introduced. A clear need for this kind of a solution is recognized in the field of diesel-electric hybrid off-road vehicles as electrical machine cannot fulfill alone all the demands of the typical load cycles of working machines. The technology introduced also suits in some road vehicle use e.g. for buses or trucks. The benefits of the solution are pointed out and its functionality is proven by simulations. The dynamic performance of the driveline is analyzed using a co-simulation approach that accounts the mechanical system and the dynamics of the control system.

1. Introduction

In this study, a new type of electric traction motor system that fulfills the special needs of off-road vehicles is introduced. Due to the limitations of the operational range of electric motors in general, they are often incapable alone to function as hub motors of an off-road machine. In light road vehicles, such as passenger cars a gearbox is normally not needed as the starting torque ratio to the top speed torque is typically in the range of 5 – 6 while in off-road applications this ratio can be in the range of

10 – 30. Integration of a two-speed gearbox and a PMSM in one compact package enables usage of hub motors in off-road vehicles and other heavy machinery and gives full benefits of an electric driveline for the system. So far integration of a step-down gear inside an electric machine has been suggested [1].

The high freedom to select the geometry of a PMSM enables such integration, especially, in case of tooth-coil PMSMs which are – without sacrificing any important properties – capable of producing a high torque-per-volume ratio and can be realized as a thin rim inside which a gearbox can be fitted. The basic operation principle, the mechanical structure and simulation results of this new component will be studied here.

Traditional hub motors have problems to function in such a wide operational range that is needed for example in a normal agricultural tractor. If the motor is dimensioned to give enough torque with suitably low speed for tough working processes, then it will not produce enough torque at high rotational speed in some other tasks such as on-road driving.

The best option for off-road vehicle traction motor seems to be the permanent magnet synchronous motor, especially a tooth-coil wound machine with concentrated fractional non-overlapping windings which enable the smallest possible end winding [2]. Such PMSMs can occasionally reach three times their nominal torque at low speeds and more than two times their nominal rotating speed with good efficiency while the drop in torque remains reasonable [3]. Typical properties include high torque and power densities, high torque capability at low speeds, wide operational speed range, high efficiency over the speed range, high reliability, and acceptable cost [4, 5]. Maximum torque curve and thermal limit curve of a permanent magnet synchronous motor drive is presented in Figure 1. Converter current capability is selected three times the nominal motor current as they usually do not tolerate large currents even for short time periods. It can be seen that a combination of an oversized converter and a tooth-coil wound PMSM design has a high torque reserve at low speeds to give high traction force at start. By machine design it is also possible to adjust the synchronous inductance of a tooth coils machine in such a way that suitable field weakening range will be reached. Integrating a gear and a tooth-coil PMSM also enables an efficient cooling solution which in this case is achieved by transmission oil splashing over the PMSM. An external oil filtering and cooling system will be needed. A water-cooling jacket solution may be possible but complicates the machine housing design.

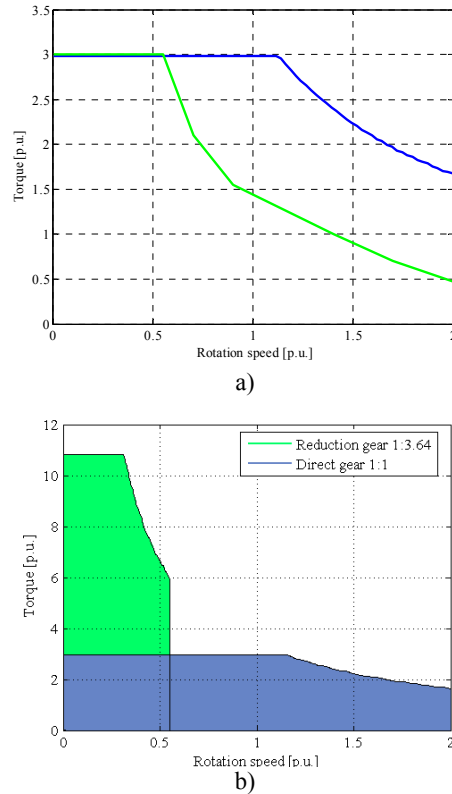


Fig. 1: a) Maximum torque curve (blue) and thermal limit curve (green) of a permanent magnet synchronous motor drive designed for good field weakening properties b) gear changing effects based on the maximum torque curve, gear ratio is now 3.64.

In mechanical or hydro-mechanical transmissions there are as many gear steps as it is needed to find suitable torque – speed combinations. In electric drivelines the target is usually to make the layout simpler and get rid of complicated mechanical transmissions if possible. In demanding off-road vehicles this is, however, not possible and a clever integration of a two-speed gearbox and an electric drive is needed.

Let us examine an agricultural tractor and its demands more closely. Typical values for a mid-size agricultural tractor are listed in Table I.

Table I: Typical values for mid-size agricultural tractor

Mass, m [kg]	6000
Motor nominal power, P [kW]	140
Motor nominal speed, n [1/min]	1900
Motor nominal torque, T_n [Nm]	600
Rear tire diameter, D_{tire} [m]	1.8
Total transmission efficiency, η	0.8

Let us compare two typical tasks often carried out with tractors [6]; hard ploughing at a speed of 5 km/h and on-road drive at 50 km/h.

In this kind of evaluation, the traction force is the most important factor. The traction force F is defined by the motor torque T , transmission efficiency η , total gear ratio i_{tot} and the tire radius r by:

$$F = \frac{T \eta}{r i_{\text{tot}}} \quad (1)$$

The torque in the single tire of a four-wheel vehicle is obtained when the motor torque is multiplied with the overall gear ratio and gear efficiency. With traditional transmissions there is probably a gear step with which something very close to the optimum torque – speed combination can be found. If the system is simplified the torque of one tire is

$$T_{\text{tire}} = \frac{T \eta}{i_{\text{tot}} \times 4} \quad (2)$$

The optimal total gear ratio i_{tot} can be calculated by dividing the tire's rotating speed with the engine's nominal rotating speed. The same gear ratio is then used for calculating the maximum torque for tire.

According to Equations (1) and (2), in the example case of the agricultural tractor with traditional mechanical transmission, there is 68.7 kN traction force available for the whole tractor when it is ploughing with speed of 5 km/h. It means that each tire has 17.2 kN traction force.

If we want to reach same ploughing performance with electric hub motors, we have to select the calculated 17.2 kN traction force as a target value when dimensioning the motor. In the example case, with 1.8 m tire diameter, it means that 15.5 kNm torque is needed from one tire. Separate, fixed ratio reduction gear is naturally needed so that electric motor speed range will be reasonable. When ploughing, the load is continuous and the motor has to operate at no-higher than its nominal torque as the maximum torque can only be allowed for short spurts. If the PMSM nominal rotating speed would be e.g. 1000 1/min then the nominal torque (with 35 kW) would be 334 Nm and needed reduction gear ratio would be $i_{\text{tot}} = 67.8$ (motor nominal speed) / (rear tire rotating speed in the speed of 5 km/h) = 67.8.

The electric motor is capable of rotating at 2.5 times the nominal speed. Despite this the tractor maximum linear speed will not exceed 12.5 km/h with a fixed step-down gear. In practice, it clearly should result in a too low top speed.

If the dimensioning would be done so that the maximum speed would be 50 km/h, the corresponding maximum traction force for one wheel would be only 4.3 kN (gear ratio $i_{\text{tot}} = 17.0$), which is too small for ploughing and other heavy-duty tasks.

The obvious conclusion is that at least a two-speed gear box is needed if both off-road and on-road tasks have to be covered by the same machine.

2. Structure studied

The new integrated construction consists of a multiple-pole tooth-coil permanent magnet synchronous electric motor integrated with a planetary gear system. Such a motor design allows locating the planetary gear inside of the electric motor rotor as the rotor yoke is thin and a suitably large space inside the rotor can be found. Different parts and the layout of the structure are introduced in Figure 2.

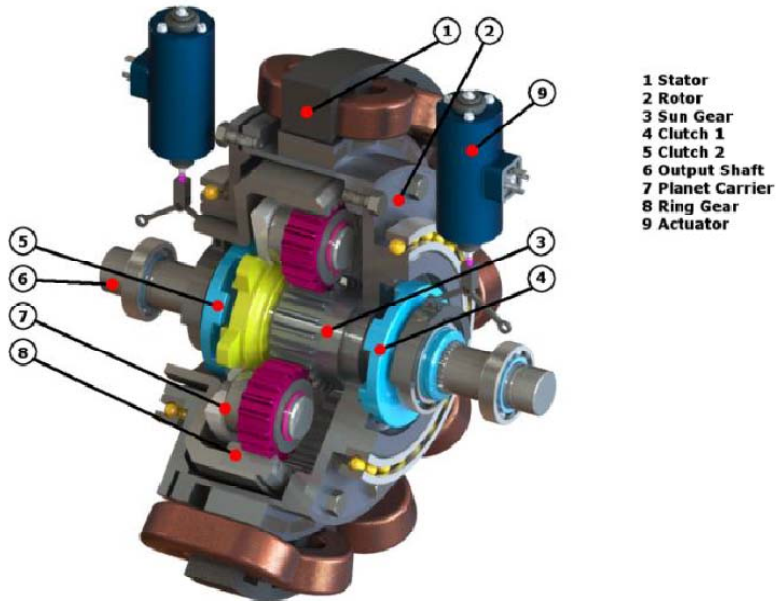


Fig. 2: Section view of the integrated tooth-coil PMSM and a planetary gear inside a PMSM. The thin rotor yoke of the multiple-pole machine enables placing the planetary gear inside the rotor

In this design the rotor of the electric motor is fixed to the sun gear of the planetary gear set. The direct gear ratio is obtained when clutch 1 is activated. Then the power is transferred from the sun gear to the output shaft through the activated clutch (Figure 3). In this case the planet carrier rotates freely and the ring gear is fixed.

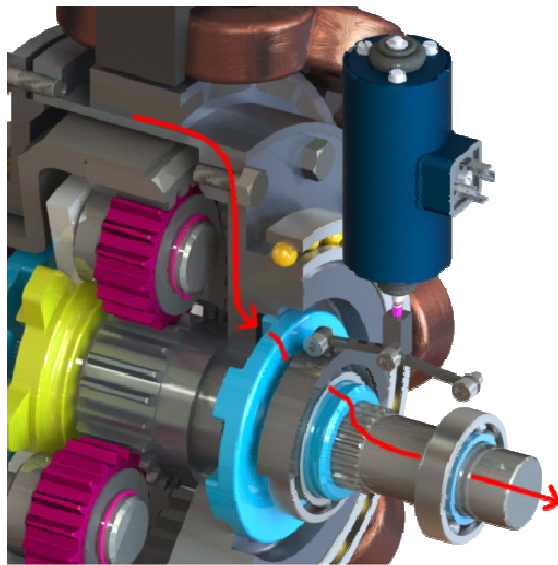


Fig. 3: Power route with direct gear activated

The reduction gear ratio depends on the teeth number of the ring gear, the sun gear and the planet gears. Typical values that can be achieved easily are 1:2 – 1:10 [7]. For the tractor application a gear

ratio of 1:4 would be appropriate. That would enable high torque and traction force capacities at low speeds (reduction gear activated) and high enough speed with the direct gear ratio (1:1).

The introduced construction is very compact, particularly, if compared to the combined size of a standard electric motor and a gearbox. The volume inside the electric motor that is inactive in standard electric motors will be now used for the planetary gear. Basically, the integrated solution fits almost in the same room as a standard electric motor.

One remarkable advantage is also that no additional hydraulic or pneumatic power is needed for shifting the gear, since a tooth clutch (i.e. dog clutch) is used in this construction. The torque is transmitted via teeth, which means that there is no need to push the clutch parts against each other with high forces like in the case of friction clutches. The profile for a tooth clutch is also designed so that it does not need great forces for engaging or disengaging. In practice, it means that the clutch can be operated by electric actuators, such as solenoids, voice coils or stepping motor drives, with low force and minimal stroke.

Nevertheless, the selected clutch type sets strict demands for the control of the gear shifting procedure in which both the electric motor speed and torque as well as clutch actuators must be simultaneously controlled. The shifting procedure contains the following steps:

1. Actuation signal is emitted.
2. Electric motor is set to no-load
3. Active clutch is disengaged.
4. Primary speed (electric motor) is adjusted to correspond to the new secondary speed (either smaller or greater)
5. Second clutch is engaged
6. Electric motor is enabled to create torque again.

Everything has to happen in a short time (e.g. in 100 ms) so that shifting will not cause problems for the machine driving. Here, a power electronic vector control converter plays an important role as it has the capabilities of fast synchronizing the speeds for the clutch engagements and is also capable of commanding the clutch operations. The converter control also enables smooth torque control avoiding e.g. undesired torque vibrations stressing the gear components unnecessarily.

3. Simulation model

The gear shifting procedure is studied using co-simulation approach where a detailed mechanical model and electric drive and control model are analyzed simultaneously. A mechanical model of the gear box with clutches is implemented in a multibody simulation software application (MSC.ADAMS [8]). The multibody simulation model includes the kinematical descriptions, masses and mass moments of inertias of gear-box components. Operation of the clutches is described using contact force elements. The simulation model of the electric motor, motor controller, power electronics and control logic of the whole system is implemented in Simulink. In co-simulation these two simulation models are combined as illustrated in Figure 5. Simulink is the master that sends selected signals to MSC.ADAMS at certain intervals. MSC.ADAMS calculates new dynamic situation and sends defined signals back to Simulink.

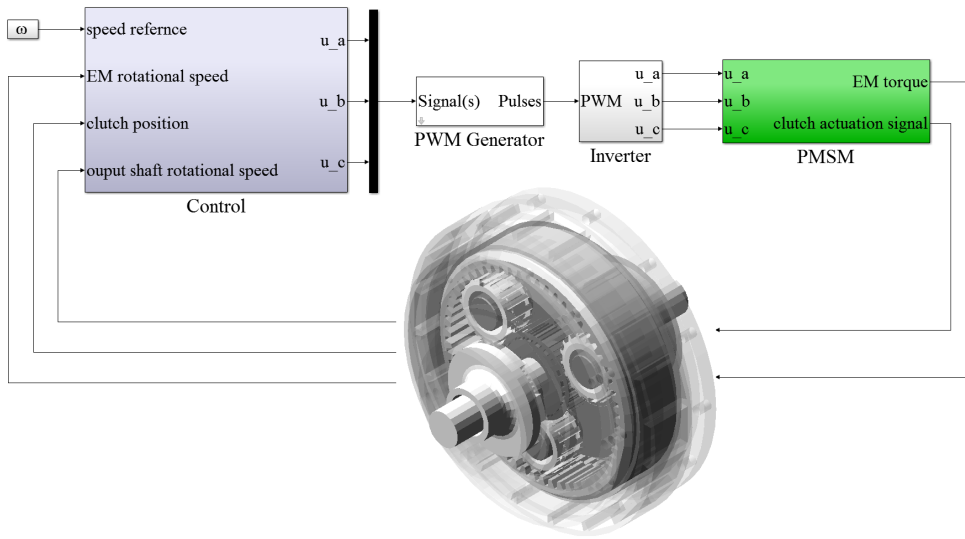


Fig. 4: Principle of the co-simulation model

The inputs for the multibody model are the torque of the electric motor and the actuation signals for the clutches. Clutch positions and rotation speeds of the electric motor and the output shaft are calculated and sent to the Simulink model.

Current vector control is used to control the electric machine current under inverter operational limits. Simulink will allow the usage of special algorithms such as maximum torque per ampere control below nominal speed and the field weakening at speeds higher than the rated one. Park-Clarke transformations are used to get the most simplified two-axis model for the electric machine and its control instead of three phase quantities. The equations for the PMSM can be, hence, simplified into

$$T = \psi_{PM} i_q + (L_d - L_q) i_d i_q \quad (3)$$

$$u_d = R_s i_d - \omega L_q i_q \quad (4)$$

$$u_q = R_s i_q + \omega \psi_{PM} + \omega L_d i_d \quad (5)$$

where

i_d, i_q d- and q-axes stator currents;

u_d, u_q d- and q-axes stator voltages;

L_d, L_q d- and q axes synchronous inductances;

ψ_{PM} flux linkage due to permanent magnet excitation;

R_s stator resistance;

T electromagnetic torque;

ω electrical angular frequency.

Now the current components can be controlled as pairs inside the voltage and current limits of the inverter at needed torque and speed state. Especially, below the rated speed the selection of the current component can be selected in a way which utilizes the reluctance and excitation torque of the machine in an optimal way. Electrical machine design details can be found from [9].

4. Results and analysis

In mechanical approach, the dynamic behavior of the system during the gear shifting is studied by using multibody system simulation software (MSC.ADAMS). The main focus is to observe the proper functioning and check the gear shifting controllability which is a determinant factor in the duty life of

the driveline. The duty cycle for the simulation is summarized in accelerating, operating in a constant speed, shifting and accelerating (Figure 5.a). In order to follow the duty cycle the electric motor accelerates from standstill to 1200 rpm in 45 ms. Due to the acceleration the applied torque on clutch 2 which is engaged with planet carrier (blue dashed line), is higher than the load in Figure 5.b. The electric motor operates at a constant speed and torque for 1.6 seconds while the drive shaft rotates at 330 rpm and delivers 188 kNm torque (Figure 5.b). After disengaging clutch 2, in 1 ms the rotor decelerates down to 270 rpm – that is 30 rpm lower than the drive axle. Then by the means of the thrust force of actuator 1, the drive shaft is engaged with the rotor through clutch 1 and direct drive mode is achieved immediately. The electric motor then continues accelerating till the end of the cycle.

Since the gear shifting process should be carried out in a small time period (Figure 6.a) any failure in the synchronization of the rotor and clutches leads to severe shocks and vibration (Figure 6.b) that, as a consequence, might lead to fatigue or fracture of the mechanical components.

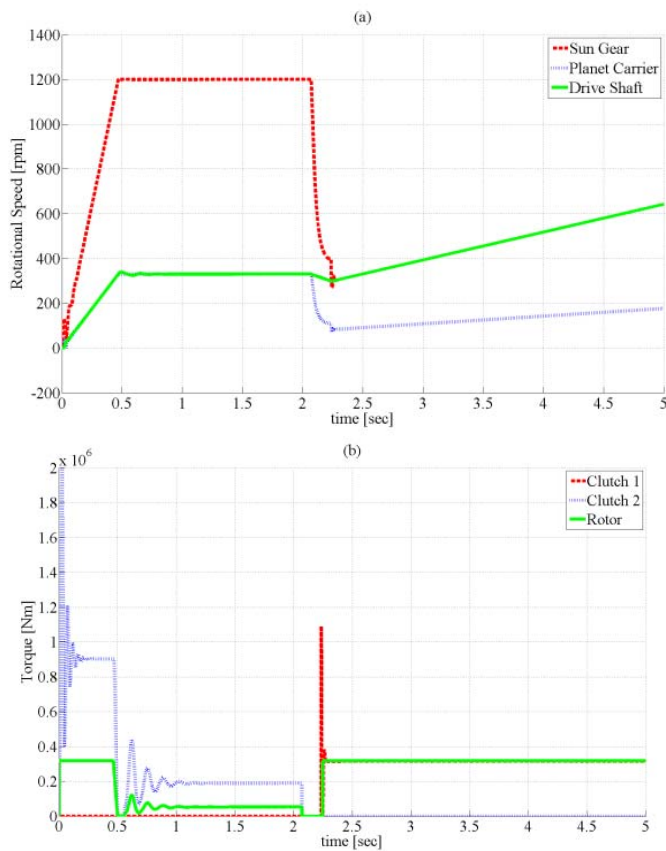


Fig. 5: Rotation speeds and torques during a gear shifting cycle.

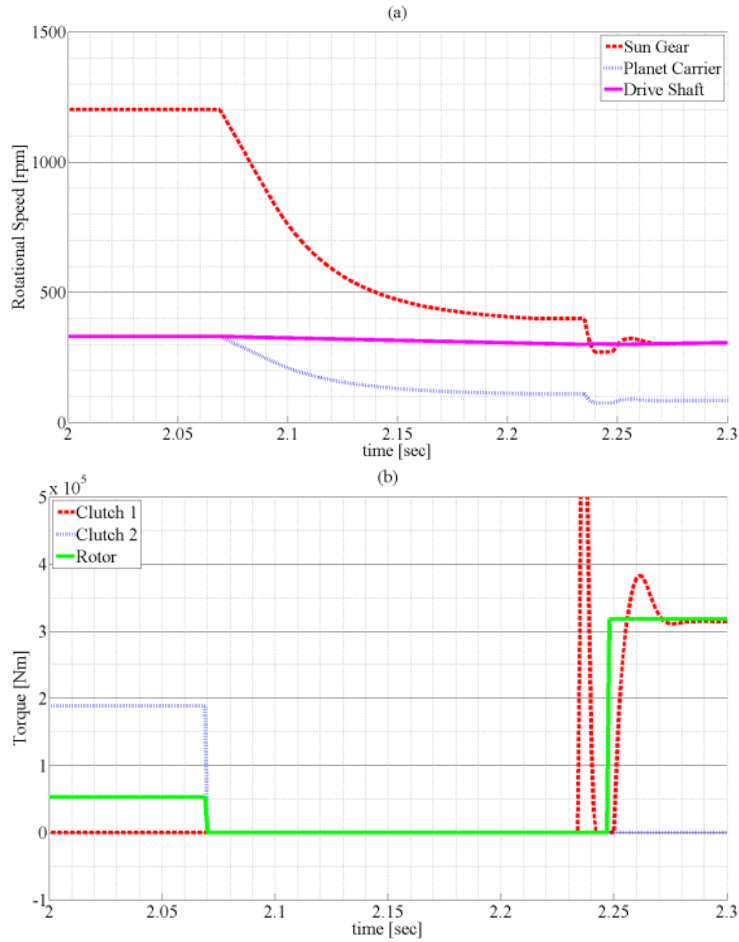


Fig. 6: While shifting: a) Speed variation b) Torque

The operation of the system is extremely dependent on the electric motor control and gear shifting control. Since the electric motor is modelled in MATLAB-Simulink a co-simulation environment was built to validate the compatibility of transmission and electric motor control. Hence, more detailed co-simulations were conducted.

In order to simulate the system in the new configuration of different software, a sample drive cycle is defined that by increasing and decreasing the imposed load over and below the electric motor critical power threshold and the gear shifting control activates. Whereas the proposed system can be employed in various applications, the proposed driving cycle is defined so that it can be regarded as benchmark.

The simulation is run for 4 seconds and there is interaction between Simulink and mechanical plant in ADAMS in every 10 microseconds. According to the defined sample drive cycle, three shifting signals are sent to clutches and as shown in Fig. 7, in every disengagement there is an overshoot in the sun gear rotational speed that illustrates the rotor speed increases dramatically when it is unloaded immediately. So the electric motor control should be modified to set the torque to zero before sending gear shifting signals to the clutches that not only decreases the tooth clutch sliding friction but also prevents immense shocks to the system.

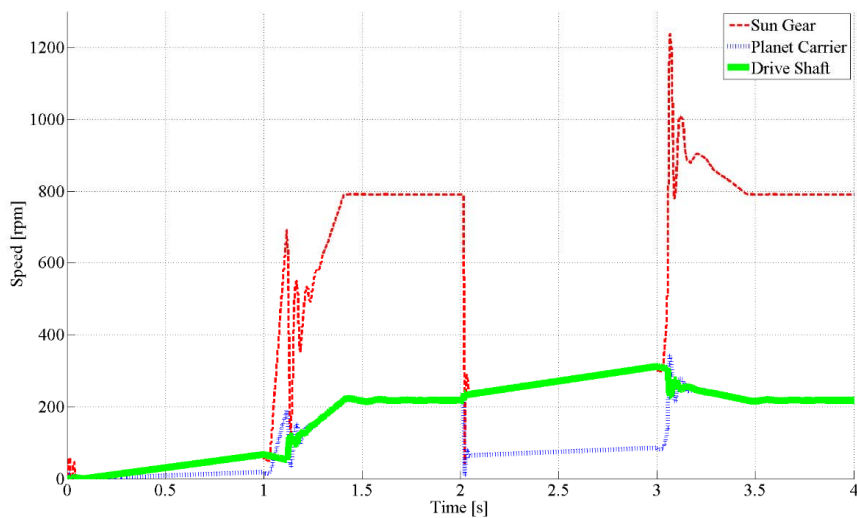


Fig. 7: Driveline components rotational speed during driving cycle

5. Conclusion

A clear need of an integrated two-speed gearbox and electric motor is identified for off-road working machine applications. The introduced new construction proposes a solution that saves space and allows full use of electric hub motors and full electric drivelines in off-road vehicles such as agricultural tractors. Operation of the introduced structure is studied using co-simulations. The results indicate that gear shifting is possible to conduct using the proposed approach; however the control of the electric motor and gear changing must be carefully designed in order to avoid high impulsive torques to mechanical components. Developed co-simulation tool can be used in the future to study different load conditions and to continue developing gear shifting control system. The model can be embedded also in a full vehicle model for studying the functionality and the drive behavior more closely and realistically.

References

- [1] X. Zhu, L. Chen, L. Quan, Y. Sun, W. Hua, Z. Wang, "A new Magnetic-Planetary-Geared Permanent Magnet Brushless Machine for Hybrid Electric Vehicle" IEEE Transactions on Magnetics, vol. 48, no. 11, pp. 4642–4645, 2012.
- [2] Peng Zhang, Gennadi Y. Sizov, Muyang Li, Dan M. Ionel, Nabeel A.O. Demerdash, Steven Stretz, Alan W. Yeadon "Multi-objective Tradeoffs in the Design Optimization of a Brushless Permanent Magnet Machine with Fractional-Slot Concentrated Windings", Proceedings of 15th European Conference on Power Electronics and Applications (EPE'13), Lille, France, 2013 pp. 2842 – 2849.
- [3] Z. Zhu and D. Howe, "Electrical machines and drives for electric, hybrid, and fuel cell vehicles," Proceedings of the IEEE, vol. 95, no. 4, pp. 746–765, 2007.
- [4] P. M. Lindh, H. K. Jussila, M. Niemelä, A. Parviainen and J.J. Pyrhönen, "Comparison of Concentrated Winding Permanent Magnet Motors With Embedded and Surface-Mounted Rotor Magnets" IEEE Transactions on Magnetics, vol. 45, no. 5, pp. 2085–2089, 2009.
- [5] M. Rahman, M. Masrur, and M. Uddin, "Impacts of interior permanent magnet machine technology for electric vehicles," in Electric Vehicle Conference (IEVC), 2012 IEEE International, pp. 1–5, 2012.

[6] J. Ahokas, "Traktorit ja työkoneet" [electronic article], accessed 10.10.2013, <http://www.energia-akatemia.fi/attachments/article/54/TraktoritJaTyokoneet.pdf>

[7] P. Lynwander, Gear Drive Systems: Design and Application, New York and Basel: Marcel Dekker, Inc. ISBN 0-8247-1896-8, 1983.

[8] "Adams" [Online]. Available: <http://www.mscsoftware.com/product/adams>. [Accessed: 12-May-2014].

[9] J. Montonen, S. Sinkko, P. Lindh, J. Pyrhönen "Design of a Traction Motor with Two-Step Gearbox for High-Torque Applications", To be published in ICEM-conference in Berlin, September 2.-5.9.2014.

Publication III

Gerami Tehrani, M., Montonen, J., Immonen, P., Sinkko, S., Kaikko, E., Nokka, J., Sopanen, J. and Pyrhönen J.

Application of Hub-Wheel Electric Motor Integrated With Two Step Planetary Transmission for Heavy Off-Road Vehicles

Reprinted with permission from

ASME Proceedings IDETC,

International Design Engineering Technical Conferences and Computers and Information in Engineering Conference.

Boston, USA, 2.-5.8.2015,

© 2015 American Society of Mechanical Engineers.

DETC2015-47030

**Application Of Hub-Wheel Electric Motor Integrated With Two Step Planetary Transmission
For Heavy Off-Road Vehicles**

Mohammad Gerami Tehrani
Department of Mechanical
Engineering
Lappeenranta University of
Technology
Skinnarilankatu 34
53850 Lappeenranta,
Finland
Email:
mohammad.gerami.tehrani@lut.fi

Juho Montonen
Department of Electrical
Engineering
Lappeenranta University
of Technology
Skinnarilankatu 34
53850 Lappeenranta,
Finland
Email:
juho.montonen@lut.fi

Paula Immonen
Department of Electrical
Engineering
Lappeenranta University
of Technology
Skinnarilankatu 34
53850 Lappeenranta,
Finland
Email:
paula.immonen@lut.fi

Simo Sinkko
unit Of Technology
Saimaa University Of
Applied Sciences
Skinnarilankatu 36
53850 Lappeenranta,
Finland
Email:
simo.sinkko@saimia.fi

Esa-Pekka Kaikko
Department of Mechanical
Engineering
Lappeenranta University of
Technology
Skinnarilankatu 34
53850 Lappeenranta,
Finland
Email:
Esa-Pekka.Kaikko@lut.fi

Jarkko Nokka
Department of Electrical
Engineering
Lappeenranta University
of Technology
Skinnarilankatu 34
53850 Lappeenranta,
Finland
Email:
jarkko.nokka@lut.fi

Jussi Sopanen
Department of Mechanical
Engineering
Lappeenranta University
of Technology
Skinnarilankatu 34
53850 Lappeenranta,
Finland
Email:
jussi.sopanen@lut.fi

Juha Pyrhönen
Department of Electrical
Engineering
Lappeenranta University of
Technology
Skinnarilankatu 34
53850 Lappeenranta,
Finland
Email:
juha.pyrhonen@lut.fi

ABSTRACT

An integrated electro-mechanical drive train component for heavy duty vehicles in off-road applications is presented. The component utilizes a two-step transmission and a tooth-coil permanent magnet motor and has compact size enabling in-wheel installation. The driveline design procedure is surveyed to explore the advantages of a geared electric motor in electric drivelines. Multibody dynamic simulation is applied to verify the functionality of the driveline. A vehicle generic model that is compatible with a multibody simulator program is developed to describe the performance of the proposed driveline in different vehicles. A co-simulation procedure is applied to combine the electric motor and vehicle body simulation models. It is shown that the co-simulation can be performed in real-time, thus

enabling a human driver to control the vehicle. A comparison is made of the rear wheel drive and wheel mounted electric motor from the efficiency and performance points of view. The power consumption of vehicles with different driveline architectures is calculated to diagnose the weak points of the system and enhancement solutions are proposed.

INTRODUCTION

Application of electric drivelines in heavy off-road vehicles is becoming a topic of growing interest because of their many advantages compared to conventional drivelines, namely, greater efficiency, reduced local emissions and silent operation. Nowadays most heavy duty off-road vehicles, such as

agricultural tractors, wheel loaders and excavators, have electrically controlled hydraulic or hydro-mechanical drivelines.

Pure hydraulic transmission typically means a hydrostatic transmission. The mechanical power of the diesel engine is converted into hydraulic power with a hydraulic pump, and then this hydraulic power is converted back to mechanical power with a hydraulic motor that directly drives the shafts or wheels. This kind of a transmission can be found, for example, in excavators, forest tractors and combine harvesters. However, the efficiency of hydrostatic transmission is low, around 70% at the optimal operating point and in partial load situations significantly lower [1]. The benefits of hydrostatic transmission are good controllability, simplicity and that it is a proven technology with a relatively low price.

The architecture of a conventional heavy-duty off-road vehicle drive line is made up of a combustion engine and a hydraulic pump/motor that is capable of producing consistent and steady output power despite relatively irregular engine operation [2]. The optimum operation point of a hydraulic pump/motor is where maximum torque is applied while the rotation speed is low. Consequently, sole hydraulic power transmission is not suitable for high speed operation, e.g. transportation [3]. Modern agricultural tractors have either continuously variable transmissions (CVT) or electrically controlled gear shifting (powershift). In both cases, hydraulics is present and transmissions include many wet sliding clutches. The efficiency of these kinds of transmissions is quite poor, even when the main power line is mechanical. On the other hand, this arrangement makes it easy to achieve a wide operational range so that an optimal speed can be found for every task of the vehicle [4].

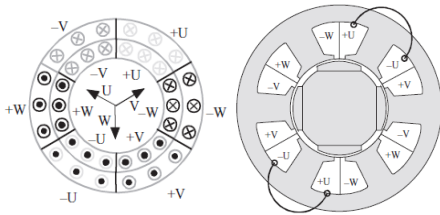


Figure 1 Different winding configurations: Distributed winding (left) and TCPMSM (right) [4].

In off-road mobility, which is characterized by unpredictable terrain, the contribution of each wheel needs to be determined separately to control the vehicle along the desired trajectory. In conventional multi-wheel drive vehicle drivelines, torque is distributed to the wheels by means of differentials, and the amount of torque dedicated to each wheel is adjusted by frictional plates or by applying resistive force on individual wheels. The vehicle traction control system is based on the friction level on each wheel, which can be predicted or sensed by the speed difference of wheels connected to a common differential [5]. In both power distributing method, the suitable torque is regulated by manipulating the torque/speed ratio at each

power dividing unit. , the need for series division of power necessarily makes the control system rather complicated.[6]. The control of electrical systems is easier and faster than control of mechanical systems, so utilization of a hub-wheel electric motor is appropriate not only in the sense of controllability but also because it enables improvement in the efficiency of the driveline by optimizing the torque delivery on the wheels [7].

Typical applications of heavy off-road vehicles require that the electric drive line must be capable of providing seamless torque at low speeds, which is a task to which electric motors are well suited. The output torque of an electric motor is highly dependent on the electric motor rotor dimensions, and in order to overcome wheel radius limitations, a planetary gear train is usually integrated to increase the torque at low speeds.

An electric motor alone cannot normally be used as a traction motor of heavy machinery without the support of a gearbox. The torque demand in off-road heavy machinery devices varies in the range of 1:20, when the highest speed operation in the range of 1:20, when comparing torque at highest speed operation in the field and highest torque at start-up Ideally, an off-road traction motor drive system should provide a constant power drive at a wide speed range. An electrical machine may be temporarily overloaded at 2 – 3 times the rated torque of the machine, and at twice the rated speed, the machine can normally produce 50 % of the rated torque. A suitable Tooth-Coil Permanent Magnet Synchronous Motor (TCPMSM) is able to meet the demands of such operations [8]; for which reason, a TCPMSM was selected and designed for the high-performance system discussed in this work. The difference between a TCPMSM winding configuration and traditional distributed winding is illustrated in Figure 1.

Figure 2 presents a four-quadrant operation efficiency map for a hub-wheel motor working on a direct gear. Such efficiency maps can be used for instantaneous efficiency calculation of electric motors.

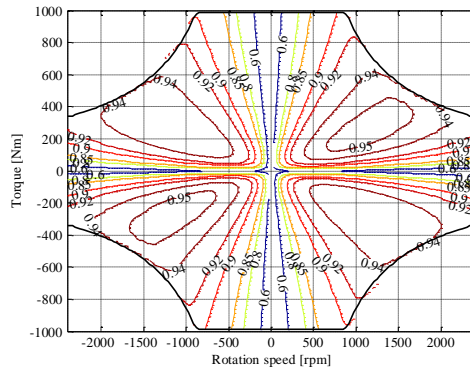
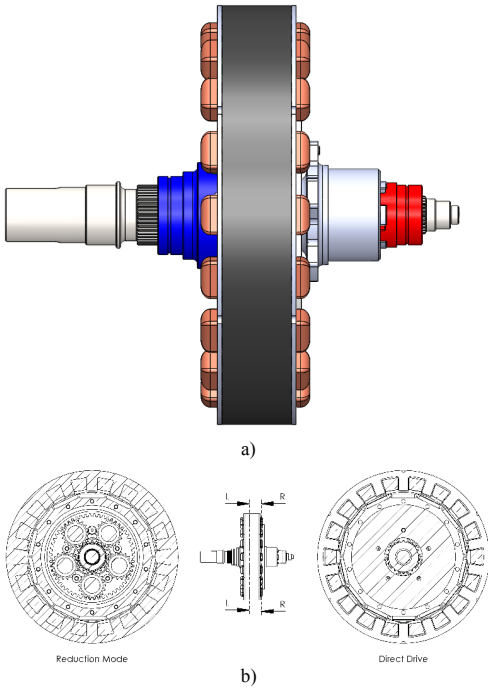


Figure 2 Four-quadrant operation efficiency map of the hub-motor in torque-speed range. The map presents the area of direct gear.

STUDIED DRIVELINE

The studied driveline is a novel architecture consisting of a multiple-pole tooth-coil permanent magnet synchronous electric motor integrated with a planetary gear system (later InHuGOR, i.e. Integrated Hub-Gear Off-Road). Such a motor design allows the planetary gear to be located inside the electric motor rotor as the rotor yoke is fairly and a suitably large space can be found.

The layout of InHuGOR is presented in Figure 3 and two driving modes are also given in cross section view. The operation of the clutch mechanisms is such that in neutral drive mode both the red and blue dog clutches are disengaged and idling. Once the reduction driving mode is selected, the red clutch will pair with the sun gear that is connected to the electric motor. Once the reduction mode has been activated, the blue clutch will engage to the planet carrier. If the shifting is applied while the output shaft is rotating, either for reduction or direct drive mode activation, the electric motor should synchronize the rotor speed with respect to the aimed mode, since there is no mechanical power decoupler or speed synchronizer.



**Figure 3 a) InHuGOR layout depicting the dog clutches
b) InHuGOR cross section**

Earlier study [9] analyzed the functionality of the gear shifting procedure using a co-simulation approach in which a detailed mechanical model and an electric drive and control

model were analyzed simultaneously. In [9] a mechanical model of the gear box with clutches was implemented in a multibody simulation software application (MSC.ADAMS [10]). The multibody simulation model included kinematical descriptions as well as masses and mass moments of inertias of gear-box components. Operation of the clutches was described using contact force elements. The simulation model of the electric motor, motor controller, power electronics and control logic of the whole system was implemented in Simulink. The main finding of the study was that it is possible to perform gear shifting as planned, however, electric synchronization and control play a significant role in a smooth operation.

In this paper we present the application of InHuGOR in real-time vehicle simulations. It is possible to connect the real-time simulation model to a motion platform so that realistic driving conditions can be tested.

The behavior and the nominal point of the motor are shown in Figure 4. The figure also gives power curves for the drive system at a 3:1 gear ratio. The figure shows that the geared system is capable of providing a per-unit speed range from 0 to 2 and the per unit torque ranges from 0 to 9. As the highest speed torque is 0.5 per unit, the torque ratio of the drive system is $9:0.5 = 18$. With a 3:1 gear ratio, the electric traction motor is, therefore, capable of meeting the torque range needed in a heavy machinery drive. The highest continuous output torque is limited to $T = 3 T_n$ of the motor, and in that case the torque ratio will be $3:0.5 = 6$.

The design of the integrated system includes oil splashing cooling of the electric motor, enabling high torque densities and high overloading capability at the lowest speeds.

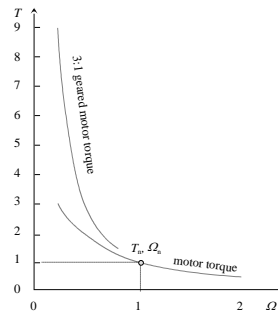


Figure 4 Constant power curves of the studied traction motor and geared traction motor.

Figure 5 shows the electromagnetic capabilities of the hub motor with two different gears using fully the inverter voltage and current constraints. Table 1 presents principal design parameters of the studied electric motor and, correspondingly, Table 2 shows the performance characteristics. This electric motor has been previously studied in more detail in [11].

As can be seen from **Table 1**, the large diameter and short axial length of the motor favors multiple poles to get the best

torque output. This particular TCPMSM was selected based on its mostly sinusoidal back-electromotive force waveform, inherently low cogging torque and torque ripple, good efficiency and sufficiently large field weakening range.

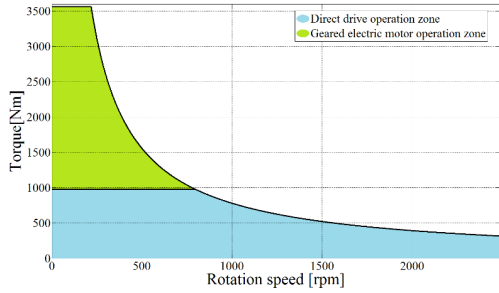


Figure 5 Torque capabilities of the studied hub-wheel PMSM with two-step planetary gear.

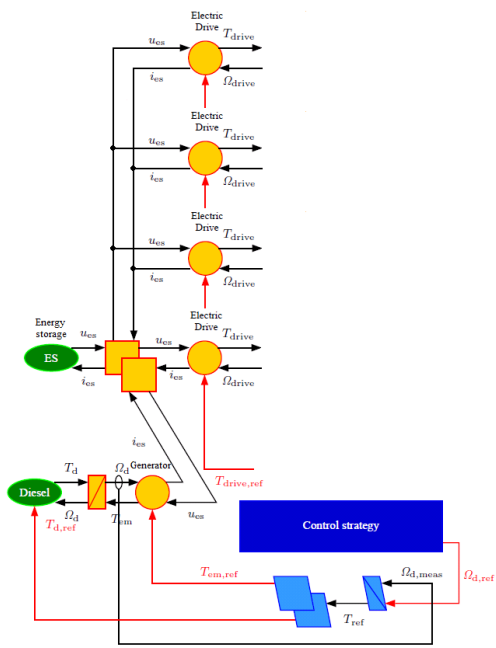


Figure 6 Energetic Macroscopic Representation (EMR) of electrical components in the electrical driveline and hybrid system.

Figure 6 provides an Energetic Macroscopic Representation (EMR) [12] of the electrical components in the electrical driveline and hybrid system. EMR is an energy-flow based graphical method to illustrate energy and power flow in a complex electromechanical systems. The electrical driveline consists of an electric drive, which includes an electric motor and a frequency converter. The diesel generator set produces all the electric energy needed in the electric drive. Depending on the configuration, the energy storage can be either a battery or a supercapacitor.

Table 1 Principal design parameters

Parameter	value
Slots per pole and phase, q	0.43
Stator slots	18
Poles	14
Length of the stator stack [mm]	75
Stator outer diameter [mm]	454
Stator inner diameter [mm]	346
Rotor outer diameter [mm]	340
Rotor inner diameter [mm]	280
Number of coil turns in phase N_{ph}	138
Phase resistance [p.u]	0.02

Table 2 Performance characteristics at the rated point of the PMSM

Parameter	value
Rated output power [kW]	40.8
Rated speed [min^{-1}]	1200
Rated torque [Nm]	324
Estimated efficiency Sinusoidal supply	0.957
Power factor	0.92
Rated current [A]	67
Back-emf at 1200 min^{-1} [V]	203
Current density at the rated point [A/mm^2]	4

The drive transmission of the vehicle is implemented using a two-step planetary gear and fixed planet gear. Figure 7 illustrates the simplified EMR of the drive transmission of the vehicle.

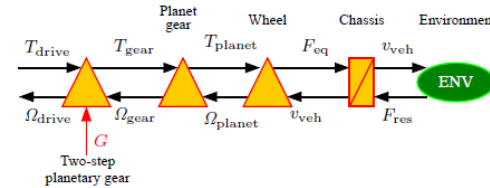


Figure 7 Simplified EMR of vehicle drive transmission.

VEHICLE SIMULATION

In the employed real-time simulator, a multibody system approach is applied for vehicle dynamic modeling. A multibody system may consist of both rigid and flexible bodies, which are connected to each other using kinematic joint constraints, while force components are used to describe the actuators. The bodies compose the kinematic chains whose behavior is analyzed in the simulation [12]. The simulation environment used in this study can be used for simulations of multibody systems containing also mechatronic components such as hydraulics, actuators, motors and transmissions.

In order to validate the applicability of the proposed driveline in different vehicle architectures, i.e. electric drivelines as well as hybrid or all electric drivelines, a generic model has to be developed. The generic model should be capable of modifying all the parameters in the integrated simulation software, which in this study are Matlab Simulink and Mevea. The advantages of utilizing a parametric and dynamic design are that the model does not need to be designed from scratch every time and further optimization will proceed quite fast. The main purpose of the generic model is to hasten the modeling processes of similar products. Clearly, the benefits of a generic model are greater when a variety of products is to be modeled. [13]

As can be seen in Figure 9, the electrical components are modelled in Simulink while the mechanical components are modelled inside the Mevea program. The co-simulation is timed from the multibody dynamic simulation side and is synced with its time step. During this time step, the positions, orientations and velocities of the simulated bodies are calculated. The same method is applied for the hydraulic system as well as mechanical powertrain values. Once in every time step the multibody dynamic simulation sends the output values of the external interface to Simulink and waits for the return value. During this time Simulink calculates the corresponding number of calculation loops to match the time. In this way the simulation progresses conjointly between the two programs.

The simulation process is functionalized using the Mevea and Matlab/Simulink interface. The electric motor is modeled inside the Matlab script and only torque and rotational speeds are modeled inside the Simulink model. This approach makes the simulation process faster; inductances, flux linkages and currents etc. are inside the script and Simulink uses only efficiency maps. All the other electrical components are handled in the same way.

In this study, an agricultural tractor is taken as an example heavy-duty off-road vehicle for comparison of the power consumption of two different driveline configurations; the first configuration comprises two double powered InHuGOR in the rear wheels, and the second configuration has an InHuGOR component in all four wheels. The ambient situation and vehicle parameters [14] shown in Table 3 are constant for both cases while the propulsion method is changed. The above-mentioned tractor is implemented in the real-time simulator environment as given in Figure 8.

In order to develop a test setup, a modern software-in-loop (SIL) and hardware-in-loop (HIL) simulator was built by cooperation between Lappeenranta University of Technology (LUT), heavy duty electrical and hybrid electrical driveline

manufacturer and a simulation product provider. In this section a combined (SIL) simulation approach is applied as well as the generic model that constructs the different combinations of the vehicle model and simulation. A solution for a hybrid working machine system simulation is introduced. The system includes a human-machine interface (HMI) with high quality virtual reality modeling of dynamic behavior of mechanical components of working machines (WM) and tire friction modelling as well as electrical drive models including converter control [15].



Figure 8 Real-time multibody dynamics simulator environment

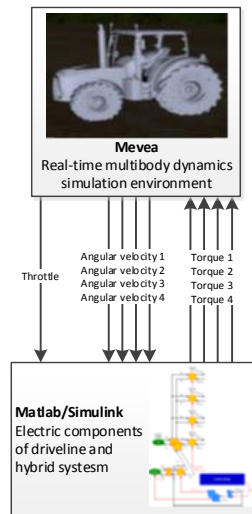


Figure 9 Interface between Mevea simulation environment and Matlab/Simulink.

In the test setup, driving commands to the sample vehicle are defined by a joystick. Based on the throttle angle, the corresponding torque is regulated by a PI controller and the reference torque signal is sent to the electric model in Simulink, as shown in Figure 10. Subsequently, the Simulink model of the electric motor calculates the corresponding torque on the wheels. The calculated torque is then sent to the multibody dynamic simulator as an input. Since the electric motor is torque/speed controlled, the effect of the torque/speed of the wheel is sent back to the Simulink model as feedback.

Table 3 Sample tractor parameters

Parameter	value
Air density in (kg/m ³)	1.225
mass (kg)	6500
frontal area (m ²)	6.8
Air drag coefficient	0.60
Tire rolling resistance coefficient	0.8
Dynamic rolling radius of the front tire (m)	0.67
Dynamic rolling radius of the rear tire (m)	0.94

Two different driveline configurations are objected in the simulation to achieve results in a drag test. In the drag test, the vehicle accelerates at full throttle from the very first moment. In the first driveline, i.e. four-wheel drive (4x4), four InHuGORs are attached to the wheels via the drive shaft. In this driveline, despite the fact that every single wheel can provide similar maximum torque, the traction force is not the same due to differences in tire radiuses, which force some electric motors to operate in the transient power area, where the output power is not constant. Thus, in sudden acceleration, front tires have greater likelihood of slipping.

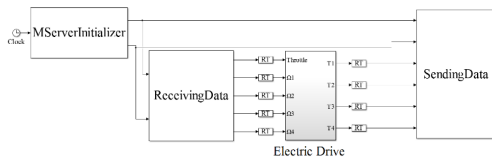


Figure 10 Co-simulation with Simulink

The latter driveline model, i.e. rear wheel drive (RWD), consists of two InHuGORs with double rated power mounted on the rear wheels, providing the same total accessible power as hub-motors on four-wheels. Some minor simplifications are applied in modeling the double power InHuGORs, such as adaptations to rotor mass and electric motor efficiency, although these changes do not have a significant effect on the results. The rotor mass is negligible compared to the wheel complex mass and full throttle operation efficiency is almost the same in the double rated power electric motor. The simulation track is dry asphalt and tire dynamic friction coefficient is set to 0.8. In the initial moments that the model is created in the simulator environment, it has some initial speed in the opposite direction of the track, consequently around the first second of the simulation, the speed value in Figure 11 is negative. The top

speed in this simulation is 115 km/h, which may not be suitable for agricultural tractors, although the results can be valid for other vehicle types.

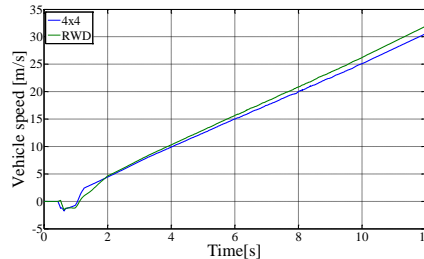


Figure 11 Linear speed of two different drivelines

Based on the rear and front tire radii and widths, chassis geometry and a center of mass location that is 10% inclined to the rear, the normal force at tire contact and the rolling friction of the rear tires are higher than those of the front tires. The effect can be seen in Figure 11, where the vehicle linear speed with RWD driveline is higher than the 4x4 model, whereas the acceleration is pretty much the same, because of initial tire slipping in 4x4 mode. The instant power consumption of electric motors on each wheel (Front-Left, Front-Right, Rear-Left, Rear-Right) is plotted in Figure 13 for both proposed drivelines. Comparing plots a and b in Figure 13, it can be seen that the cumulative power consumption is almost the same in both 4x4 and RWD but the tire slipping duration is double in RWD because of the two times higher power of the electric motors in this mode.

Figure 12 shows an example of tire modeling in which the wheel profile is defined with 3 splines. Here, the center of the wheel has the biggest radius while each side of the wheel has a smaller radius. In this study, a symmetric tire with 5% radius increment at the middle is modeled. In Figure 13 (b), the power consumption on the rear wheels is slightly higher, because the lower slippage of the rear wheels leads to more electric power consumption than for the front wheels, which can rotate with less resistive force. The total power consumption of the modeled tractors is calculated based on the torque on the wheels and the drive shaft speed and is given in Table 4.

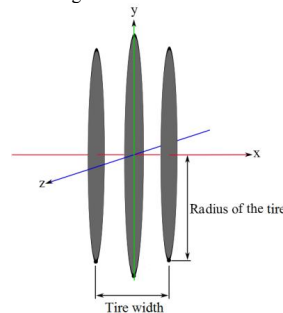


Figure 12 Tire profile described with three spline points.

Table 4 Power consumption on wheels (kWh)

	4x4	RWD
Front-Left	0.9323	-
Front-Right	0.9293	-
Rear-Left	1.0270	1.2319
Rear-Right	1.0280	1.2323
Total	3.9166	2.4643

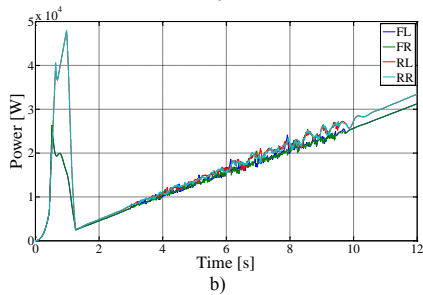
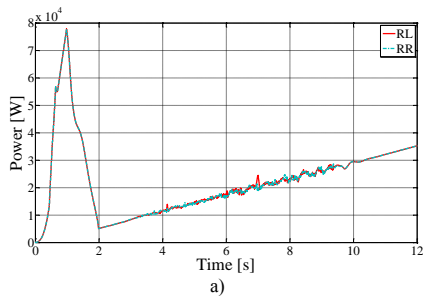


Figure 13 Instant power consumption on wheels: a) rear wheels drive, b) four-wheels drive

When considering the power consumption plots, the necessity of an efficient traction control system is clearly evident. According to the results in Table 4, the total energy efficiency of the RWD driveline is still better than that of the proposed 4x4 driveline, when no mechanical differential imposes extra power loss to the system without an effective traction control that prevents over-spinning of tires.

Gear shifting capability of the proposed model is not applied in this simulation, since the traction control is not embedded in the system and higher torque at low speeds will lead to more power loss. An accurate dynamic model of the proposed electric motor and integrated gear train needs to be developed to generate more realistic simulation conditions. However, the use of more complex models and the inclusion of non-linearity in the system bring drawbacks in the form of more time lag in the real-time

simulation, and a need for more accurate tire modelling and tire contact modeling.

CONCLUSIONS

This paper presents a novel combination of an electric drive and a mechanical transmission that is embedded inside the wheel hub. The advantages of the proposed system from the performance and efficiency points of view are explained and its functionality is verified by multibody system analysis.

The applicability of utilizing the presented system in electric mobility, specifically in heavy off-road vehicles, is studied and an all-electric driveline based on InHuGOR designed and described. Real-time vehicle simulation software is then employed to evaluate the designed driveline in the virtual world. Two different all-electric driveline architectures are subjected to comparison at the power consumption level. The better operation of individually controlled wheels is explained and the lack of a traction control system shown to manifest itself in inefficient operation of the hub-wheel electric motor. Optimum performance of the designed driveline can be achieved by development of a dynamic model of the InHuGOR components and an effective traction control strategy.

Acknowledgments

The authors would like to thank the Centennial Foundation of the Technology Industries in Finland and Tekes – the Finnish Funding Agency for Technology and Innovation for their financial support.

- [1] H. E. Merritt, in *Hydraulic Control Systems*, John Wiley & Sons, 1967, pp. 228–229.
- [2] G.-Q. Liu, Y.-C. Yan, J. Chen, and T.-M. Na, “Simulation and experimental validation study on the drive performance of a new hydraulic power assist system,” in *2009 IEEE Intelligent Vehicles Symposium*, 2009, pp. 966–970.
- [3] B. Wu, C.-C. Lin, Z. Filipi, H. Peng, and D. Assanis, “Optimal power management for a hydraulic hybrid delivery truck,” *Veh. Syst. Dyn.*, vol. 42, no. 1–2, pp. 23–40, 2004.
- [4] J. Montonen, S. Sinkko, P. Lindh, and J. Pyrhonen, “Design of a traction motor with two-step gearbox for high-torque applications,” in *2014 International Conference on Electrical Machines (ICEM)*, 2014, pp. 1069–1075.
- [5] J. P. Gray, V. V. Vantsevich, and A. F. Opeiko, “6x6 UGV: Stochastic Dynamics Fundamentals for Mobility Estimation,” in *ASME 2014 International Design Engineering Technical Conferences and Computers and Information in Engineering Conference*, 2014, pp. V003T01A023–V003T01A023.

- [6] V. V. Vantsevich, "Multi-wheel drive vehicle energy/fuel efficiency and traction performance: Objective function analysis," *J. Terramechanics*, vol. 44, no. 3, pp. 239–253, Jul. 2007.
- [7] V. V. Vantsevich, "Power losses and energy efficiency of multi-wheel drive vehicles: A method for evaluation," *J. Terramechanics*, vol. 45, no. 3, pp. 89–101, Jun. 2008.
- [8] P. Ponomarev, P. Lindh, and J. Pyrhonen, "Effect of Slot-and-Pole Combination on the Leakage Inductance and the Performance of Tooth-Coil Permanent-Magnet Synchronous Machines," *IEEE Trans. Ind. Electron.*, vol. 60, no. 10, pp. 4310–4317, Oct. 2013.
- [9] J. Pyrhönen, T. Jokinen, and V. Hrabovcová, "Front Matter," in *Design of Rotating Electrical Machines*, John Wiley & Sons, Ltd, 2008, pp. i–xxv.
- [10] "Adams" [Online]. Available: <http://www.mscsoftware.com/product/adams>. [Accessed: 16-Jan-2015].
- [11] S. Sinkko, J. Montonen, M. G. Tehrani, J. Pyrhonen, J. Sapanen, and T. Nummelin, "Integrated hub-motor drive train for off-road vehicles," in *2014 16th European Conference on Power Electronics and Applications (EPE'14-ECCE Europe)*, 2014, pp. 1–11.
- [12] A. A. Shabana, *Dynamics of Multibody Systems*. Cambridge: Cambridge University Press, 2005.
- [13] G. W. Winch and D. J. W. Arthur, "User-parameterised generic models: a solution to the conundrum of modelling access for SMEs?," *Syst. Dyn. Rev.*, vol. 18, no. 3, pp. 339–357, 2002.
- [14] M. Gerami Tehrani, J. Kelkka, J. Sapanen, A. Mikkola, and K. Kerkanen, "Transmission configuration effect on total efficiency of Electric Vehicle powertrain," in *2014 16th European Conference on Power Electronics and Applications (EPE'14-ECCE Europe)*, 2014, pp. 1–9.
- [15] J. Montonen, J.-H. Montonen, P. Immonen, K. Murashko, P. Ponomarev, T. Lindh, P. Lindh, L. Laurila, and J. Pyrhonen, "Electric drive dimensioning for a hybrid working machine by using virtual prototyping," in *2012 XXth International Conference on Electrical Machines (ICEM)*, 2012, pp. 921–927.

Publication IV

Gerami Tehrani, M., Kelkka, J., Sopenen, J., Mikkola, A. and Kerkkänen, K.
**Electric Vehicle Energy Consumption Simulation by Modeling the Efficiency of
Driveline Components**

Reprinted with permission from
SAE International Journal of Commercial Vehicles
Vol.9, no. 2016-01-9016, pp. 31-39,
©2016, SAE.

Electric Vehicle Energy Consumption Simulation by Modeling the Efficiency of Driveline Components

Mohammad Gerami Tehrani
Lappeenranta University of Technology

Juuso Kelkka
Valmet Automotive Inc

Jussi Sopanen, Aki Mikkola, and Kimmo Kerkkänen
Lappeenranta University of Technology

ABSTRACT

The feasibility of improving the energy efficiency of Electric Vehicles (EV) by manipulating operation points by means of a variable transmission is investigated with an efficient mathematical model of power losses in all driveline components. Introduced model can be solved in real-time making it possible to embed it to a control scheme of EV. Empirical test results are employed to derive the efficiency of the power electronics and electric motor at operation points while the mechanical power losses are predicted by a comprehensive and generic formulation for efficiency analysis. The simulation model used comprises electrical component efficiency, drivetrain inertias, gearbox efficiency, regenerative braking, and gear ratio selection. Three different transmission types are studied in this work; a single reduction gear, a five-step gearbox and an Infinitely Variable Transmission.

CITATION: Gerami Tehrani, M., Kelkka, J., Sopanen, J., Mikkola, A. et al., "Electric Vehicle Energy Consumption Simulation by Modeling the Efficiency of Driveline Components," *SAE Int. J. Commer. Veh.* 9(1):2016, doi:10.4271/2016-01-9016.

INTRODUCTION

Power consumption in Electric Vehicles (EV) is a major concern in driveline architecture design as it affects the life cycle and trip range of the EV. Permanent Magnet Synchronous Motors (PMSM) are commonly applied in electric driveline design because of their ability to deliver high torque and their compact size as well as constant power at high speeds. Furthermore, since the traction control method in EVs is Direct Torque Control (DTC), PMSM can be considered an optimal option because they can be controlled fast and efficiently [1]. Unlike Internal Combustion Engines (ICE), where maximum torque and power are produced at high rotation speed, in PMSM maximum torque is available even at the lowest rotation speeds allowing the power production to be constant.

In most EVs currently available, variable transmission is omitted from the powertrain because, from the performance point of view, the output power of PMSM is constant while the output torque is fixed. However, EV powertrain efficiency is a significant factor that cannot be neglected. A technical and financial comparison of conventional and equivalent hybrid and fully electric vehicles in different classes is presented for the Australian market in [2][3].

In parallel hybrid EVs, use of a combination of two or more propulsion sources permits management of the operation of the electric motor and ICE at optimal efficiency [4]. By contrast, in series

hybrid and all-electric drivelines, the electric motor has to spin at the corresponding road speed regardless of the demanded torque. In view of this characteristic of PMSM, conventional transmission is not required because the electric motor can provide similar power at different speeds. However, electric motor efficiency is not homogeneous over equivalent power points, which means that although the same power can be achieved by different torque-speed combinations, the efficiency can vary by up to 30% [5]. Improving the electric motor efficiency (without consideration of auxiliary components) by shifting the operation point along constant power curves by means of a variable transmission is studied in [6][7][8].

Definitive conclusions on the overall efficiency of the driveline cannot be drawn if power losses from the transmission, e.g. the effect of friction, are not taken into account. Thus, a precise model of the gearbox is needed to be able to predict power dissipation.

With this goal in mind, the study by [9] can be taken as a platform for development of a gearbox model and the friction coefficient formulation proposed by [10] applied. In the power loss prediction model developed by [9], the friction coefficient is considered constant while in more recent studies, the friction coefficient value varies according to the applied torque and operation speed. To be able to monitor how power losses due to downstream components in the driveline compromise the total efficiency and trip range of an EV

requires an agile mathematical model that predicts both electrical and mechanical efficiency instantaneously [11]. Such a model would enable assessment of the feasibility of applying a variable transmission in an EV driveline [12].

To overcome power dissipation in mechanical linkages and electrical components, the amount of power required in each driveline component should be somewhat higher relative to the previous stage. In other words, every component in the driveline flow chart has a value for its efficiency which compensates the losses while transmitting the power. The total efficiency of the driveline is a multiplication of the efficiency of the mechanical and electrical components.

The efficiency drop occurs principally in the electric machines, e.g. in the electric motors in which the electric power is converted to mechanical power. In electric machines, where the electric power - a product of current I and voltage U - is converted to the mechanical power - torque τ times angular velocity ω - some portion of power dissipates via both electrical and mechanical components.

In order to calculate the total efficiency, power extracted from the batteries compared to power exerted on the wheels should be derived, for both mechanical and electrical efficiency, at any arbitrary operation point. Any proposed modification to improve total efficiency should consider all factors in parallel [13]. For example, minimizing the power loss in the power electronics, including both switching and conduction losses, while modifying electric drive efficiency according to the operation point may improve the driving range [14]. However, optimizing the driving range parameter may compromise the efficiency of other stages, as is clear from discontinuous efficiency waterfall modeling.

Another component that has a determinant effect on driveline efficiency is the gearbox through which the power is transmitted while the torque and speed vary. In the context of this study, unlimited combinations of torque and angular velocity are possible in selection of a specific amount of power, whereas the efficiency of the electrical or mechanical systems fluctuates, with one or the other system showing greater efficiency. Thus, the operation point at which total efficiency of the driveline results in the highest value determines the optimum operational point from an efficiency perspective.

The objective of this study is to assess the feasibility of implementing a variable transmission in EV driveline architecture, from the efficiency point of view, by developing an efficiency model for the gearbox that is a function of torque and angular speed to predict power losses in accordance with the operating point of the electric motor. The efficiency maps of electric components such as the power electronics and the electric motor are taken from manufacturers' empirical test results and the power losses in the gearbox are predicted by formulation in [9]. The power losses resulting from components that function in the same way in the driveline whether a variable gearbox or a constant reduction gear is included, are considered as constant.

The rest of the paper is constructed as follows. The next section considers theoretical aspects, in particular mechanical losses, which are divided into load-dependent losses and spin losses. Section 3 presents the simulation model, which is a comprehensive EV driveline model built by applying a novel real-time efficiency calculator for the gearbox. The proposed generic model is not only compatible with all kinds of geartrain but can also be used for Continuously Variable Transmission (CVT) and Infinitely Variable Transmission (IVT), thus enabling power consumption comparisons between different transmission configurations. The studied structure is presented in section 4. Section 5 presents the simulation results, which are analyzed with the aim of finding optimal performance points and assessing the feasibility of adding a variable transmission to the EV driveline. The paper ends with a short section giving conclusions of the study.

GEARBOX MODELING

In mechanical power transmission by means of a geartrain, gear teeth deliver the power by rolling and sliding over each other. Although tooth surfaces look plain and fully burnished in macro view, they are ragged surfaces whose asperities resist sliding. As a result, a portion of power is lost as heat, wear and noise.

Losses due to friction in support bearings and the gear mesh are called load-dependent losses, and losses that come from air resistance and the lubricant used are termed spin losses. The challenge in formulation of load-dependent losses comes from the need to derive a friction coefficient that varies during the mesh cycle. In Coulomb's law, the friction coefficient (μ) is a constant value and the resistive force is dependent on normal force variation. In gear tooth pairing, the friction coefficient varies according to the mesh cycle sequence. For this reason, the time dependent method for calculating the friction coefficient proposed by [10] is applied in this work in a modified version of Coulomb's law for friction by [15] that was developed for estimating the resistive force. The methodology developed by [16] is applied in calculation of spin losses, which are divided into oil churning and windage power losses, which represent power losses due to the interaction of individual gears with lubrication fluid and pumping of oil at the gear mesh.

In order to have a model that considers both rolling and sliding interaction between the gear teeth, a modification of Coulomb's law is applied to obtain the equivalent kinetic friction coefficient. Resistive frictional torque in the supporting bearings is also considered based on the construction of load carrying shafts and gears in the gearbox. The load-dependent power losses are defined as a function of rotating speed and applied torque, while spin losses vary by rotational speed.

For smoother and more efficient operation, a gear box needs to be lubricated. The thickness of the formed lubricant film that eases the rolling and sliding movements of parts is dependent on the applied pressure between the solid surfaces. At excessive pressures and point contacts, the lubricant film can become ruptured, so in order to select a suitable lubricant, the mean operational pressure needs to be calculated. There are three types of solid-to-solid sliding condition: dry sliding, fully lubricated sliding and semi-lubricated sliding.

Although using lubricant fluid with high viscosity results in thicker films and decreases the friction coefficient, it increases the rolling (pumping) resistance [17].

By considering the lubricant as a Newtonian fluid, the rolling losses (P_R) due to hydrodynamic resistance can be categorized as oil drag and oil pumping losses, both of which are dependent on the lubrication type, i.e. whether an oil jet or oil bath is used.

Rolling (or pumping) loss is the power required to draw and compress the lubricant to form a pressurized oil film that separates the gear teeth in order to make the contact surface smoother and, thus, reduce friction. At light loads, the rolling loss is a major portion of the system losses.

A number of friction models have been proposed for calculation of the friction coefficient, such as the Coulomb Model, the Benedict and Kelley Model, Xu's Full Model and the Smoothed Coulomb Model, based on Anderson and Loewenthal, it is clear that the friction coefficient is crucial in calculation of sliding power losses (P_S). In this work, the formulation suggested by Xu [10] is utilized for calculation of the friction coefficient, and the friction type is assumed to be fully lubricated in all cases.

The load dependent power losses are mainly divided into sliding losses and rolling losses. The sliding power losses can be derived as:

$$P_S = C_m V_S F_S \quad (1)$$

where C_m is the thermal correction coefficient, V_S is tooth surface sliding speed and F_S is the sliding force.

The Coulomb's law of friction can be used to define the resistive force between two involute spur gear teeth:

$$F_S = \mu W \quad (2)$$

where μ is the friction coefficient, and W is the normal load on the sliding surfaces.

As mentioned earlier, μ is calculated according to Xu's method [10]:

$$\mu = e^f P_h^{b_1} |SR|^{b_2} V_e^{b_3} \nu^{b_4} R^{b_5} \quad (3)$$

where f is a function of the gear tooth's relative speed, P_h is the relative maximum Hertzian pressure, SR is the slide-to-roll ratio around the gear tooth mesh point, V_e is the linear speed of the entering tooth, ν is dynamic viscosity, R is the gear tooth equivalent radii of curvature, and b_i are constant coefficients that can be defined manually according to the lubrication condition or based on running an elastohydrodynamic lubrication (EHL) simulation [10]. Simultaneous rolling and sliding movements take place between the

tooth flanks of two mating gears, except at the pitch point, where pure rolling takes place. As explained in [10], three different regions can be roughly defined on a μ versus SR curve. In this study, in order to simplify the friction coefficient formulation and hasten the simulation process the mesh cycle is discretized into seven points which are critical points and friction coefficient is calculated at those points only. The trend of discretized mesh cycle conforms to continuous models in [10].

As it can be seen in Figure 1, when the sliding velocity is zero, there is no sliding friction, and only rolling friction (though very small) exists. Thus, the value of the friction coefficient should be almost zero at the pitch point. When the slide-to-roll ratio, SR , increases from zero, the friction coefficient, first increases linearly with small values of SR . This region is defined as the linear or isothermal region. When the SR increases further, μ reaches a maximum value and then decreases as the SR value increases beyond that point. This region is referred to as the nonlinear or non-Newtonian region. As SR increases still further, the friction decreases in an almost linear fashion; the thermal region [18].

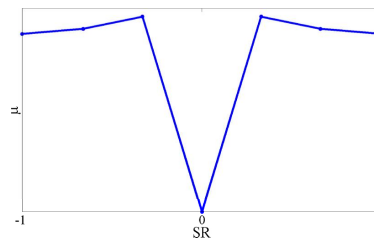


Figure 1. Friction coefficient variation over mesh cycle

Power losses due to rolling can be obtained as follows:

$$P_R = C_m V_R F_R \quad (4)$$

where V_R is gear tooth rolling speed and F_R is the rolling load at the gear tooth [19].

Compression from the pressure of one tooth on another tries to eliminate the oil film between the teeth. Although the lubricant film stretches because of molecular cohesion (viscosity), it also resists, thus behaving like a spring. A portion of this stress is converted to heat and the remainder breaks the molecular bonds of the oil [20]. Consequently, film thickness is the main factor determining the behavior of the lubricant and losses and wear in gear meshing.

In order to derive average power losses during the mesh cycle for both sliding and rolling losses, discretized integration is done in each sequence. As illustrated in Figure 2, the mesh cycle is split into three sequences: before the mesh point, at the mesh point and after the mesh point.

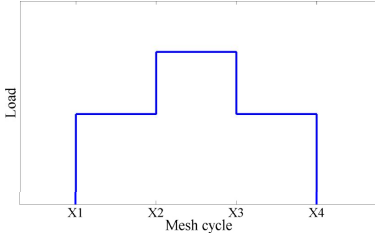


Figure 2. Load sharing on teeth sequences, [9].

Since most sliding and pumping losses occur before and after the mesh point, they are weighted double that of losses at the mesh point:

$$\bar{P}_S + \bar{P}_R = \frac{1}{X_4 - X_1} \left\{ 2 \int_{X_1}^{X_2} [P_S(X) + P_R(X)] dx + \int_{X_2}^{X_3} [P_S(X) + P_R(X)] dx + 2 \int_{X_3}^{X_4} [P_S(X) + P_R(X)] dx \right\} \quad (5)$$

Where P_S and P_R are power losses due to sliding and rolling components, respectively, X_1 is the start of a mesh cycle in which two teeth share the load, X_2 is the start of single-tooth contact, X_3 is the end of single-tooth contact, and X_4 is the end of the mesh cycle. For the discretized gear mesh cycle $X_1 \dots X_4$ in Figure 2, the following equations are calculated between each two collars of X_i where the gear mesh type is constant.

The load independent losses (spin losses) which are categorized as oil churning and windage losses in [16], is calculated based on the formulation in [21].

VEHICLE SIMULATION MODEL

A generic vehicle simulation model for electric power consumption over a given driving cycle is developed that enables comparison of the effect of the driveline configuration on power consumption. The model is composed of electrical component efficiency, drivetrain inertias, gearbox efficiency, regenerative braking, and a shifting scheme that selects the gear ratio according to the vehicle road speed. In the simulation model, different options are defined to form the architecture of the powertrain. The type of transmission (stepped or continuous), number of gears and ratio variation are adjustable, and fixed term and real-time efficiency can be calculated in each stage.

In the modeling of the gear ratios in stepped gearboxes, the characteristics of the chosen gears need to be taken into account in calculation of the load-dependent losses. Furthermore, spin losses should be considered for idling gears based on the architecture of the gearbox. For example, in a six-step gearbox, both load-dependent losses and spin losses in the engaged gear pair are required. By neglecting dog clutches and synchronizer losses for each stage, spin losses can be calculated individually for idling gears.

In a stepped-type gearbox architecture, the gear parameters need to be defined beforehand in the mathematical model in order to form the efficiency maps of each gear pair. The mathematical model for gear efficiency calculation is run over a variety of main parameters i.e. speed and torque, considering the driveline limitations to form the gear efficiency map. By utilizing parameters that do not vary with time, e.g. gear module etc., the simulation model can give instantaneous gear efficiency based on the applied torque and operating speed by interpolating the data from the gear efficiency map.

For continuous transmission types, e.g. variable pulley diameter systems, power losses are higher than with geared transmissions [22]. In modeling of such configurations, there are two options for efficiency calculation; fixed value or equivalent geared model. In the equivalent geared model, by defining the boundary ratios - minimum and maximum ratio required - and equivalent gear-pinion parameters based on the desired accuracy, the ratio range is discretized into very small steps and the gear parameters are interpolated correspondingly.

The required propulsion power to follow the drive cycle for the sample vehicle is calculated as below:

$$P_r = (C_r + \sin \alpha) mgV + \frac{1}{2} \rho C_d AV^3 \quad (6)$$

where C_r is coefficient of rolling resistance, α is road slope, m is vehicle total mass, g is gravity acceleration, V is vehicle linear speed, ρ is air density, C_d is air drag coefficient and A is vehicle frontal area. The efficiency of components then is interpolated from readymade tables and multiplied by passing power through it. At every simulation step the required propulsion power is divided by the total efficiency of the driveline and the cumulative power consumption is calculated accordingly. The diagram of power loss due to studied components is illustrated in Figure 3.

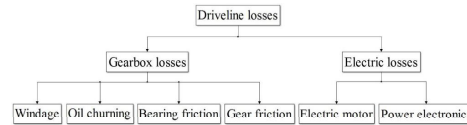


Figure 3. Driveline power loss diagram

As it can be seen in Figure 4, the electrical efficiency is interpolated from the electric machines efficiency map and will be multiplied by vehicle demanded power as well as gearbox efficiency to provide the real value of extracted power from the batteries in real-time manner.

The efficiency calculator gives total efficiency of the powertrain at any arbitrary working point. The power consumption of different transmissions can be evaluated at the end of the driving cycle. The simulation model also enables comparison of the total efficiencies of the drivelines under study, which in this work are a single reduction gear, a five-step gearbox and an IVT.

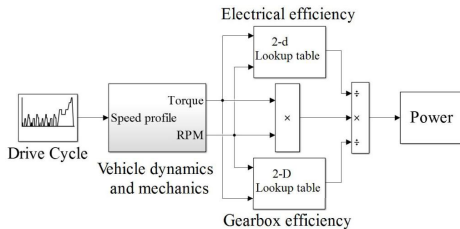


Figure 4. EV simulation model.

MODEL PARAMETERS

The efficiency model is applied to an EV model with manufacturer reported parameters, shown in Table 1. The input driving cycles are the New European Driving Cycle (NEDC) and the EPA Federal Test Procedure (FTP-75) with smooth acceleration and deceleration.

Table 1. Parameters of the EV model.

Air density in	1.225 kg/m ³
Vehicle mass	1337 kg
Vehicle frontal area	2.45 m ²
Air drag coefficient	0.30
Tire rolling resistance coefficient	0.015
Dynamic rolling radius of the tire	0.303 m
The moment of inertia of the bodies	0.206 kgm ²
The moment of inertia of non-driving axle and prior to the reduction gear	1.86 kgm ²
Efficiency of regenerative braking	0.5

In this study, the system is lubricated by oil jet and it is assumed that the gears are not drawn in an oil pool. The single reduction gear pair parameters are shown in Table 2. Furthermore, oil splashing, which causes momentum losses due to oil drop departure, and vibration losses, which make noise, have not been taken into consideration. The windage and bearing losses can be calculated in a straightforward manner by simple mathematical operation. However, the mesh losses are more complex and require more detailed analysis.

Table 2. Single reduction gearbox parameters.

Gear pitch diameter	0.0254 m
Pinion pitch diameter	0.01524 m
Number of teeth of gear	80
Number of teeth of pinion	48
Diametral pitch	0.3175 N/m
Pressure angle	20 deg
Helix angle	20 deg
Tooth width	0.0147 m
Lubricant dynamic viscosity	50 cP
Lubricant kinematic viscosity	60 cSt
Lubricant friction coefficient	0.16
Immersion level	0.5
Bearing thrust factor	0.5
Bearing radial factor	0.6
Bearing bore diameter	0.07 m
Bearing friction coefficient	0.002

A schematic layout of a conventional 5 step gearbox which is applied in driveline modeling is illustrated in Figure 5. As it can be seen from the figure, the input torque is transmitted to the countershaft with a constant gear ratio. Engaging any of gears will multiply the input-countershaft ratio by the corresponding gear ratio and finally by multiplying the differential ratio total gear ratio between the torques produced by engine the one on the wheel will be achieved.

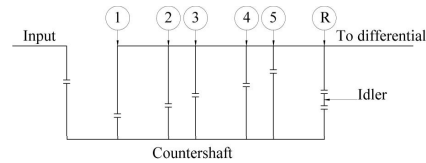


Figure 5. Gearbox schematic.

In conventional variable stepped transmission with a countershaft, there is a pair of gears for each step. Considering the ratio of 1.66:1 for the countershaft and 3.5:1 for the differential, ratios for each gear can be calculated as given in Table 3.

Table 3. Gearbox ratios.

Shifting stage	Pinion diameter [mm]	Gear diameter [mm]	Fixed ratio	Total ratio
1 st	40	80.8	5.81:1	11.73:1
2 nd	50	75		8.72:1
3 rd	65	51.3		4.59:1
4 th	85	49.3		3.37:1
5 th	90	41.4		2.67:1

SIMULATION RESULTS

The presented transmission model was run and archived for gear pairs that are used in the vehicle model over the electric motor operation points, i.e., 0 to 10000 rpm and -350 Nm to +350 Nm. The obtained transmission efficiency data were then embedded into the corresponding vehicle model to derive the efficiency at any arbitrary power point. The simulation model was run for two different driving cycles to validate the compatibility of the model with both NEDC and FTP-75.

The instantaneous energy consumption of an EV with different gearboxes on NEDC was simulated, Figure 6, and the total efficiencies were compared by considering efficiency variation at different time steps. The power required for the driving cycle is given in the electric motor-generator efficiency map for the single reduction gear, five-step gearbox and IVT in Figure 7a, Figure 7b and Figure 7c, respectively.

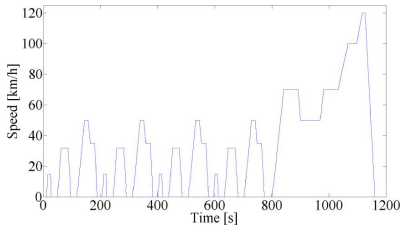
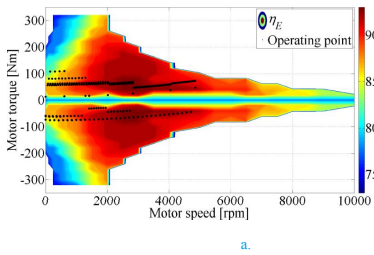
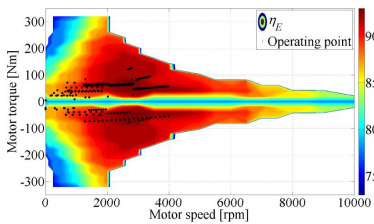


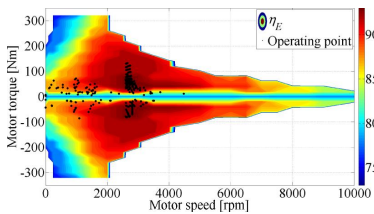
Figure 6. New European Driving Cycle (NEDC).



a.



b.

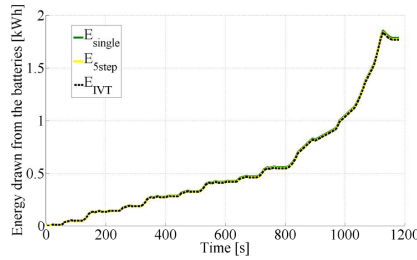


c.

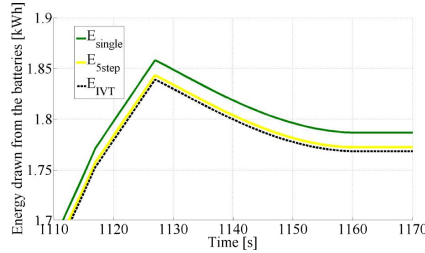
Figure 7. Operating points of Electric motor during NEDC over efficiency map with a) single reduction gear, b) five-step gearbox and c) IVT.

It should be mentioned that the electric motor operation map is plotted in nominal condition whereas the maximum output power is almost double of the nominal power. However there are some operation points (specifically for FTP-75 drive cycle) that are out of the map in Figure 7 and Figure 10, it does not mean that the electric motor is not capable of producing corresponding power. The

correlating efficiency is also calculated by extrapolating the given values from nominal operation range. However the cumulative energy consumption in all three drivetrain architectures seems to be similar in Figure 8, in the magnified scope, minor difference can be seen that shows the single reduction gear design depletes batteries more than the other drivetrain designs.



a.



b.

Figure 8. a) Cumulative energy consumption during NEDC with single reduction gear five-step gearbox and IVT. b) Zoomed scope.

The simulation was also run with FTP-75 as the input driving cycle, Figure 9. Operation points are plotted for the electric motor-generator in Figure 10a, Figure 10b and Figure 10c for the single reduction gear, five-step gearbox and IVT, respectively. The energy consumption seems to be similar in the five-step gearbox and IVT, but the single gear transmission exhibits clear differences, Figure 11.

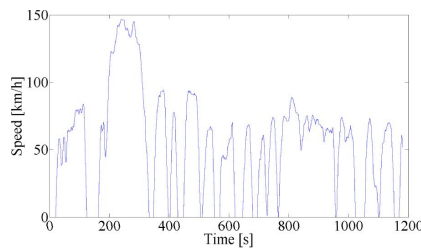


Figure 9. FTP-75 driving cycle.

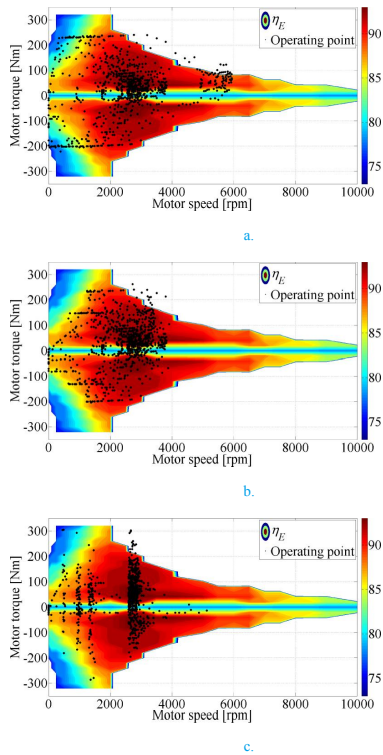


Figure 10. Operating points of Electric motor during FTP-75 over efficiency map with a) single reduction gear, b) five-step gearbox and c) IVT.

Comparing the cumulative power consumption curve as shown in Figure 11, and driving cycle fluctuation in Figure 9, it can be seen that at high speeds the low efficiency of single reduction gear causes higher power consumption.

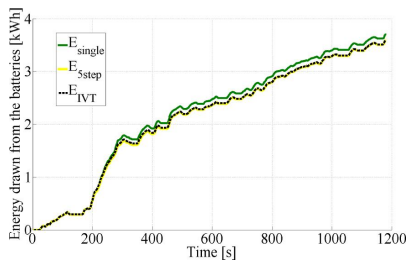


Figure 11. Cumulative energy consumption during FTP-75 with single reduction gear, five-step gearbox and IVT.

As shown in Table 4, the total energy consumption of the driveline according to the last cumulative energy consumption point are brought in comparison. The powertrain with a single gear takes more energy from the batteries than the five-step gearbox for both NEDC and FTP-75.

Table 4. EV energy consumption (kWh/100km).

	NEDC		FTP-75	
	ideal	real	ideal	real
Single gear	133	135	326	333
5-step gearbox	131	139	318	335
IVT	130	144	316	345

The simulation model was run in both an ideal situation, where the efficiency of the non-electrical components was set to 100 percent, and in realistic situations, for which the proposed model was employed to calculate the power losses due to mechanical components, i.e. transmission. The simulation results for ideal transmissions indicated that the trip range of an EV in which an IVT is embedded improves by 2.5% for NEDC and 3% for FTP-75 compared to a single reduction gear. The EV equipped with a 5-step manual transmission has a trip range improved by 1.5% and 3% for NEDC and FTP-57 driving cycle respectively. In order to illustrate the contrast in energy consumption level across different driving cycle and transmission configuration in both ideal and real situation, results in Table 4 are plotted as bar chart in Figure 12.

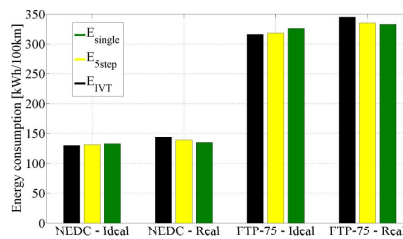


Figure 12. Energy consumption comparison bar chart

However, although the IVT seems to be a better option than a single reduction gear in an ideal situation, in realistic conditions when the gearbox power losses are taken into account, the efficiency of the driveline drops by 6.6% for NEDC and 3.6% for FTP-75. As it can be seen from Table 4, in the real situations, the power consumption increases as the driveline architecture gets more complicated. The reason for the simulation with IVT resulting in higher energy consumption in both NEDC and FTP-75, as can be seen from Table 4, is that the mechanical power losses in IVT are relatively higher and will cancel out the achieved improvement in electrical efficiency. Even though the results vary for different driving cycles and gear ratio selections, this simulation shows that with equivalent settings, extra component power losses outweigh any downstream efficiency gained in the more efficient operation of the electric motor.

CONCLUSIONS

A simulation model for electric vehicle energy consumption is developed and three types of transmissions are embedded in the simulation. The results are compared for total energy consumption of an electric vehicle. Based on the simulation model, which includes gearbox losses, gear ratio selection strategy and efficiency maps of power electronics and the electric motor, the most efficient option for transmission is a single reduction gear. In this study, comparison is done only from the point of view of energy efficiency while the additional costs and complications introduced into the system are neglected. Complementary studies are required to evaluate the feasibility of using IVT transmission from the financial point of view. Furthermore, the total efficiency is the outcome of sampled gearbox efficiency and given efficiency maps of electronic components, thus the results may vary in different combination of driveline components.

REFERENCES

- Nerg, J., Niemela, M., Pyrhonen, J., Partanen, J., 2002. FEM calculation of rotor losses in a medium speed direct torque controlled PM synchronous motor at different load conditions. IEEE Trans. Magn. 38, pp. 3255-3257. doi:10.1109/TMAG.2002.802127
- Sharma, R., Manzie, C., Bessede, M., Brear, M.J., Crawford, R.H., 2012. Conventional, hybrid and electric vehicles for Australian driving conditions - Part 1: Technical and financial analysis. Transp. Res. Part C Emerg. Technol. 25, pp. 238-249. doi:10.1016/j.trc.2012.06.003
- Sharma, R., Manzie, C., Bessede, M., Crawford, R.H., Brear, M.J., 2013. Conventional, hybrid and electric vehicles for Australian driving conditions. Part 2: Life cycle CO₂-e emissions. Transp. Res. Part C Emerg. Technol., Euro Transportation: selected paper from the EWGT Meeting, Padova, September 2009 28, pp. 63-73. doi:10.1016/j.trc.2012.12.011
- Immonen, P., Lindh, P., Niemela, H., Pyrhonen, J., Sinkko, S., Kasurinen, M., 2014. Energy saving by hybridization of a city bus, in: 2014 16th European Conference on Power Electronics and Applications (EPE'14-ECCE Europe). Presented at the 2014 16th European Conference on Power Electronics and Applications (EPE'14-ECCE Europe), pp. 1-8. doi:10.1109/EPE.2014.6910855
- Minav, T.A., Pyrhonen, J.J., Laurila, L.I.E., 2012. Permanent Magnet Synchronous Machine Sizing: Effect on the Energy Efficiency of an Electro-Hydraulic Forklift. IEEE Trans. Ind. Electron. 59, pp. 2466-2474. doi:10.1109/TIE.2011.2148682
- Ren, Q., Crolla, D.A., Morris, A., 2009. Effect of transmission design on Electric Vehicle (EV) performance, in: IEEE Vehicle Power and Propulsion Conference, 2009. VPPC '09. Presented at the IEEE Vehicle Power and Propulsion Conference, 2009. VPPC '09, pp. 1260-1265. doi:10.1109/VPPC.2009.5289707
- Holdstock, T., Sorniotti, A., Everitt, M., Fracchia, M., Bologna, S., Bertolotto, S., 2012. Energy consumption analysis of a novel four-speed dual motor drivetrain for electric vehicles, in: 2012 IEEE Vehicle Power and Propulsion Conference (VPPC). Presented at the 2012 IEEE Vehicle Power and Propulsion Conference (VPPC), pp. 295-300. doi:10.1109/VPPC.2012.6422721
- Hofman, T., Dai, C.H., 2010. Energy efficiency analysis and comparison of transmission technologies for an electric vehicle, in: 2010 IEEE Vehicle Power and Propulsion Conference (VPPC). Presented at the 2010 IEEE Vehicle Power and Propulsion Conference (VPPC), pp. 1-6. doi:10.1109/VPPC.2010.5729082
- Anderson, N.E., Loewenthal, S.H., 1980. Spur-gear-system efficiency at part and full load. National Aeronautics and Space Administration, Scientific and technical Information Office.
- Xu, H., Anderson, N., Maddock, D., Kahraman, A., 2007. Prediction of mechanical efficiency of parallel-axis gear pairs. J. Mech. Des. 129, pp. 58-68.
- Haddoun, A., Benbouzid, M.E.H., Diallo, D., Abdessemed, R., Ghouili, J., Srairi, K., 2007. A Loss-Minimization DTC Scheme for EV Induction Motors. IEEE Trans. Veh. Technol. 56, pp. 81-88. doi:10.1109/TVT.2006.889562
- Gerami Tehrani, M., Kelkka, J., Sopenen, J., Mikkola, A., Kerkkanen, K., 2014. Transmission configuration effect on total efficiency of Electric Vehicle powertrain, in: 2014 16th European Conference on Power Electronics and Applications (EPE'14-ECCE Europe). Presented at the 2014 16th European Conference on Power Electronics and Applications (EPE'14-ECCE Europe), pp. 1-9. doi:10.1109/EPE.2014.6910780
- Emadi, A., Lee, Y.-J., Rajashekar, K., 2008. Power Electronics and Motor Drives in Electric, Hybrid Electric, and Plug-In Hybrid Electric Vehicles. IEEE Trans. Ind. Electron. 55, pp. 2237-2245. doi:10.1109/TIE.2008.922768
- Chan, C.C., Chau, K.T., 1997. An overview of power electronics in electric vehicles. IEEE Trans. Ind. Electron. 44, pp. 3-13. doi:10.1109/41.557493
- Anderson, N.E., Loewenthal, S.H., 1982. Design of Spur Gears for Improved Efficiency. J. Mech. Des. 104, pp. 767-774. doi:10.1115/1.3256434
- Seetharaman, S., Kahraman, A., 2009. Load-Independent Spin Power Losses of a Spur Gear Pair: Model Formulation. J. Tribol. 131, 022201-022201. doi:10.1115/1.3085943
- He, S., Cho, S., Singh, R., 2008. Prediction of dynamic friction forces in spur gears using alternate sliding friction formulations. J. Sound Vib. 309, pp. 843-851. doi:10.1016/j.jsv.2007.06.077
- Michlin, Y., Myunster, V., 2002. Determination of power losses in gear transmissions with rolling and sliding friction incorporated. Mech. Mach. Theory 37, pp. 167-174. doi:10.1016/S0094-114X(01)00070-2
- Anderson, N.E., Loewenthal, S.H., 1983. Comparison of Spur Gear Efficiency Prediction Methods, Defense Technical Information Center, USA
- Mang, T., Dresel, W., 2007. , in: Lubricants and Lubrication. John Wiley & Sons, pp. 749-758.
- Gerami Tehrani, M., 2013. Energy Efficiency Consideration in Electric Vehicle Transmission, Master's thesis. ed. Lappeenranta University of Technology, Finland.
- Genta, G., Morello, L., Cavallino, F., Filtri, L., 2014. Transmission, in: The Motor Car, Mechanical Engineering Series. Springer Netherlands, pp. 439-483.

CONTACT INFORMATION

Mohammad Gerami Tehrani
 Laboratory of Machine Dynamics Lappeenranta University of Technology
 Skinnarilankatu 34 P.O.Box 20 FI-53850 Lappeenranta, FINLAND
 Mobile: +358503006697
Mohammad.gerami.tehrani@lut.fi

ACKNOWLEDGMENTS

The authors would like to acknowledge the Product Development Department of Valmet Automotive Inc. for sponsorship of this research.

ABBREVIATIONS

A - vehicle frontal area
 C - coefficient
 C_d - Air drag coefficient
 C_r - Rolling resistance coefficient
 C_{th} - Thermal correction coefficient
 CVT - Continuously Variable Transmission
 DTC - Direct Torque Control
 EHL - Elastohydrodynamic lubrication
 EV - Electric Vehicle
 F - Force

F_s - Sliding force	V_e - Linear speed of the entering tooth
F_R - Rolling force	V_s - Tooth surface sliding speed
I - Electric current	X - Mesh cycle
ICE - Internal Combustion Engine	b_i - Constant number
IVT - Infinitely Variable Transmission	f - Function of the gear tooth's relative speed
P_n - Relative maximum Hertzian pressure	g - Gravity acceleration
P_R - Rolling power loss	m - Mass
P_S - Sliding power loss	α - Road slope
PMSM - Permanent Magnet Synchronous Motor	μ - Friction coefficient
R - Gear tooth equivalent radii of curvature	ν - Dynamic viscosity
SR - Slide-to-roll ratio	ρ - Air density
U - Electric voltage	τ - Torque
V - Linear speed	ω - Angular velocity

Publication V

Lindh, P., Gerami Tehrani, M., et al.

**Multidisciplinary Design of a Permanent-Magnet Traction Motor for a Hybrid
Bus Taking the Load Cycle into Account**

Reprinted with permission from
IEEE Transactions on Industrial Electronics,
Vol. 63, no. 6. pp. 3397-3408,
© 2016, IEEE.

Multidisciplinary Design of a Permanent Magnet Traction Motor for a Hybrid Bus Taking into Account the Load Cycle

P. M. Lindh, *Member, IEEE*, M. Gerami Tehrani, T. Lindh, J.-H. Montonen, J. J. Pyrhönen, *Member, IEEE*, J. T. Sopenan, *Member, IEEE*, M. Niemelä, Y. Alexandrova, P. Immonen, L. Aarniovuori, *Member, IEEE*, and M.V. Polikarpova

Abstract— An electrical and mechanical design process for a traction motor in a hybrid bus application is studied. Usually, the design process of an electric machine calls for close cooperation between various engineering disciplines. Compromises may be required to satisfy the boundary conditions of electrical, thermal, and mechanical performances. From the mechanical point of view, the stress values and the safety factors should be at a reasonable level and the construction lifetime predicted by a fatigue analysis. In a vehicle application, the motor has to be capable of generating high torque when accelerating, and in normal operation, the losses of the machine should be low to be able to cool the machine. Minimization of the no-load iron losses becomes a very important electrical design requirement if the traction motor and the generator are mechanically connected with an internal combustion engine when it is operating as the only source of torque. The manufacturing costs of the motor are also taken into account in the paper.

Index Terms—Electromagnetic, fatigue analysis, hybridization, mechanical design, permanent magnet motor, thermal design, traction.

NOMENCLATURE

b	Basquin exponent, Fatigue strength exponent
C_d	Drag coefficient
F_c	Centrifugal force
Q	Number of slots per pole and phase
i_{diff}	Final drive gear ratio
K	Rolling friction coefficient
k_t	Stress concentration factor
k_{Fe}	Stator lamination space factor
L_d	Direct-axis synchronous inductance
L_q	Quadrature-axis synchronous inductance
M	Mass
m_{PM}	Magnet mass
m_{rb}	Rotor bridge mass

N	Rotational speed
n_i	Number of repetitions in class i
N	Number of repetitions in all classes
N_f	Number of equivalent load cycles
N_s	Number of stator coil turns in series per phase
p	Number of pole pairs
p_1	Polynomial coefficient 1
p_2	Polynomial coefficient 2
Q	Slots per pole and phase
R	Radius
r_{PM}	Distance of the magnet centers of mass from the rotation axis
r_{mb}	Distance of the rotor bridge centers of mass from the rotation axis
S	Tension bar cross-sectional area
T	Torque
$z_Q/2$	Effective coil turns in half-slot
$\Delta\sigma_{eq}$	Equivalent stress cycle
γ	S-N curve slope
σ	Stress
σ_{tan}	Rotor tangential stress
σ_f	Fatigue strength coefficient
Φ	Magnetic flux
Ω	Mechanical angular velocity

I. INTRODUCTION

THIS study deals with a permanent magnet traction motor design process in which not only the application sets some design limitations but also the manufacturing process and reliability have their impacts on the design. In traction applications, one important design parameter is cooling; usually, mobile machines have some indirect [1, 2] or even direct [3–5] liquid cooling available, which determines the thermal range of the machine and, thereby, also some electrical design parameters such as the maximum current density.

Permanent magnet synchronous motors (PMSMs) and permanent-magnet-assisted synchronous motors (PMASMs) [6–8] have been studied with electric vehicle traction drive applications [9–11] and with different drive cycles [12–14]. Permanent magnet synchronous motors are often used in traction applications, because they provide flexibility with respect to certain important machine design parameters [15–17]. PMSMs with rotor-embedded magnets have favorable characteristics for traction motor applications [18, 19]. Their typical properties include high torque and power densities, a

Manuscript received May 29, 2015; revised August 31, 2015 and November 1, 2015; accepted November 29, 2015.

Copyright (c) 2016 IEEE. Personal use of this material is permitted. However, permission to use this material for any other purposes must be obtained from the IEEE by sending a request to pubs-permissions@ieee.org.

P. M. Lindh, T. Lindh, J.-H. Montonen, J. J. Pyrhönen, M. Niemelä, Y. Alexandrova, P. Immonen, and L. Aarniovuori are with Lappeenranta University of Technology, LUT School of Energy Systems, Electrical engineering, P.O. Box 53851, Lappeenranta, Finland. pia.lindh@lut.fi. M. Polikarpova is a student at LUT Business School.

M. Gerami Tehrani and J. T. Sopenan are with Lappeenranta University of Technology, LUT School of Energy Systems, Mechanical Engineering, P.O. Box 53851, Lappeenranta, Finland. Mohammad.gerami.tehrani@lut.fi.

high torque capability at low speeds, a wide operating speed range, high efficiencies over the speed range, high reliability, and acceptable cost [20, 21]. Embedded magnets are preferred to rotor surface magnets, because they generate less losses than rotor surface magnets, their risk of demagnetization during a stator short-circuit failure is lower, the magnets can be rectangular, and they can be fixed and bonded more reliably in the rotor [21–23]. However, a significant proportion of the PM flux is lost through magnet-retaining parts when embedding the magnets in a ferromagnetic material.

The study introduces a design process where a traction motor having a maximum speed of 4500 min^{-1} and a rated power of 150 kW is designed considering the thermal, electrical, and mechanical performances of the PM machine. The machine has a laminated rotor, in which the permanent magnets are embedded in lamination pockets. The study seeks solutions to the permanent magnet housing pocket in the rotor, with a special focus on the height of the steel bridge covering the pocket and the shape of the hollow space, which are essential both from the mechanical and electromagnetic aspects. The motor design optimization process takes into account the magnet shape, the magnet embedding depth, and the leakage-flux-minimizing air pocket (cavity) areas on magnet sides. The mechanical stresses and the electromagnetic forces are calculated by Finite Element Analyses (FEA). The effects of the embedding depth of the magnets on torque, efficiency, demagnetization risk, and mechanical stresses are reported. The results provide guidelines on the permanent magnet traction motor (PMTM) design.

The electrical and mechanical analyses are performed hand in hand, and three different feasible rotor designs are presented in the paper. The most important mechanical aspects considered in the study are the fatigue life of the rotor laminations under actual duty cycles and the maximum stresses at the highest operation speed. These have to be at an acceptable level without sacrificing the useful magnetic flux. However, it should be noted that both the fatigue life and the maximum stress level are significantly affected by the geometric stress concentrations in the rotor laminations. Both of these issues can be significantly influenced by a proper design. The electromechanically important aspects considered are the maximum available torque, the amount of losses, and tolerance for failure situations. From an economic point of view, the price of permanent magnets is naturally important, and thus, the minimum magnet weight is preferred. From the mechanical point of view, again, light weight often means less supporting structures, and therefore, special attention has to be paid to ensure the mechanical durability of the construction [24]. In the design process, these aspects were weighted and the final rotor design was chosen.

Not only the dimensioning of the combustion engine but also the fuel economy of the engine itself could be optimized for instance by improvements in the engine control. This was shown in [25], where a variable engine valve control was applied to enhance the fuel economy and increase the torque performance over a wider range.

II. APPLICATION

A hybrid bus was designed and constructed at Lappeenranta University of Technology. The active components of the driveline are illustrated in Fig. 1. The combustion engine, a 2.5-liter diesel engine, rotates a generator, a 55-kW outer rotor PM generator. The traction motor is connected with a cardan shaft running the differential and drive shafts. In the series hybrid or electric vehicle mode, a mechanical coupling between the generator and the traction motor is open. In the parallel hybrid mode, the clutch is closed so that all the active components are running with same rotational speed and can relay torque to the wheels. The parallel mode is available when the speed of the bus exceeds 20 km/h (970 min^{-1}). In the parallel mode, the generator and the traction motor are either at load or at no-load. A more detailed description of the mechanical driveline, which enables multiple driving modes, can be found in [26, 27].

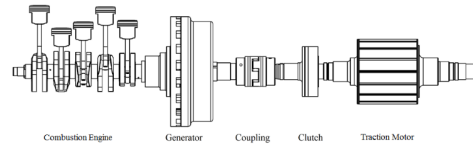


Fig. 1. Driveline: a combustion engine, a 55-kW outer rotor PM generator, coupling, a clutch, and a 150 kW PM traction motor.

In a hybrid bus traction motor, the torque requirements vary in different speed areas. The highest torque demand, suitable supply voltages from the inverter in use, and the demand for maximum speed are the main initial design parameters. The hybrid bus values are given in Table I. The friction forces and the bus speed were computed from these values.

TABLE I
CITY BUS PARAMETERS

Parameter	Symbol	Value
Total mass of bus	M	16 000 kg
Front cross-sectional area	S_f	8 m^2
Air drag coefficient	C_d	0.5
Rolling friction coefficient	K	0.006
Radius of wheel	R	0.478 m
Final drive fixed gear ratio	i_{diff}	8.83

The speed and torque requirements were also investigated for this hybrid bus application by recording an actual drive cycle of a bus route in Lappeenranta [28]. Fig. 2 illustrates the data recorded on the speed profile of the bus route 1 in Lappeenranta and the height profile of the 47 km route. From the cycle it was calculated that the torque demand is approximately 640 Nm at the rated speed of 2240 min^{-1} .

The maximum traction torque needed was estimated to be 1600 Nm while the maximum speed at 80 km/h was calculated to be 3920 min^{-1} . The maximum speed of the diesel engine, 4500 min^{-1} , is selected as the highest possible speed for the mechanical stress analysis. At this speed, the bus should reach a speed of 92 km/h if the mechanical coupling is enabled. Typically, the maximum operating speed is about 60 km/h, and at the rated traction motor speed, the city bus runs at a 45 km/h speed.

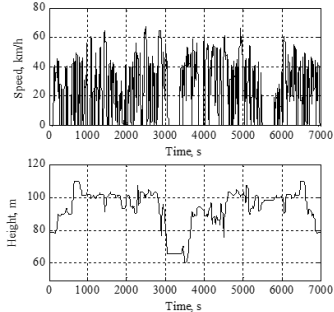


Fig. 2. Speed and height profiles of the bus route 1 [28].

The main initial design parameters such as the highest torque demand, suitable supply voltages from the inverter in use, and the demand for the maximum speed are listed in Table II.

TABLE II
OPERATING SPECIFICATION

Parameter	Value
Rated speed, rpm	2240
Maximum speed, rpm	4500
Rated line-to-line voltage, V	440
Rated mechanical power, kW	150
Rated torque, Nm	639
Maximum torque, p.u.	2.5
Stator outer diameter, mm	396
Rotor outer diameter, mm	260
Machine length, mm	225

The two winding systems of the traction motor are driven by two liquid-cooled inverters with a rated current of 240 A each. The rated voltage of the battery unit (designed at LUT) is 624 V. The battery is directly connected with two parallel inverters feeding the separate windings of the motor. One inverter works as a master and one as a follower. A fast drive-to-drive link relays data such as a rotor angle resolver feedback between the master and the follower. The controls of the inverters are otherwise independent. The dimensioning of the motor, and especially of the inverters, is far from conservative. The inverters operating at their rated current produce approximately 2.5 times the rated torque of the traction motor. This equals to the traction motor maximum torque. Therefore, the bus should be able to operate the route of Fig. 2. This applies if two conditions are satisfied. Firstly, the cooling of the motor and the inverters must be adequately dimensioned with a torque profile during the load cycle, which is calculated using the route data. Here, the dimensioning has been made rather as in conjunction with servo drives than with industrial drives. In addition, the maximum allowed power during operation is limited by using measurements of the coolant temperature and by estimation of the junction temperature of the power switches. Secondly, the problem with a gearless vehicle is that if there is an obstacle as a ramp in front of the wheel or the tire is in a sharp pit, the torque may not be adequate when starting from a standstill. In commercial applications with unknown load data, more conservative

dimensioning would be preferable. On the other hand, the fault tolerance of the traction drive is high when the fault in one inverter does not prevent driving. The maximum torque of the drive with only one inverter is still slightly higher than the rated traction motor torque. Therefore, the bus can operate the route with reduced speed. In addition, the torque references of the inverters can vary with healthy inverters also. This option can be used to optimize the efficiency of the drive or to balance the temperatures of individual inverters in order to maximize the temperature margin of the whole drive.

III. ELECTROMAGNETIC ANALYSIS

The authors produced and analyzed several magnet volumes and their air-pocket styles, tested the embedding depth of the magnets, investigated ways to increase the inductance ratio, and analyzed the mechanical stresses of the rotor. The value of the armature reaction flux Φ depends greatly on the effective air-gap length, which is not easy to obtain accurately by analytical equations when the magnets are embedded and the rotor is nonuniform having air pockets. Therefore, the finite element method was applied to solve Φ . The motor inductances are the most critical parameters when calculating the maximum torque achieved from the motor, because the torque is inversely proportional to the inductance. The inductances presented in this study are computed from the flux values obtained by the finite element method and then divided by the current values as shown previously in [26]. From the machines studied, three of the most promising designs were chosen for further analysis. The geometry and flux lines at no-load of each three rotors are depicted in Fig. 3.

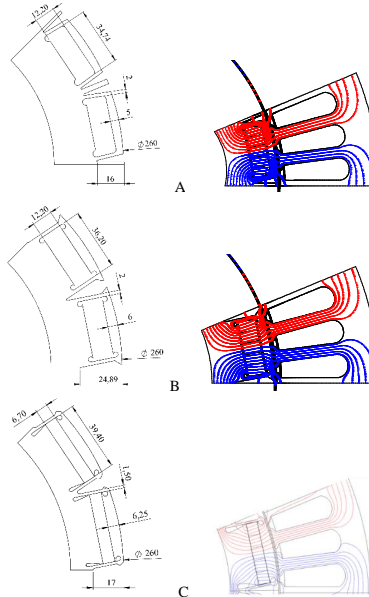


Fig. 3. Rotor geometry structures A, B, and C. Note: the manufacturing tolerances are ± 0.1 mm around the magnets.

As shown in Fig. 3, each permanent magnet is segmented into five pieces in order to reduce eddy current losses. The first design A is a toothed rotor, whose q-axis teeth protrude 1 mm from the rotor outer surface. This arrangement increases the q-axis inductance and provides some extra reluctance torque for the machine. The magnet-retaining bridge was one of the optimizing targets. The final agreement was a 5 mm thickness at the bridge midpoint and 2 mm thickness at the lateral walls. The second proposed design B with wedge-shaped slots brings the magnets 1 mm deeper than the first design, but larger magnets are embedded in the rotor. The lateral wall thickness is 2 mm, and the outer diameter is the same. The third analyzed design C is a modified version of the second design with the same outer diameter but deeper embedded magnets, thinner lateral walls, and smaller magnets. This magnet housing offers a good path for the main magnetic flux, and at the same time, suitable mechanics that minimize the stresses. The air pockets are more complicated, and lower grooves are stretched towards the rotation axis to minimize the magnet leakage.

The dynamic FEA computations applying the Cedrat 2D program were performed for machine designs A, B, and C. First, a dynamic computation with no load was performed to determine the amount of induced voltage and the waveforms presented in Fig. 4.

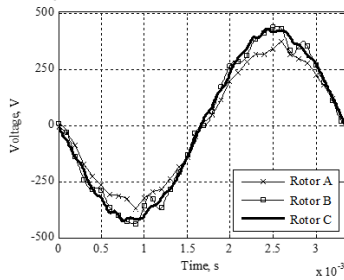


Fig. 4. No-load voltage waveforms of rotors A, B, and C.

The d- and q-axis inductance components were given as a function of current in order to compute the torque over the speed range. First, a static finite element computation was run to determine where the flux density has its maximum and where it is zero. These angular positions were used to solve the d- and q-axis inductances, given at the rated current in Table III. Short-circuit computations were also performed to ensure the d-axis inductance values. Next, dynamic FE computations were run using sinusoidal voltage supplies. According to the voltage-driven dynamic FEA, all studied machines yielded the required 1600 Nm torque (line-to-line voltage at 440 V). The analysis results from the FE computations are collected in Table III. There are two separate parallel windings in the whole machine, each supplied with an inverter of its own; in Table III, however, only the total inductances of the motor are given. The eddy current losses in the permanent magnets of these machines are not compared as they are not significant; the eddy current losses in the permanent magnets are less than 10 W. This is because the

magnets are segmented into five pieces, the magnets are deep inside the rotor, and an integer winding is used.

TABLE III
MACHINE PARAMETERS

Rotor	A	B	C
Induced voltage (no-load), V	245	293	297
Maximum torque, p.u. at low speeds	2.5	2.5	2.6
Iron losses at the rated load, kW	1.2	1.6	1.6
Joule losses at the rated load, kW	1.45	1.1	1.25
Efficiency at the rated point	0.964	0.964	0.963
Direct-axis inductance L_d , mH	0.76	0.66	0.7
Direct-axis inductance L_d , per unit	1.1	0.96	1.06
Quadrature-axis inductance L_q , mH	1.08	1.06	1.06
Quadrature-axis inductance L_q , per unit	1.62	1.5	1.61
Magnet height, mm	12	12	6.5
Magnet width, mm	33	36	39.15
Magnet mass, kg	11	11.8	7
Magnet price, €	1900	2100	1200
Total active material price, € (Al, Fe, Cu, Neodym magnets)	2800	3000	2100

The same differences were detected in the loss values: rotor structure A has the smallest iron losses but the largest copper losses among the studied machines. Nevertheless, the total losses at the rated point are approx. the same between the rotor designs. The efficiencies at several speeds and loads were computed and gathered to produce an efficiency map of each rotor design. A dynamic model of the whole drive system (generator, diesel set) was built in a Matlab Simulink environment to estimate the overall fuel consumption and energy efficiency. Based on simulations, the drive system overall efficiency was approximately 0.92 in all cases. In this system, the efficiency was not affected by the rotor design.

The material consumption and material prices of the motors are given in Table III. The material prices for the machine manufactured in 2014 were: neodymium magnets 175 €/kg, aluminum 2 €/kg, steel 3 €/kg, and copper 7 €/kg. The neodymium magnet price at the moment is approx. 100 \$/kg, resulting in a lower material price of the machine. It can also be seen that the total material prices of motors B and C differ by 900 euros.

The reliability of the traction motor applied to a hybrid bus is an important issue. Therefore, the magnet material N38UH was chosen because the maximum operation temperature of this material is 160°C. In addition, the risk of irreversible demagnetization during fault operation was studied in detail for each rotor. According to the manufacturer's B/H curves, the first possible irreversible demagnetization temperature is 150°C. At this temperature, the irreversible demagnetization point (knee) is approx. at 0.36 T. This temperature was also studied with other traction drives [11], although the motor should not reach such a temperature in normal operation.

The demagnetization risk was first analyzed in rated load and overload situations. The irreversible demagnetization was performed according to [29]. As a result, none of the rotor designs suffered from demagnetization during the rated load or overload. In the short-circuit failure case, a finite element dynamic computation was performed at the most critical moment, which is estimated to be at the time instant when the

induced voltage decreases close to zero. Next, a three-phase short-circuit was simulated where the short-circuit currents reached values of 1.5 p.u. The flux density was analyzed from a 0.1 mm depth from the magnet surface; the flux density normal components are depicted in Fig. 5. Rotor A is well protected against irreversible demagnetization because of the shaping of the air pockets. It can also be seen from the flux density behavior that designs B and C may have irreversible demagnetization in the magnet corners in the case of a three-phase short-circuit if the magnet temperature is 150°C or above.

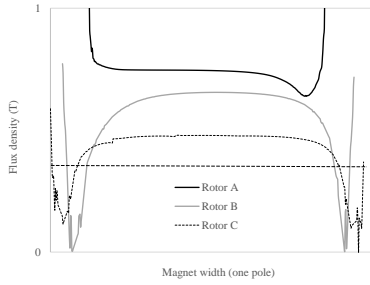


Fig. 5. Normal component of the flux density at 150°C during a three-phase short-circuit from the FEA. The critical demagnetization limit for the magnet material is 0.36 T (dashed line).

IV. MECHANICAL ANALYSIS

The proposed concepts were modeled with plane stress boundary conditions. The fatigue life was analyzed under stresses caused by the centrifugal force by the given drive cycle. A formulation for the distributed load on a beam was applied to calculate the effective stresses on the model. A similar phenomenon also occurs in slitted solid rotors, as it was shown in [24].

In the analysis, the effect of adhesives (i.e., glue or resin) between the magnet and the rotor is neglected. In other words, it is assumed that the magnets are retained in their pockets only by the mechanical structure of the rotor. As a result of this assumption, the external load resulting from the magnet mass at the maximum speed is applied to the ceiling of the magnet housing. By considering the mass of the magnet pocket iron bridge, the total force carried by the tension bars on the permanent magnet sides can be calculated as

$$F_c = (m_{PM}r_{PM} + m_{rb}r_{rb})\omega^2 \quad (1)$$

where m_{PM} and m_{rb} are the magnet and rotor bridge masses and r_{PM} and r_{rb} are the distances of the magnet and the rotor bridge centers of mass from the rotation axis, respectively. The nominal stress caused by the centrifugal force, F_c , can be calculated as

$$\sigma = k_t \frac{F_c}{S} \quad (2)$$

where S is the tension bar cross-sectional area and k_t is the stress concentration factor. In the case of simple geometries,

the stress concentration factors can be obtained from mechanical engineering charts. In a general case of complicated geometry, the stress concentration factors can be calculated applying the finite element method. The latter approach is adopted in this study to calculate k_t .

The centrifugal force and the stresses caused by it vary in relation to the square of the angular velocity. As a result, the relationship between the electric motor speed profile and the resulting stress profile can be obtained. In the study, also the stress levels caused by the combination of the tangential and centrifugal forces at different speeds were calculated. It was observed that the stresses caused by the tangential forces are negligible compared with those caused by the centrifugal forces at high speeds. Similar findings were also reported by Gao *et al.* [31]. Therefore, in the fatigue life calculation presented in this study, only stresses caused by centrifugal forces are taken into account, because they are dominant.

A. Centrifugal stresses at different rotational speeds

The initial design, rotor A in Fig. 3, is a toothed rotor in which the teeth protrude 1 mm from the rotor outer diameter. Several magnet housing geometries were analyzed to reduce the stress concentrations in the corners, and simultaneously, meet the electromagnetic requirements of the traction motor rotor. The centrifugal force on the magnet mass at 4500 rpm is 75 N. The second proposed design, rotor B with wedge-shaped slots, brings magnets 1 mm deeper than in the first design but the magnets also have to be larger. The centrifugal force of the magnets at 4500 rpm is 86 N. The third analyzed design rotor C has thin lateral walls and a small magnet volume. The glue injection holes are more complicated, and lower grooves are stretched towards the rotation axis. The centrifugal force of the magnets at 4500 rpm is 52 N.

In order to find a relation between the stress level and the rotational speed, the maximum stress at different speeds is determined, and next, an average of the speed–stress ratio is calculated (Table IV). All the maximum stresses are calculated in the worst-case scenario in which it is assumed that the adhesive chemical used does not retain the magnets in their positions. In this case, the centrifugal force caused by the magnets will be carried by the magnet housing bridge, and the bridge is retained by radial spokes. This condition is modeled by applying a radially distributed load to the lower surface of the bridge. A more detailed finite element study of the proposed electric motor is presented in [29].

TABLE IV
MAXIMUM STRESS OF THE MAGNET-RETAINING BARS AT DIFFERENT
ROTATIONAL SPEEDS IN ISOTHERMAL CONDITION [Pa]

RPM	Rotor A	Rotor B	Rotor C
500	2.6	3.5	2.3
1000	11	14	9
1500	24	32	21
2000	42	57	38
2500	66	89	59
3000	95	128	84
3500	130	175	115
4000	167	228	150
4500	216	289	195

A further stress analysis, which accounts for the temperature difference in the steady-state situation, is also performed. In the first case, an exaggerated condition is assumed in which the outer surface of the rotor is at 140°C, the magnet pocket top is at 120°C, the magnet pocket bottom is at 100°C, and the rotor core is at -10°C. Despite the fact that such a condition is impossible in practice, the maximum stress at different operating speeds is calculated, and even though it is close to the yield stress at some points, the safety factor is still above one. In the second case, a more realistic thermal condition is assumed. Based on the studies conducted for the cooling system design in section VI of this paper, the realistic thermal condition at the rated speed is adopted. In this case, the maximum recorded temperature in the rotor is 80°C, which is at the outer surface, as can be seen Fig 13. Then, an FE analysis is made in which both the thermal loads and the mechanical loads are considered simultaneously to calculate the maximum stress. The results are shown in Table V.

TABLE V
MAXIMUM STRESS OF THE MAGNET-RETAINING BARS AT DIFFERENT
ROTATIONAL SPEEDS WITH TEMPERATURE GRADIENT [Pa]

RPM	Rotor A	Rotor B	Rotor C
500	26	61	30
1000	23	50	21
1500	27	32	25
2000	46	34	42
2500	70	54	64
3000	99	78	90
3500	133	117	126
4000	173	172	175
4500	218	235	229

As it can be seen, the stress level trend according to the speed inclination is different in the isothermal condition and when different temperatures are applied to different surfaces. It can be noticed that at some points, the counter displacement resulting from thermal deformation and the mechanical loads cancel out each other and remain below the stress level. However, the nonuniform heat affects the mechanical behavior of the rotor, but it does not raise the stress over the yield stress point, and can be neglected in this study. Furthermore, the transient computational fluid dynamics (CFD) analysis of the heat flux through the motor components calls for a separate study, which is out of the scope of this paper.

By analyzing data in Table IV, the relation between the stress level and the rotational speed can be determined. A first-degree polynomial curve fitting with respect to the square of the rotational speed and the maximum stress at the corresponding rotational speed is conducted as follows

$$\sigma = p_1 n^2 + p_2 \quad (3)$$

where n is the rotational speed in min^{-1} and p_i are the polynomial coefficients. It can be seen that there is almost a linear correlation between the maximum stress and the square of the rotation speed, as the coefficients of determination (R-square) are higher than 0.99 for all three designs. The fitted values for polynomial coefficients are shown in Table VI.

TABLE VI
FITTED FIRST-DEGREE POLYNOMIAL COEFFICIENTS

	Rotor A	Rotor B	Rotor C
p_1	$1.059 \cdot 10^{-5}$	$1.427 \cdot 10^{-5}$	$9.528 \cdot 10^{-6}$
p_2	$-5.897 \cdot 10^{-2}$	$-1.368 \cdot 10^{-1}$	$-5.564 \cdot 10^{-1}$

B. Fatigue study

In order to calculate the fatigue life of the rotor, the results from Table IV are considered. As it can be seen in Fig. 1, the recorded drive cycle is nonuniform, thus resulting in a fairly complex stress history during the cycle. In these kinds of cases, a rainflow cycle counting method can be used together with the Palmgren-Miner linear damage hypothesis to assess the fatigue life of the structure. By the rainflow analysis, the equivalent stress cycle, $\Delta\sigma_{\text{eq}}$, can be evaluated as follows [30]

$$\Delta\sigma_{\text{eq}} = \sqrt{\frac{\sum_i^k n_i \Delta\sigma^{\gamma}}{N}} \quad (4)$$

where k is the quantity of the rainflow stress classes, n_i is the number of repetitions in class i , $\Delta\sigma$ is the stress variation in that class, and N is the total number of repetitions in all classes. The exponent γ is the S-N curve slope, and for the machine cut edges, m is equal to 3 [31].

The number of equivalent load cycles N_f that the structure tolerates until a fatigue damage is developed can be solved from the Basquin equation [32]

$$\frac{\Delta\sigma_{\text{eq}}}{2} = \sigma'_f (2N_f)^b \quad (5)$$

where σ'_f is the fatigue strength coefficient and b is the Basquin exponent or fatigue strength exponent. Based on the published fatigue test results for similar rotor laminate materials [31], the following fatigue parameter values are adopted in this study: $\sigma'_f = 673.25$ MPa and $b = -0.09559$. The calculated equivalent stress cycles $\Delta\sigma_{\text{eq}}$ and the number of cycles N_f for designs A, B, and C over the driving cycle depicted in Fig.1 are given in Table VII.

TABLE VII
FATIGUE LIFE RESULTS FOR LAPPEENRANTA DRIVING CYCLE

	Rotor "A"	Rotor "B"	Rotor "C"
$\Delta\sigma_{\text{eq}}$ (MPa)	293	440	252
N_f (cycles)	$4 \cdot 10^6$	$6 \cdot 10^6$	$20 \cdot 10^6$
Drivability (km)	$5.3 \cdot 10^{12}$	$5.4 \cdot 10^{10}$	$6.4 \cdot 10^{13}$

To validate the design fatigue life for a standard drive cycle rather than the recorded drive cycle on the local track, a fatigue study is conducted also for the New European Driving Cycle (NEDC) shown in Fig. 6. However, because the maximum speed of the bus is 92 km/h, the low-powered vehicle cycle is applied for the Extra-Urban Driving Cycle [33]. Fig. 6 shows the NEDC speed profiles; it can be seen that the maximum speed is higher than in Lappeenranta bus route 1.

The fatigue analysis results for the NEDC drive cycle are shown in Table VIII. It is pointed out that the number of

cycles and drivability values are equal as the NEDC_{LF} length is 994 m, which is very close to one kilometer.

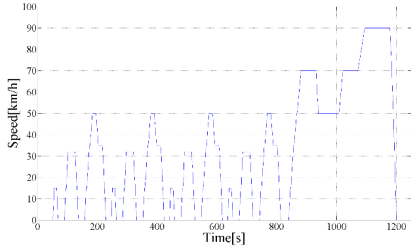


Fig.6. NEDC speed profile for the low-powered vehicle cycle

TABLE VIII
FATIGUE ANALYSIS RESULTS FOR NEDC_{LF}

	Rotor A	Rotor B	Rotor C
$\Delta\sigma_{eq}$ (MPa)	224	304	194
N_f (cycle)	$71 \cdot 10^6$	$2.8 \cdot 10^6$	$3 \cdot 10^6$
Drivability (km)	$7.1 \cdot 10^7$	$2.8 \cdot 10^6$	$3.1 \cdot 10^8$

V. ANALYSES

From the electromagnetic and mechanical computations, some values were gathered in Table IX to compare the three rotor designs. Important issues are the maximum available torque, the efficiency at the rated point, and the magnet price. The other manufacturing costs were almost the same for all rotors as the most expensive item was the neodymium magnets; their price at the time of the manufacturing in 2014 being 175 €/kg. From the mechanical point of view, the key issues are the stresses caused by the centrifugal force and torque loads and the fatigue life length.

All of the designs are capable of carrying the required loads without reaching the yield area. The final conclusion, from the mechanical point of view, depends on how frequently the traction motor will reach 4500 rpm. According to Table IX, if safety factor is considered as the only criterion for evaluation, the design “C” would be the foremost option. Taking into account the results of Table VII and Table VIII, design “C” is preferential not only because of the higher safety factor, but also longer fatigue life.

However, for multi-criteria optimization, a selection table with weights and precise values of mechanical and electrical properties as well as material and manufacturing costs is used. For the selection, Table X is proposed.

TABLE IX
COMPARISON OF ELECTRICAL AND MECHANICAL PROPERTIES.

	Rotor A	Rotor B	Rotor C
Maximum torque, Nm	1610	1790	1650
Efficiency at the rated point	0.94	0.94	0.94
Magnet price, €	1900	2100	1200
Maximum shear stress, MPa	35	39	40
Maximum centrifugal stress, MPa	216	289	195
Safety factor	2.2	1.6	2.4

TABLE X
OPTIMIZATION TABLE OF THE BUS ROTOR

	Rotor A	Rotor B	Rotor C	Weight %
Max. torque	0.96	1.06	0.98	25 %
Efficiency in the rated point	1	1	1	20 %
Durability	0.57	0.02	2.4	25 %
Magnet cost	-1.09	-1.20	-0.71	15 %
Manufacturing cost	-0.94	-0.97	-1.08	15 %
Total weight	27	13	78	Σ 100 %

In the selection table, the determinant factor in each design is divided by the corresponding mean value of all designs to achieve a relative index. The relative index in each criterion is then weighted based on its importance in this hybrid bus application in the Lappeenranta drive cycle.

Based on the optimization, rotor design C was selected, the fatigue life of which was long and which yields good electromagnetic performance and lowest manufacturing costs because of the smallest amount of expensive permanent magnet material compared with the other rotor designs.

VI. PROTOTYPE

The main dimensions and parameters of the traction motor are shown in Table XI.

TABLE XI
DIMENSIONS AND PARAMETERS OF THE BUS MOTOR

Parameter	Value
Stator stack (physical) iron length l_{Fe} , mm	225
Stator lamination space factor k_{Fe}	0.97
Stator inner diameter D_i , mm	263
Stator stack outer diameter D_{os} , mm	396
Stator yoke magnetic height h_{ys} , mm	20.5
Number of stator slots Q_s	48
Number of slots per pole and phase q	1
Stator skewing by one slot pitch, mm ($263 \times \pi / 48$)	17.21
Rotor lamination outer diameter D_o , mm	260
Rotor lamination inner diameter, D_{in} , mm	176
Rotor lamination stack length, l_{Fe} , mm	230
Rotor tangential tension σ_{tm} at the rated torque kPa	26.8
Rotor tangential tension $\sigma_{tm,max}$ at the max. torque kPa	80
Permanent magnet height, mm	6.5
Permanent magnet width, mm	39.15
Permanent magnet length per pole, mm	$4 \times 57 = 228$
Number of pole-pairs p	8
Number of slots per pole and phase q	1
Winding factor k_{w1} taking stator one slot pitch skewing into account	0.956
Effective coil turns in half-slot $z_{q/2}$ pcs	5
Stator coil turns in series per phase N_s	20

The stator and the rotor were manufactured from thin steel layers M270-50A. Each magnet was segmented to reduce eddy current losses. One magnet consists of four 57 mm long elements made of N38UH-material having a remanence of 1.15 T, a coercive field strength of 870 kA/m, and a permeability of 1.05 (at 120 C).

The flux density distributions in different steel areas are shown in Fig. 7 at the rated load. The figure is obtained from the 2D program of Cedrat.

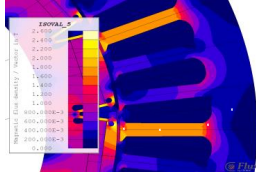


Fig. 7. Flux densities in the teeth and yoke points (shown in Fig. 11) in the rated operating point. Only the magnetic proportion of the yoke is taken into account in the calculation. Flux 2D computation.

The flux density variations as a function of time are shown in Fig. 8 in the corresponding positions (points 1–4). The maximum flux density reaches 1.85 T in the teeth.

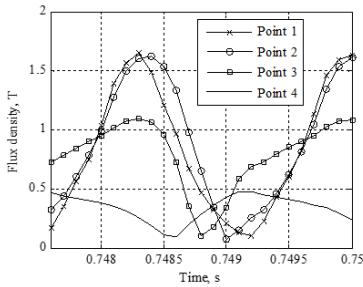


Fig. 8. Flux densities in the teeth and yoke of the final machine design C.

The torque ripple of the nonsmooth rotor type C was 27% of the rated torque. Therefore, the stator was skewed by 3.57 degrees. The torque ripple is presented in Fig. 9. Skewing of the rotor is not possible because simple permanent magnet shapes are used.

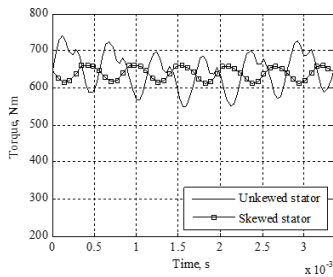


Fig. 9. Torque curves at the rated torque 639 Nm from the FEA.

The traction motor operation was designed for the drive cycle of Lappeenranta bus route 1, and according to the FEA, all operating areas can be covered. The authors also analyzed whether the designed motor meets the operating points of the Gothenburg line 85 drive cycle. The motor parameters and the drive cycle were analyzed in Matlab; the torque versus speed curves are depicted in Fig. 10. In the Gothenburg cycle, the following drive points are needed: a) 2240 min^{-1} , 640 Nm, 150 kW when operating in the motor mode, b) 740 min^{-1} , 1500 Nm, 116 kW in the motor mode, c) 1600 min^{-1} , 1400 Nm in

the generator mode, d) max. 230 kW power in the motor mode, and e) max. 416 kW power in the generator mode.

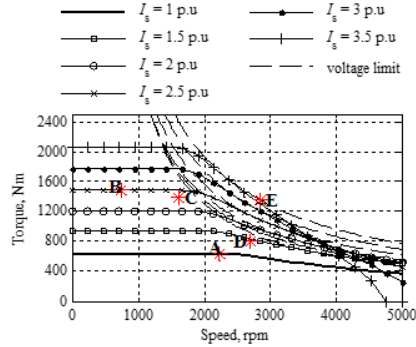


Fig. 10. Torque at different currents ($I_{\text{rated}} = 1$ p.u.). The results are obtained analytically. They could be used for preliminary estimation of the required current ratings. Point A is the rated value when operating in the motor mode. Point B is the maximum torque when operating in the motor mode. Point C is the maximum torque in the generator mode; point D indicates the maximum 228 kW power in the motor mode, and point E the maximum 416 kW power in the generator mode.

Fig. 11 shows one coil turn of the two-layer $q = 1$ winding during the winding procedure. In this winding type there are two independent three-phase windings with no phase shift, that is, two parallel branches. The two-layer winding was chosen to achieve as short end windings as possible.



Fig. 11. Stator stack was constructed to have a skew of 3.57 degrees. The winding is a two-layer winding to achieve short end windings.

Two converter units are supplying a modular winding structure. Should one inverter get damaged, the other could still continue supplying the motor. There are two independent winding sections in the stator, one section for each converter. The winding scheme is depicted in Fig. 12.

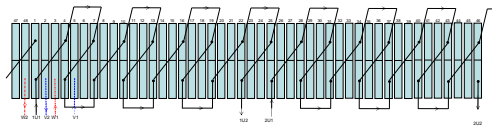


Fig. 12. Winding diagram for phase U supplied by two galvanically isolated converters.

The water jacket was implemented to the frame part and to the end shields to have sufficient cooling also for the end windings. The cylindrical frame was constructed from aluminum profile elements, shown in Fig. 13, to achieve a light weight.



Fig. 13. Stator frame and the end shield with cooling channels.

The thermal model was generated by the CFD applying the computed rated losses, cooling structures, and suitable thermal coefficients. The temperature of the liquid (50 % mix of water and glycol) coolant is assumed to be 50°C, the flow rate is 6 l/min, and the liquid duct height 30 mm and width 5 mm. The temperature distribution is shown in Fig. 14. According to the thermal analysis, the motor is sufficiently cooled during the rated operation. However, it is pointed out that the thermal computation parameters vary because the coolant temperature and fluid speed may vary in the bus, and also the ambient temperature will vary across the year (the assumed driving location is in Finland).

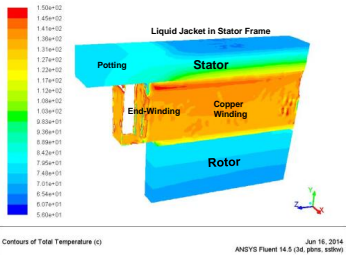


Fig. 14. Temperature distribution in the motor according to the CFD at the rated speed and load.

VII. EXPERIMENTAL RESULTS

The measurement results provide essential information to verify the electrical and thermal analysis. The measurements were carried out with commercial inverters and a 355 kW IM as the load-producing machine. The induced phase voltage waveform of the skewed machine obtained from the FEA is compared with the measured voltage waveform as shown in Fig. 15.

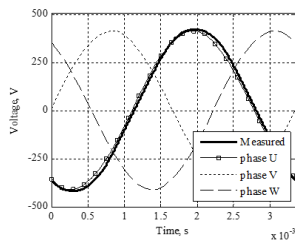


Fig. 15. Induced voltage waveforms from the FEA and the measurements as a function of time.

All six phases, three in both stators, were measured to ensure that the voltages are sinusoidal and equal in all phases. The voltages are shown in Fig. 16 a for stator 1 and in Fig. 16 b for stator 2.

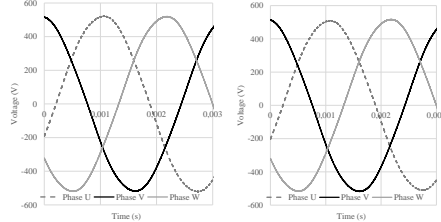


Fig. 16. Measured induced voltage waveforms from a) stator 1 and b) stator 2 as a function of time.

Fig. 17 shows the winding temperature rises and the coolant temperature at the rated load. The steady-state temperature was determined by performing a curve fitting. The curves of the best fit are shown for winding temperatures for the slot winding, the end windings, and the coolant at full load. The expected resultant copper temperature rise for a 100% load is about 100°C in the slot proportion of the winding and 107°C in the end winding. The coolant temperature rise is 15°C.

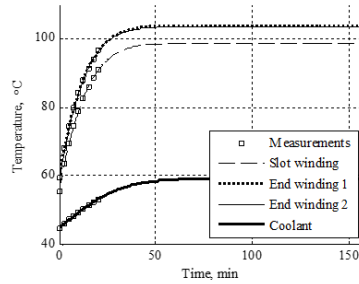


Fig. 17. Measured (from Pt100) and extrapolated temperature rise as a function of time in different parts of the winding and the coolant temperature.

The traction motor was tested by driving bus on flat road and climbing a hill. In Fig. 18, it is shown how the bus is accelerated to speed up to approximately 30 km/h and then stopped using regenerative braking. It can be seen from figure that great portion of energy used for acceleration can be recovered by braking with the traction motor only. Mechanical braking is actually useless if the road is not very slippery. On icy road the front wheels should always brake more than rear wheels. Climbing a hill is illustrated in Fig. 19. A Hill of 1:20 slope, which is the largest slope in the route 1 of Lappeenranta, was driven with a torque limit of 1100 Nm. The bus could accelerate well in the slope tested. The hill can be climbed with one inverter only as discussed in Section II. However, as can be seen from Fig. 19 the speed reduces in the middle portion of slope. In this location, the hill has a slope of 1:9. The bus could not start from standstill in the area of largest slope using one inverter only.

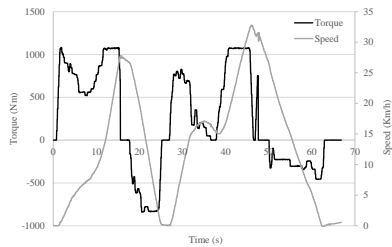


Fig. 18. Measured torque and speed of the studied hybrid bus.

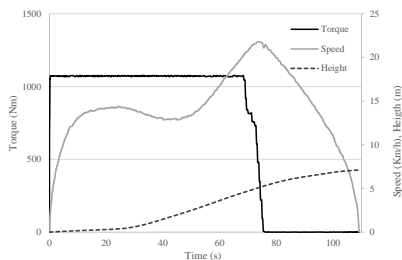


Fig. 19. Measured torque, speed and height of the studied hybrid bus on a slope.

VIII. CONCLUSION

The electrical and mechanical properties were analyzed for three different rotor designs. The most important mechanical aspect in the study was the fatigue life of the rotor laminations under actual duty cycles and the maximum stresses at the highest operating speed. The main tasks were to design a machine that can generate enough torque with a minimum magnet flux leakage and have a long enough rotor fatigue lifetime. As a result of the optimization, rotor design C was selected, the fatigue life of which is long enough and which yields a good electromagnetic performance and low manufacturing costs because of the smallest amount of expensive permanent magnet material compared with other rotor designs. The prototype machine is installed into a hybrid bus, and according to the preliminary test drives, it works as planned.

REFERENCES

1. M. Polikarpova, P. Ponomarev, P. Lindh, I. Petrov, W. Jara, V. Naumanen, J. A. Tapia, and J. Pyrhönen, "Hybrid cooling Method of Axial-Flux Permanent Magnet Machines for a Vehicle Application," *IEEE Trans. on Ind. Electron.*, vol. 62, no. 12, pp. 7382–7390, 2015.
2. C. Kral, A. Haumer, B. L. Sang, "A Practical Thermal Model for the Estimation of Permanent Magnet and Stator Winding Temperatures," *IEEE Trans. Power Electron.*, Vol. 29, no. 1, pp. 455–464, 2014.
3. A. Reinap, F. J. Marquez-Fernandez, R. Andersson, C. Högmärk, M. Alaküla, and A. Göransson, "Heat transfer analysis of a traction machine with directly cooled laminated windings", International Electric Drives Production Conference, EDPE, pp. 1–7, 2014.
4. C. E. Kilbourne, C. H. Holley, "Liquid cooling of turbine-generator armature windings", *Electrical Engineering*, Vol. 75, no. 5, pp. 436–441, 1956.

5. Y. Alexandrova, R. S. Semken, J. Pyrhönen, "Permanent magnet synchronous generator design solution for large direct-drive wind turbines: Thermal behavior of the LC DD-PMSG", *Applied Thermal Engineering*, Vol. 65, no. 1–2, pp. 554–563, 2014.
6. M. Degano, E. Carraro, N. Bianchi, "Robust optimization of a traction PMSM motor according to given driving cycles" *Int. Conference on Electrical Machines (ICEM)*, Germany, pp. 270–276, 2014.
7. M. Ferrari, N. Bianchi, E. Fornasiero, "Analysis of Rotor Saturation in Synchronous Reluctance and PM-Assisted Reluctance Motors", *IEEE Trans. Ind. Appl.*, Vol. 51, no. 1, pp. 169–177, 2015.
8. P. Niazi, H. A. Toliyat, A. Goodarzi, "Robust Maximum Torque per Ampere (MTPA) Control of PM-Assisted SynRM for Traction Applications", *IEEE Trans. Veh. Technol.*, Vol. 56, no. 4, pp. 1538–1545, 2007.
9. S.-I. Kim, S. Park, T. Park, J. Cho, W. Kim, S. Lim, "Investigation and Experimental Verification of a Novel Spoke-Type Ferrite-Magnet Motor for Electric-Vehicle Traction Drive Applications," *IEEE Trans. Ind. Electron.*, Vol. 61, no. 10, pp. 5763–5770, Oct. 2014.
10. A. M. El-Refai, J. P. Alexander, S. Galioto, P. B. Reddy, H. Kum-Kang, P. de Bock, and S. Xiochun, "Advanced High-Power-Density Interior Permanent Magnet Motor for Traction Applications," *IEEE Trans. Ind. Appl.*, Vol. 50, no. 5, pp. 3235–3248, Sep/Oct. 2014.
11. S. Galioto, P. B. Reddy, A. M. El-Refai, J. P. Alexander, "Effect of Magnet types on Performance of High-Speed Spoke Interior-Permanent-Magnet Machines Designed for Traction Applications", *IEEE Trans. Ind. Appl.*, Vol. 51, no. 3, pp. 2148–2160, May/June 2015.
12. V. Ruuskanen, J. Nerg, J. Pyrhönen, S. Ruotsalainen, R. Kennel, "Drive Cycle Analysis of a Permanent-Magnet Traction Motor Based on Magnetostatic Finite-Element Analysis," *IEEE Trans. Veh. Technol.*, vol. 64, no. 3, pp.1249–1254, Mar. 2015.
13. V. Ruuskanen, J. Nerg, A. Parviainen, M. Rilla, J. Pyrhönen, "Design and Drive-Cycle Based Analysis of Direct-Driven Permanent Magnet Synchronous Machine for a Small Urban Use Electric Vehicle" in *Proc. 16th European Conference On Power Electronics and Applications (EPE-ECCE)*, pp. 1–7, Aug. 2014.
14. X. Hu, N. Murgovski, L. M. Johannesson, and B. Egardt, "Optimal Dimensioning and Power Management of a Fuel Cell/Battery Hybrid Bus via Convex Programming", *IEEE/ASME Trans. Mechatr.*, Vol. 20, no. 1, pp. 457–468, Feb. 2015
15. J. Nerg, M. Rilla, V. Ruuskanen, J. Pyrhönen, and S. Ruotsalainen, "Direct-Driven Interior Magnet Permanent-Magnet Synchronous Motors for a Full Electric Sports Car", *IEEE Trans. Ind. Electron.*, Vol. 61, no. 8, pp. 4286–4294, 2014.
16. X. Chen, J. Wang, B. SEN, P. Lazari, and T. Sun, "A High-Fidelity, Computationally Efficient Model for Interior Permanent Magnet Machines Considering the Magnetic Saturation, Spatial Harmonics and Iron Loss Effect," *IEEE Trans. Ind. Electron.*, early access 2015.
17. K. Yamazaki, and M. Kumagai, "Torque Analysis of Interior Permanent Magnet Synchronous Motors by Considering Cross-Magnetization: Variation in Torque Components With Permanent-Magnet Configurations," *IEEE Trans. Ind. Electron.*, Vol. 61, no. 7, pp. 3192–3201, 2014
18. A. M. EL-Refai, T.M. Jahns, P. J. McCleer, and J. W. McKeever, "Experimental Verification of Optimal Flux Weakening in Surface PM Machines Using Concentrated Windings", *IEEE Trans. Ind. Appl.*, Vol. 42, n0. 2, March/April 2006.
19. P. B. Reddy, H. Kum-Kang, A. M. El-Refai, "Generalized Approach of Stator Shifting in Interior Permanent-Magnet Machines Equipped With Fractional-Slot Concentrated Windings", *IEEE Trans. Ind. Electron.*, Vol. 61, no. 9, pp. 5035–5046, 2014.
20. L. Chong, R. Dutta and M. F. Rahman, "Field Weakening Performance of a Concentrated Wound PM Machine with Rotor and Magnet Geometry Variation", *Power and Energy Society General Meeting*, pp. 1–4, July 2010.
21. G. Pellegrino, A. Vagati, P. Guglielmi, and B. Boazzo, "Performance Comparison Between Surface-Mounted and Interior PM Motor Drives for Electric Vehicle Application," *IEEE Trans. Ind. Electron.*, Vol. 59, no. 2, pp. 803–811, Feb. 2012.
22. Boldea, L. N. Tutela, L. Parsa, and D. Dorrell, "Automotive Electric Propulsion Systems with Reduced or No Permanent Magnets: An Overview", *IEEE Trans. Ind. Electron.*, Vol. 61, no. 10, pp. 5696–5711, Feb. 2014.
23. D. Dorrell, L. Parsa, and I. Boldea, "Automotive Electric Motors, Generators, and Actuator Drive Systems with Reduced or No Permanent

- Magnets and Innovative Design Concepts" *IEEE Trans. Ind. Electron.*, Vol. 61, no. 10, pp. 5693–5695, 2014.
24. T. Aho, J. Nerg, J. Sopenan, J. Hupponen, and J. Pyrhönen, "Analyzing the Effect of the Rotor Slit Depth on the Electric and Mechanical Performance of a Solid-Rotor Induction Motor." *Int. Rev. Electr. Eng.*, vol. 1, no. 4, pp. 516–524, 2006.
 25. P. Mercocelli, "A Hysteresis Hybrid Extended Kalman Filter as an Observer for Sensorless Valve Control in Camless Internal Combustion Engines", *IEEE Trans. Ind. Appl.*, vol. 48, no. 6, pp. 1940–1949, Nov. 2012.
 26. P. Immonen, P. Lindh, H. Niemelä, J. Pyrhönen, S. Sinkko, and M. Kasurinen, "Energy saving by hybridization of a city bus", *the 16th European Conference on Power Electronics and Applications EPE ECCE 2014*, pp. 1–8, 2014.
 27. M. Gerami Tehrani, and J. Sopenan, "Torsional Vibration Analysis of Multiple Driving Mode Hybrid Bus Drivetrain", *ASME Design Engineering Technical Conferences and Computers and Information in Engineering Conference 2014*, Aug., New York, USA, pp. 1–8, 2014.
 28. P. Immonen, J. Pyrhönen and P. Lindh, Report of Lappeenranta City bus cycle: Lappeenranta Route 1, www.doria.fi/handle/10024/93685 on 30.11.2013, Year 2013.
 29. J. D. McFarland, T. M. Jahns, "Investigation of the Rotor Demagnetization Characteristics of Interior PM Synchronous Machines During Fault Conditions", *IEEE Trans. Ind. Appl.*, Vol. 50, no. 4, pp. 2768–2775, 2014.
 30. P. M. Lindh, P. Immonen, Y. Alexandrova, M. Gerami Tehrani, J. J. Pyrhönen, and J. T. Sopenan, "The design of rotor geometry in a permanent magnet traction motor for a hybrid bus," *Proc. of 2014 Int. Conference on Electrical Machines (ICEM)*, pp. 310–315, 2014.
 31. Y. Gao, R. Long, Y. Pang, and M. Lindemmo, "Fatigue Properties of an Electrical Steel and Design of EV/HEV IPM Motor Rotors for Durability and Efficiency," SAE International, Warrendale, PA, SAE Technical Paper 2010-01-1308, Apr. 2010.
 32. A. Hobbacher and others, in Recommendations for fatigue design of welded joints and components, XIII-2151r4-07 / XV-1254r4-07., Welding Research Council Shaker Heights, OH, pp. 45–46, 2013.
 33. S. Suresh, in Fatigue of Materials, Cambridge University Press, 1998, p. 223.
 34. T. J. Barlow, S. Latham, I. S. McCrae, P. G. Boulter, A reference book of driving cycles for use in the measurement of road vehicle emissions, Project Report, vol. 1, version 3, 2009.

Pia Lindh (M'04) born in Helsinki in 1969, received her M.Sc. degree in energy technology in 1998 and her D.Sc. degree in electrical engineering (Technology) in 2004 from Lappeenranta University of Technology (LUT), Lappeenranta, Finland. She is currently serving as an associate professor at the Department of Electrical Engineering in LUT Energy, Lappeenranta, where she is engaged in teaching and research of electric motors and electric drives.

Mohammad Gerami Tehrani born in 1984, Tehran, Iran, received his B.E. degree in Mechanical engineering from the Azad University of Dezful, Iran, in 2009. He has also worked in electric vehicle product development Valmet Automotive Inc. 2013. He pursued his studies towards M.Sc. degree in mechanical engineering from Lappeenranta University of Technology (LUT), Lappeenranta, Finland, in 2013, where he is currently working towards the Ph.D. degree on design of electro-mechanical systems. His research interests are electric machine design, electric vehicle powertrain design, gearbox efficiency and mechatronic system control design.

Tuomo Lindh was born in Lappeenranta, Finland, in 1964. He received the B.Sc. degree in Mechanical Engineering from Mikkeli Institute of Technology, Mikkeli, Finland, in 1989 and the M.Sc. and D.Sc. degrees in technology from Lappeenranta University of Technology, Lappeenranta, in 1997 and 2003, respectively. Since 1997, he has been with Lappeenranta University of Technology. He is currently an Associate Professor. His research interests include generator and motor drives and system engineering, particularly in the areas of distributed power generation, electric vehicles, and mechatronics.

Jan-Henri Montonen was born in 1985 in Mikkeli, Finland. He received his Master of Science degree in electrical engineering from Lappeenranta University of Technology in 2012. He is currently a PhD student in the School of Energy Systems in LUT, where he is engaged in teaching and research of

control engineering and digital systems. His research work focuses on virtual simulation and intelligent control of electrically driven mechatronic systems.

Juha Pyrhönen (M'06), was born in 1957 in Kuusankoski, Finland, received the Doctor of Science (D.Sc.) degree in Electrical Engineering from Lappeenranta University of Technology (LUT), Finland in 1991. He became an Associate Professor of Electrical Engineering at LUT in 1993 and a Professor of Electrical Machines and Drives in 1997. He is engaged in research and development of electric motors and electric drives. His current interests include different synchronous machines and drives, induction motors and drives and solid-rotor high-speed induction machines and drives.

Jussi T. Sopenan (M'14) was born in Enonkoski, Finland, in 1974. He received the M.Sc. degree in mechanical engineering and the D.Sc. (Technology) degree from Lappeenranta University of Technology (LUT), Lappeenranta, Finland, in 1999 and 2004, respectively. He was a Researcher with the Department of Mechanical Engineering, LUT, in 1999–2006. He was also a Product Development Engineer with the electric machine manufacturer Rotatek Finland Ltd., in 2004–2005 Lappeenranta, Finland. During 2006–2012, he was a Principal Lecturer of mechanical engineering and the Research Manager of the Faculty of Technology, Saimaa University of Applied Sciences, Lappeenranta. He is currently a Professor of machine dynamics with LUT. His research interests are rotor dynamics, multibody dynamics, and mechanical design of electrical machines.

Markku Niemelä received the B.Sc. degree in electrical engineering from Helsinki Institute of Technology, Helsinki, Finland, in 1990 and the M.Sc. and D.Sc. degrees in technology from Lappeenranta University of Technology (LUT), Lappeenranta, Finland, in 1995 and 1999, respectively. He is currently a Senior Researcher with the Carelian Drives and Motor Centre, LUT. His current interests include motion control, control of line converters, and energy efficiency of electric drives.

Yulia Alexandrova completed the M.Sc. degree in Electrical Engineering from SPbETU "LETI" (Russia, Saint-Petersburg) and Lappeenranta University on Technology (Finland, Lappeenranta) in 2009. She continues the educational process toward the D.Sc. degree at Department of Energy, Electrical Engineering. Her current interest focuses on the analytical calculations and numerical simulations of high-torque low-speed electrical machines.

Paula Immonen received the M.Sc. Degree in electrical engineering and the D.Sc. (Technology) degree from the Lappeenranta University of Technology (LUT), Lappeenranta, in 2008 and 2013, respectively. She is currently working as a post-doctoral researcher in the Department of Electrical Engineering at LUT. Her current research interest is the diesel-electric hybrid drive system in mobile working machines.

Lassi Aarniovuori (M'15) was born in Jyväskylä, Finland, in 1979. He received the M.Sc. and D.Sc. degrees in electrical engineering from Lappeenranta University of Technology (LUT), Lappeenranta, Finland, in 2005 and 2010, respectively. He is currently a Post-doctoral Researcher in the Department of Electrical Engineering, LUT. His current research interests include the field of electric drives, especially simulation of electric drives, efficiency measurements, and calorimetric measurement systems.

Maria Polikarpova was born in 1985 in Severodvinsk, Russia, received the Specialist Degree in Industrial Heat and Power from Saint-Petersburg Technological University of Plant Polymers, Russia in 2008 and PhD degree in Electrical Engineering from Lappeenranta University of Technology (LUT), Finland in 2014. Her research interests focus on thermal analysis and cooling solutions for electrical machines and power electronics. She is currently a student at LUT Business School.

Publication VI

Sikanen, E., Heikkinen, J., Nerg, J., Gerami Tehrani, M., Sopanen, J.

**Fatigue life calculation procedure for the rotor of an embedded magnet traction motor
taking into account thermomechanical loads**

Reprinted from

Mechanical Systems and Signal Processing

Vol. 111, pp. 36–46. 2018,

© 2018, with permission from Elsevier.



Contents lists available at ScienceDirect

Mechanical Systems and Signal Processing

journal homepage: www.elsevier.com/locate/ymsp

Fatigue life calculation procedure for the rotor of an embedded magnet traction motor taking into account thermomechanical loads

Eerik Sikanen^{*}, Janne Nerg, Janne E. Heikkinen, Mohammad Gerami Tehrani, Jussi Sopanen

LUT School of Energy Systems, Lappeenranta University of Technology, Skinnarilankatu 34, 53850 Lappeenranta, Finland

ARTICLE INFO

Article history:

Received 10 September 2017
 Received in revised form 26 February 2018
 Accepted 30 March 2018
 Available online 5 April 2018

Keywords:

Electromagnetic
 Fatigue analysis
 Electric vehicle
 Mechanical design
 Permanent magnet traction motor
 Thermal design

ABSTRACT

Working cycle and load fluctuation have to be considered in the design process of traction motors in order to be able to optimize the size, life cycle, and performance of the electric drive. The total stress and fatigue life of an electric motor rotor are determined to a large extent by centrifugal forces, tangential forces caused by torque, and the temperature gradient along the rotor. Rapid increase in heat as a result of sudden variation in the electric current and the differing thermomechanical characteristics of the components leads to non-uniform stress in the assembly. By applying the principle of superposition to the transient mechanical and thermal stress, a multidisciplinary method is proposed for the calculation the equivalent von Mises stress for a fatigue life analysis. This paper presents a fatigue life calculation procedure considering the mechanical and thermal stresses. The method is presented using the rotor of the Electric RaceAbout (ERA) traction motor as a case example. The presented approach is validated by comparing simulated and measured temperature data from ERA drive tests at the Nürburgring Nordschleife track. The results indicate the great importance of taking into consideration both mechanical and thermal loads in lifetime calculation.

© 2018 The Authors. Published by Elsevier Ltd. This is an open access article under the CC BY license (<http://creativecommons.org/licenses/by/4.0/>).

1. Introduction

The electrical machine is one of the key components in electrical traction technology. Typical requirements for electric traction motors are a high power density and high efficiency over wide torque and speed ranges. The trend in traction applications is to use a different variations of permanent magnet synchronous motor (PMSM) which has numerous beneficial features for this purpose. Since the vehicular applications impose many simultaneous requirements for traction drives, many different traction motor drives and drivetrain architectures has been proposed [1–3].

Multidisciplinary analysis considering electromagnetic, thermal and mechanical fields should be adopted when optimizing designs of traction motors. Quite often this is done by evaluating the electromagnetic performance as a function of rotational speed of the machine and utilizing the calculated electromagnetic losses as heat sources in thermal analysis. In addition, electromagnetic forces are utilized in mechanical analysis to find out the noise and vibration characteristics [4,5]. The aforementioned design procedure reveals the bottlenecks of the electrical machine design, but it is by no means

^{*} Corresponding author.

E-mail address: eerik.sikanen@lut.fi (E. Sikanen).

<https://doi.org/10.1016/j.ymsp.2018.03.055>

0888-3270/© 2018 The Authors. Published by Elsevier Ltd.

This is an open access article under the CC BY license (<http://creativecommons.org/licenses/by/4.0/>).

Nomenclature

b	Basquin exponent or fatigue strength exponent
k	number of the rainflow stress classes
n	rotational speed (rpm)
N	number of stress cycle repetitions in total
N_f	number of equivalent applied stress cycles
P	power loss (W)
T	torque (Nm)
z_i	number of repetitions in i th stress class
β	S-N curve slope
σ	stress (Pa)
σ_f	fatigue strength coefficient
$\Delta\sigma$	stress variation
$\Delta\sigma_{eq}$	calculated equivalent stress (Pa)

optimized for traction motors. Since the operating conditions in traction motors vary significantly, the multidisciplinary analysis should be conducted over the drive cycle as was done, for example, in Fatemi et al. [6].

The calculation of mechanical stresses and fatigue life of PMSM rotor structure in traction applications is often based on different analytical and finite element (FE) based numerical approaches. According to the results found for instance in Chai et al. [7], Knetsch et al. [8], and Lindh et al. [9], the centrifugal force acting on the rotor structure is considered to be the dominant stress source, but in all the cases the effect of the thermal loads on the mechanical stresses and fatigue life were neglected. The total stress level is directly coupled with the fatigue life that can be analyzed by different methods as introduced in [10]. Mechanical stresses caused by internal and external loads and centrifugal force have an effect on the fatigue life of an electric motor. Furthermore, stresses generated by thermal loads that can be caused by ambient temperature variation or internally generated heat losses affect the fatigue life. While the effect of temperature on the electromechanical properties of components and the electric machine performance has been studied from many different perspectives, the influence of thermal loads on the mechanical durability of rotor assemblies has received limited attention.

According to the published literature, the interest of thermomechanical stress effects in electrical machines are limited to the degradation of stator insulation [11] or rotor bar braking mechanisms in squirrel-cage induction machines [12]. In the traditional mechanical dimensioning of the rotor structure of a permanent magnet traction motor the thermomechanical stresses are usually neglected, leading to a fact that the mechanical dimensioning is based mostly on the centrifugal forces affecting to the rotor.

In this paper, a calculation method of performing a thermomechanical fatigue life analysis for a rotor of an electric traction motor over the known drive cycle is presented. The fatigue life calculation with inclusion of thermal expansion induced stress in the rotor part using real drive cycle gives much more realistic fatigue life estimation compared to the standard approach where only the centrifugal loads are included. The proposed calculation method can be utilized in the structural optimization of the traction motor rotor on the given drive cycle. The presented stress calculation procedure is a combination of analytical and finite element methods (FEM) and developed such that it allows solution over the drive cycle within a reasonable computational effort.

The proposed thermomechanical fatigue life analysis was applied in the analysis of a permanent magnet synchronous motor used as a traction motor in a full electric sports car. Data measured from the rear right wheel of the vehicle running on the Nürburgring Nordschleife track [13] was utilized as the drive cycle. As an end result of this study, an important discovery was made. Based on the analyzed traction motor within the utilized drive cycle, it was found out that the thermal expansion induced stresses are actually greater than the mechanical stresses. Also, the combined thermal–mechanical stresses are significantly greater than, typically studied, centrifugal force induced stresses only. These findings represent the importance of using the real drive cycle and the calculation procedure proposed in this paper as part an electric traction motor design.

2. Thermomechanical analysis

The proposed procedure for thermomechanical analysis of a permanent magnet traction motor rotor under mechanical and thermal loads consists of four main stages. Firstly, utilizing the rotational speed and torque data of the drive cycle, the sources of heat generation, that is rotor losses, and convection coefficients from the rotor surface to surrounding air are identified. Secondly, the transient thermal FEM is applied to evaluate the temperature distribution within the drive cycle. Thirdly, the stress calculation at every calculation time instants is performed utilizing static structural FEM. Finally, the fatigue life is estimated from the stress history during the drive cycle.

2.1. Rotor losses

In the proposed procedure, the heat imposed on the rotor stack and the consequent thermal stress is the point of interest. The heat flow affecting the rotor lamination is thus investigated. Data recorded during the operation of an actual electric vehicle on a race track are utilized to evaluate the temperature variation resulting from power losses in the electric motor rotor. The rotor loss calculation is discussed in detail in Section 3.

2.2. FEM process

A finite element method is used to solve the stress history. The finite element analysis (FEA) is done in two steps; first, transient thermal study is carried out over the drive cycle to calculate the temperature distribution. In the second step, the temperature distribution is applied as an initial thermal condition for every simulation time step together with other mechanical loads. Fig. 1 presents a schematic of the simulation steps describing the inputs and output.

In the transient thermal FEA, the temperature distribution within the electrical motor rotor is calculated as a function time. In FE model, the rotational speed and torque depended heat losses are modeled as volumetric heat sources in the magnets and lamination bodies. Convective heat transfer boundaries are applied to the model describing the forced air cooling. The convection coefficients used are dependent on the rotational speed of the rotor.

In the mechanical static structural FEA, the previously solved temperature history is used as one of the inputs. In every simulation step, the thermal expansion effect must be converted into force distribution in order to provide superposition of all the mechanical forces. The conversion from temperature into force is done as pre-process by solving first only the strain caused by thermal expansion. The solved strain is then converted into force using stiffness properties of the mechanical FE model. Then, the rest of the mechanical force are applied, the centrifugal forces from the rotational speed and the tangential forces generated by the torque. Finally, all the mechanical forces are combined to solve the stress history.

2.3. Fatigue life calculation

When evaluating the durability of the system, a fatigue life calculation was carried out using the stress history calculated in the FEM process. The fatigue life was then calculated with and without thermal loads to analyze the influence of the temperature variation on the rotor lifecycle.

The Palmgren-Miner linear damage hypothesis method and rainflow cycle counting were applied to evaluate the equivalent stress cycle $\Delta\sigma_{eq}$ from a complex and non-uniform stress history. The equivalent stress was employed to identify the stress reversals and for damage summation to the structure [14,15]. The equivalent stress cycle that causes similar fatigue to the rotor as cumulative fatigue damage during the load cycle can be formulated as

$$\Delta\sigma_{eq} = \sqrt{\frac{\sum_{i=1}^k z_i \Delta\sigma_i^\beta}{N}} \quad (1)$$

where k is the number of the rainflow stress classes, z_i is the number of repetitions in class i , $\Delta\sigma$ is the stress variation in the class, β is the S-N curve slope, and N is the number of stress repetitions in total. The number of rainflow stress classes is selected for each stress history curve independently using a suitable binwidth, which can be defined as suggested by

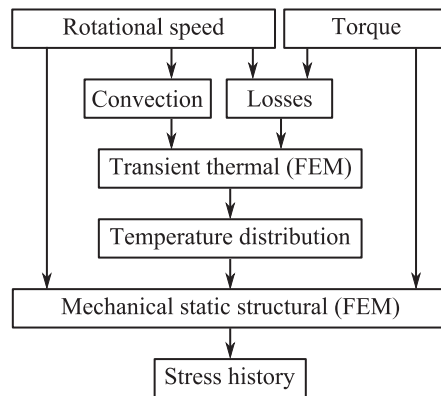


Fig. 1. Process of the thermomechanical analysis.

Shimazaki and Shinumoto in [16]. The selected binwidth considers the minimum and maximum stresses and stress variation over the stress history. The binwidth should be small enough to take into consideration the essential stress variation.

The Basquin equation for the number of applied equivalent stress fluctuations N_f that the structure tolerates until fatigue damage is developed can be solved from the following equation [17]

$$N_f = 0.5 \left(\frac{\Delta\sigma_{eq}}{2\sigma_f} \right)^{1/b} \quad (2)$$

where σ_f is the fatigue strength coefficient and b is the Basquin exponent or the fatigue strength exponent, which varies between -0.05 and -0.12 for most metals. From (2), a smaller b results in a longer fatigue life [18,19]. Based on published fatigue test results for a similar rotor laminate material in [20], the following fatigue strength coefficient, fatigue strength exponent and S-N curve slope for the machine cut edges were adopted in this study: $\sigma_f = 673.25$ MPa, $b = -0.09559$ and $\beta = 3$.

3. Case study: full electric race car

The thermomechanical analysis presented in Section 2 was applied to a three-phase sixteen-pole double-deck embedded permanent magnet traction motor originally designed for a full electric sports car Electric RaceAbout, the details of which are found in [13]. The electric machine main dimensions are given in Table 1.

As presented in [13], the majority of the machine losses occur in the stator windings. In order to obtain efficient enough cooling of the stator, the cooling of the PMSMs is carried out by combining air cooling in the air gap region and liquid cooling in the stator frame. Most of the stator iron and Joule losses are removed by liquid cooling, and the rotor surface is cooled by forced air cooling. Thus, the machine can be considered to be of open type. The structure of a single pole of the analyzed PMSM is depicted in Fig. 2.

The input for the thermomechanical analysis consists of the rotational speed and torque from the machine drive cycle and the corresponding thermal loads. All the input variables are needed as a function of time. In the studied case, the measured data from the Nürburgring Nordschleife race track was used as a drive cycle. Fig. 3 presents the measured rotational speed, torque, voltage and current on the rear left electric motor during one race track lap.

The thermal loads within the drive cycle, that is, the eddy current losses in the permanent magnets and the iron losses in the rotor laminations were calculated by 2D-FEM. The eddy current losses in the permanent magnets were calculated by treating them as short-circuited solid conductors in the transient finite element analysis. Rotor iron loss calculation was carried out using a loss-surface model implemented in the Flux2D software package by Cedrat. The loss calculation was performed at 1000 r/min applying transient FEM in such a way that the whole useful torque region, that is from no-load to break-down torque, at 1000 r/min was calculated. Temperature effects on the electromagnetic performance were not taken into account. Because eddy current losses are proportional to frequency squared, the whole rotational speed and torque range can be covered by scaling the permanent magnet eddy current losses calculated at 1000 rpm with respect to the investigated rotational speed using the relation:

$$P(n, T) = \left(\frac{n}{1000 \text{ rpm}} \right)^2 P(1000 \text{ rpm}, T) \quad (3)$$

where $P(n, T)$ is the eddy current loss at a rotational speed of n rpm and a torque of T , and $P(1000 \text{ rpm}, T)$ is the calculated eddy current loss at 1000 rpm with T . Because of the synchronous operation, the rotor iron losses remain at a very low level in the studied rotational speed range. At the nominal point, that is, at speed 1000 r/min and torque 240 Nm, the permanent magnet eddy current losses are 84.4 W and the rotor iron losses 5.3 W, respectively. At 2000 r/min and 240 Nm, the

Table 1
Main parameters of the PMSM.

Stator tooth width	11.6 mm
Stator slot height	32.5 mm
Stator outer diameter	380 mm
Stator bore diameter	287 mm
Active stator stack length	65 mm
Active rotor stack length	68 mm
Rotor outer diameter	284.2 mm
d-axis air gap length (min)	1.4 mm
q-axis air gap length (max)	5.5 mm
Width of the upper magnet	47.9 mm
Width of the lower magnet	43.9 mm
Thickness of the upper magnet (max value)	8.5 mm
Thickness of the lower magnet	6 mm

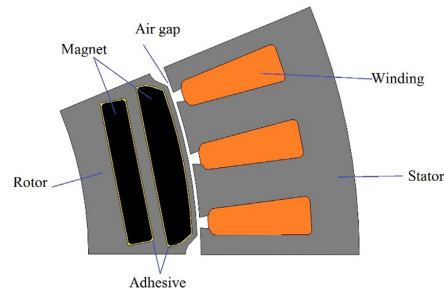


Fig. 2. Structure of one pole of the analyzed PMSM.

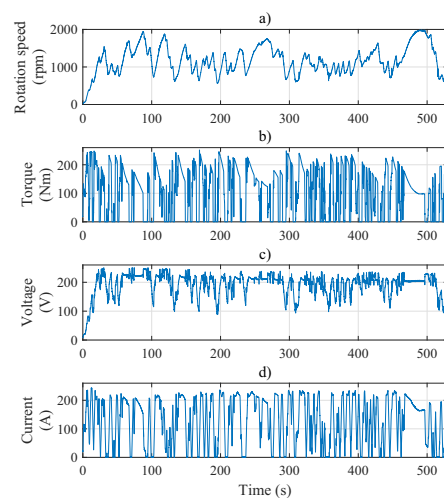


Fig. 3. Measured track data: (a) rotational speed (rpm), (b) torque (Nm), (c) voltage (V), and (d) current (A) [13].

permanent magnet eddy current losses are 337.6 W and the rotor iron losses 7.3 W. The majority of the permanent magnet eddy current losses occur in the upper magnet.

The thermomechanical analysis was performed using three-dimensional (3D) FEM in Ansys. In view of the computational effort required for a combined transient thermal and mechanical study of this size, the 3D-model is limited only to the rotor structure. This is justified for the following reasons. Firstly, because stator losses are effectively removed by combined liquid and forced air cooling, the effect of the stator losses to the thermal state of the rotor can be neglected. Secondly, the rotor losses are removed by convection to the air gap flow, which can be modeled with convection boundary condition set to the outer surfaces and the ends of the rotor structure. Thirdly, due to the relatively low rotor losses and the short active rotor stack length, 65 mm, heating of the cooling air in the air gap can be neglected to simplify the analysis, and thus, the air gap temperature applied to simulation is constant and equal to the ambient air temperature. The model can be further reduced by taking advantage of the symmetry and periodicity conditions. Because of the equal power loss density and identical cooling conditions, there is a periodicity at the edges of rotor poles. Therefore, only one rotor pole has to be considered. In the axial direction, the rotor structure, cooling conditions as well as the thermal loads are identical, which makes it possible to reduce the needed model to only one half of the axial length of the rotor. Therefore the 3D-model shown in Fig. 4 comprises of 1/32 of the rotor stack.

The utilized loads and boundary conditions of the model shown in Fig. 4 are discussed next. In transient thermal model, the thermal loads are inserted to volumes B1, B2, and B3 as volumetric heat generation as a function of time. Boundary condition describing convective heat transfer from rotor outer surface to the air gap flow is inserted to surfaces marked as C1. The convection coefficient depends on the rotational speed. Similarly, a boundary condition describing rotational speed

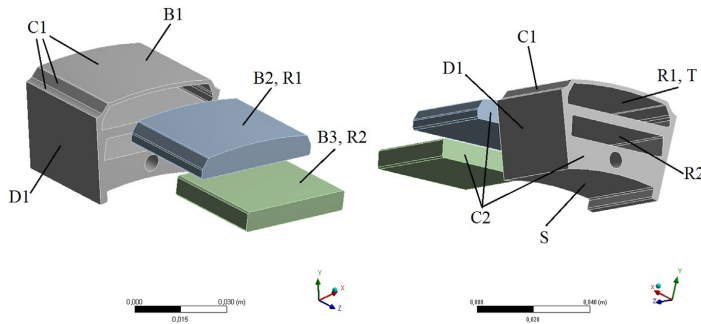


Fig. 4. The 3D-model used in thermomechanical analysis including utilized loads and boundary conditions.

dependent axial convection heat transfer is set to surfaces marked as C2. The air temperature of the air gap is set to correspond to the ambient temperature of 22 °C and assumed constant throughout the drive cycle. In the thermal model, magnets and rotor iron are modeled using their thermal conductivity, specific heat, and density. Adhesive layers are neglected from the model geometry, but their effect is included in a form of thermal contact resistance between the contact surface R1 and R2. The result from the transient thermal study is the temperature distribution within the rotor structure, which is utilized as an input variable in static structural analysis in Ansys.

In the mechanical analysis the centrifugal force due to the rotational speed affecting all the solid bodies B1, B2 and B3 was taken into account by inserting the measured rotational speed of the race track to the model in such a way that the rotation axis is located at the center point of surface S. The contact between permanent magnet and rotor iron are modeled as mechanical body-to-body contacts set to surfaces R1 and R2. The no-separation contact mode in Ansys was used, because it allows a minor slip but, at the same time, ensures that the contact between magnet and the rotor iron remains closed. Circular symmetry constraint in surfaces marked as D1 prevents tangential displacement, but at the same time it allows radial and axial displacement. Axial displacement constraint is set to surfaces C2.

In order to minimize the computational time, besides the geometrical symmetry used, the finite element mesh is optimized. In the thermal model, a coarser mesh was noticed to yield the same results than the denser mesh. Due to transient nature of the study, the coarse mesh was utilized. In the mechanical study more accurate mesh is a standard requirement. Therefore, more dense mesh was utilized in the mechanical model. Additional biasing was implemented to achieve converged mesh at the highest stress locations shown in Fig. 6.

Since the circular symmetry constraints and biased FE mesh are used, the effect of torque is modeled using tangential force set to surface T. The cylindrical coordinate system used is aligned along the same axis of rotation than in case of centrifugal force. The material properties used in the thermomechanical analysis are shown in Table 2. The data were obtained from the manufacturers' online material.

4. Results

Fig. 5 shows the measured temperature from the stator windings and the calculated highest temperature point in the rotor model located in the upper magnet. The scales of the temperatures are clearly different because the temperature of the windings rises to 145 °C and the temperature of the rotor to only 47 °C. Even though the temperatures are obtained from different locations, the trends of the curves can be compared with each other. The calculated temperature increases faster

Table 2
Material parameters of the components.

Material properties	Magnets (Neorem753A)	Steel (M270-50A)	Adhesive
Density (kg/m ³)	7600	7650	1207
Young's modulus (MPa)	150,000	200,000	–
Poisson's ratio	0.24	0.3	–
Yield strength (MPa)	75	470	–
Ultimate strength (MPa)	290	585	–
Specific heat (J/(kg C))	450	460	1173
Thermal expansion (1/K)	6e–6	1.2e–5	–
Thermal conductivity (W/(m K))	8.5	39	0.3

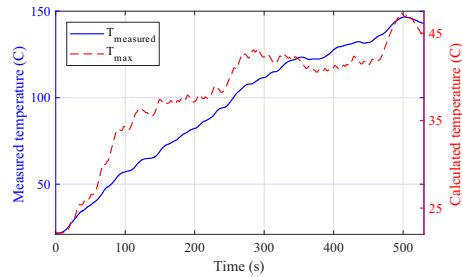


Fig. 5. Measured stator winding temperature vs. calculated rotor temperature.

between 70 and 100 s from the start of the cycle. After the first 100 s, the temperature in the rotor model increases more slowly than in the windings until the time point of 240 s, when the rotor temperature starts to increase faster than the temperature in the windings. Then, 40 s later, that is, at the time point 280 s, the rate of increase becomes slower again until the final rapid increase just before the end of the cycle.

When the relative temperature increase is compared with the measurements shown in Fig. 5, it can be seen that the faster temperature increase in the rotor is related to driving at full throttle, which can be obtained from the rotational speed curve in Fig. 3. This finding indicates that, as would be expected, the temperature increase in the rotor core is highly dependent on the loading of the motor. On the other hand, because the windings are indirectly liquid cooled, the temperature rise is not as highly dependent on the differential changes in the heat sources, and the temperature change is steadier along the drive cycle. The drive cycle is a race lap with full performance of the vehicle, which consumes most of the energy storage capacity and heats the motors to a level that prevents continuous operation at this performance level. For these reasons, the temperature curves start from the ambient temperature and end up at a much higher level, which cannot be used as an initial condition in consideration of the single race lap.

A general overview of the maximum stress areas found in the stress analysis is presented in Fig. 6. The highest stress concentration is located in the magnet pocket upper fillet. According to previous studies [9], the tension bars mostly carry the centrifugal and shear forces of the magnets, and the maximum von Mises stress generally occurs in the fillet section, where the stress concentration resulting from the centrifugal forces is highest. Furthermore, the magnetic flux is denser around the air barriers in the magnet housing, and thus, more eddy currents are induced in regions where the structure is exposed to a high stress level [21]. This stress parallax emphasizes the importance of thermal effects in stress analysis. The equivalent stress is calculated to observe the stress fluctuation.

Table 3 presents the maximum stress during the drive cycle history of each studied loading case and the corresponding design safety factor. The safety factors are calculated against the yield strength of the lamination material given in Table 2.

Table 3 gives the proportions of the different load types. The stress results are calculated using the full drive cycle input data but applying only one particular load component at a time. As expected, the dominating force components are mechanical and thermal forces. In this particular case, the mechanical design is very conservative and the highest stress caused by centrifugal force is only 43 MPa, which is unexpectedly low for a traction motor application. The most interesting values are the proportions of electromagnetic forces, which clearly play a minor role when evaluating the magnitudes of different force types, and the force caused by angular acceleration, which is remarkably low that it can be neglected. The safety factors in

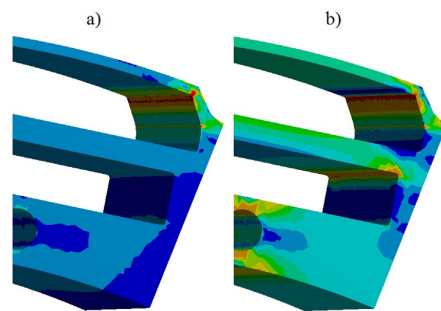


Fig. 6. Rotor stress distribution: (a) thermal stress only and (b) centrifugal stress only.

Table 3

Maximum stress and safety factor results. Cases A–F are different load conditions as follows: A – centrifugal forces, B – thermal loads, C – electromagnetic torque, D – electromagnetic radial force, E – angular acceleration, F – all loads combined.

Load type	A	B	C	D	E	F
Max stress (MPa)	43	56	4.2	2.8	0.013	80
Safety factor	11	8.5	110	170	36,000	5.9

Table 3 are calculated against the lamination material yield strength, 470 MPa, given in Table 2. Due to minor role of angular acceleration, the safety factor becomes excessive. The combined stress is obviously largest, but the value is lower than the sum of individual stress components owing to method of evaluating the von Mises stress, which combines the different multi-axial stress components.

Fig. 7 shows the maximum von Mises stress caused by mechanical, thermal, and combined loads during the studied load cycle. The curves are sketched with a dotted black line, dashed red line and solid blue line, respectively. The mechanical stress closely follows the rotational speed of the rotor. The centrifugal forces are the main contributors to the mechanical stress, whereas the tangential forces caused by the torque play a minor role. The maximum mechanical stress during the drive cycle does not exceed 43 MPa.

In principle, the thermal stresses follow the temperature curve presented in Fig. 5. The thermal stresses are due to the temperature gradient along the structure. When the load of the motors is increased, the losses of magnets increase, which causes a higher temperature gradient. In the time spans where the structure experiences a faster temperature increase (70–100, 240–280 and 475–500 s) also the thermal stresses increase faster. At higher temperatures, when the temperature increases more steadily, the structure heats up more uniformly, resulting in a lower temperature gradient and a hardly noticeable increase in the thermal stress levels.

In Fig. 8 is plotted the maximum temperature difference over the simulated time. During previously discussed time spans (70–100, 240–280 and 475–500 s), when the maximum temperature increases fast, the maximum temperature difference is also increasing rapidly. During these time spans the heat generation inside the structure is fast, but the heat conduction to the outer surface of the structure, where the air cooling is affecting, happens more slowly. Therefore, the temperature difference is rising when losses are increased rapidly.

Even though the thermal stress only and the combined stress in Fig. 7 are basically constantly increasing, the temperature difference at the time step 450 s in Fig. 8 is actually as low as it was 350 s earlier. This is due to the transient heat conduction

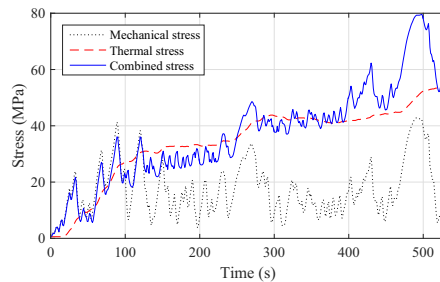


Fig. 7. Von Mises stress history in magnet pocket upper fillet in different loading conditions: mechanical load, thermal load and combined load.

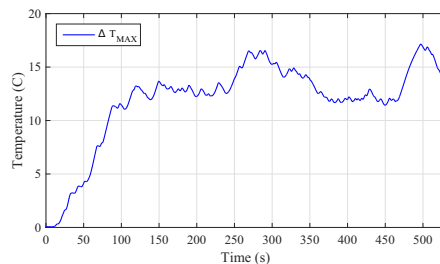


Fig. 8. The maximum temperature difference of the FE-model during the simulation.

that is slowly distribution the heat in solid bodies. Despite the fact that the heat energy due to the electrical losses is constantly flowing to the structure, after a given time, the heat conduction will reduce the difference between the minimum and maximum temperature of the structure. Also, when the surface temperature is increased the air cooling will become more efficient.

For better visualization, in Figs. 9–11 the temperature and stress distributions of the FE-model studied at previously compared time steps 100 s, 280 s and 500 s, correspondingly, are presented. The contour limits for both temperature and von Mises stress are fixed for comparison purposes. The temperature growth is clearly visible as time increases. Although, the growth in the stress is not that visible due to the generally low stress level and local peak stress located in the upper magnet pocket fillet.

When considering only the behavior of the mechanical and the thermal stresses, it can be seen that loading of the motors increases the stresses of both stress types. However, this is not the whole truth if the stresses are observed separately and the total stress level is considered by summing the stress components using the superposition principle. In general, as shown in Fig. 7 the thermal stresses increase the base level of the combined stresses, and stress variation in the combined stress curve is caused by the mechanical stresses. Comparison of the fluctuation of the mechanical stress and combined stress curves shows that the mechanical stresses experience more dramatic changes during the drive cycle, and the residual thermal

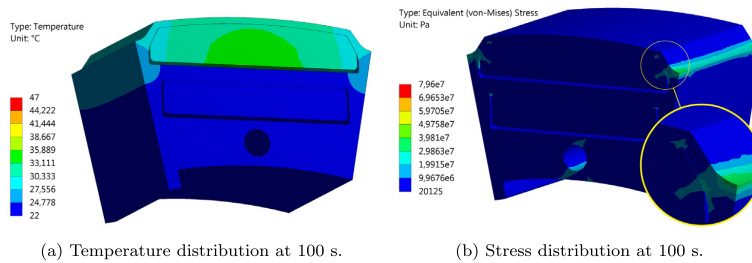


Fig. 9. Rotor temperature and stress distributions at 100 s.

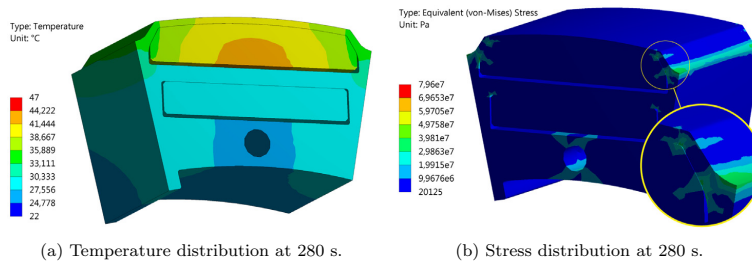


Fig. 10. Rotor temperature and stress distributions at 280 s.

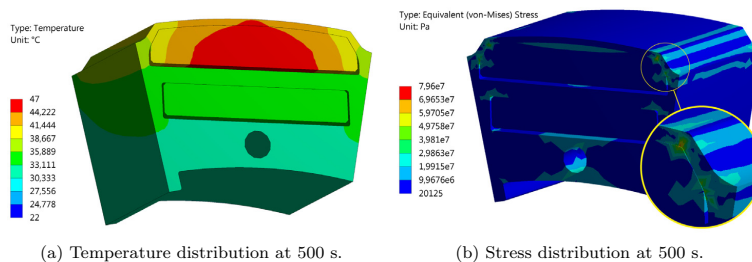
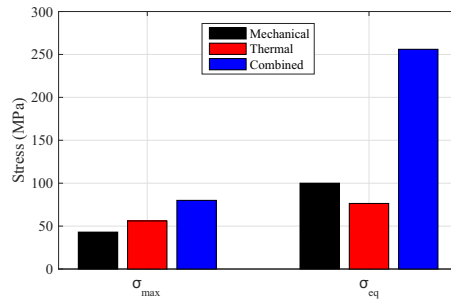


Fig. 11. Rotor temperature and stress distributions at 500 s.

Table 4
Fatigue analysis results.

Stress type	Mechanical	Thermal	Combined
$\Delta\sigma_{eq}$ (MPa)	100	76.4	256
N_f (1×10^6 cycles)	3.2×10^5	5.5×10^6	17

**Fig. 12.** Comparison of the stress levels.

stresses clearly elevate the combined stress peaks. Thermal and mechanical stresses have different dominating multiaxial stress components, and these stresses combined are actually less than the thermal stresses alone within certain period over the stress history.

According to Fig. 6, the uppermost corner is the critical area where the maximum stress occurs. Using (1) and (2) the equivalent stress $\Delta\sigma_{eq}$ and the number of cycles N_f are calculated and shown in Table 4.

A comparison between the maximum stresses in the drive cycle σ_{max} and the equivalent stresses σ_{eq} caused by mechanical, thermal, and combined loads, calculated for the fatigue study, is illustrated in Fig. 12. The mechanical stresses were produced by a model where the centrifugal force and electromagnetic torque are affecting forces. Again, the thermal stresses were provided by a model with thermal loads only. Finally, the combined stresses were obtained from a model comprising all thermal loads, centrifugal forces and electromagnetic torque. As can be seen in Fig. 12, the thermal stresses are higher than the mechanical stresses when the maximum stress peaks are observed. In contrast, the equivalent stress levels of the mechanical stresses are higher than the thermal stresses because the fluctuation of stresses is much more aggressive as a result of the rapidly and constantly changing rotational speed. When these two factors, viz. the rapidly changing mechanical stresses and the relatively high but slowly changing thermal stresses are combined, the results shows a considerably high equivalent stress level. These results emphasize the importance of taking into account both the mechanical and thermal loads particularly when estimating the lifetime of traction motors, where the loads are highly cyclic and the conditions are constantly changing.

5. Conclusions

In this work, a method for calculating the thermomechanical stress and fatigue analysis for a traction motor was presented. A finite element method was utilized to solve coupled thermal and mechanical problem. The results showed a significant change between mechanical and combined thermomechanical stress levels and in the predicted fatigue life depending on whether the thermal loads were taken into account or not. In the studied traction motor, the total stresses were at an acceptable level even when the thermal effects were included. This was due to the conservative approach adopted in the design process. Nevertheless, the mechanical durability of the rotor could be increased by sacrificing some of the electromagnetic performance. Therefore, it was emphasized that a comprehensive thermomechanical analysis is essential for optimal design. Such thermomechanical analysis can be accomplished by employing the procedure proposed in this paper. Further development of the transient thermal analysis will facilitate solution of the electrothermomechanical coupling problem of interior PMSMs.

References

- [1] J. de Santiago, H. Bernhoff, B. Ekergård, S. Eriksson, S. Ferhatovic, R. Waters, M. Leijon, Electrical motor drivelines in commercial all-electric vehicles: a review, *IEEE Trans. Veh. Technol.* 61 (2) (2012) 475–484, <https://doi.org/10.1109/TVT.2011.2177873>.
- [2] A. El-Refaie, Motors/generators for traction/propulsion applications: a review, *IEEE Veh. Technol. Magaz.* 8 (1) (2013) 90–99, <https://doi.org/10.1109/MVT.2012.2218438>.

- [3] I. Boldea, L. Tutelea, L. Parsa, D. Dorrell, Automotive electric propulsion systems with reduced or no permanent magnets: an overview, *IEEE Trans. Indust. Electron.* 61 (10) (2014) 5696–5711, <https://doi.org/10.1109/TIE.2014.2301754>.
- [4] G. Dajaku, H. Hofmann, F. Hetemi, X. Dajaku, W. Xie, D. Gerling, Comparison of two different IPM traction machines with concentrated winding, *IEEE Trans. Indust. Electron.* 63 (7) (2016) 4137–4149, <https://doi.org/10.1109/TIE.2016.2544720>.
- [5] N. Bracikowski, M. Hecquet, P. Brochet, S. Shirinskii, Multiphysics modeling of a permanent magnet synchronous machine by using lumped models, *IEEE Trans. Indust. Electron.* 59 (6) (2012) 2426–2437, <https://doi.org/10.1109/TIE.2011.2169640>.
- [6] A. Fatemi, N. Demerdash, T. Nehl, D. Ionel, Large-scale design optimization of PM machines over a target operating cycle, *IEEE Trans. Indust. Appl.* 52 (5) (2016) 3772–3782, <https://doi.org/10.1109/TIA.2016.2563383>.
- [7] F. Chai, Y. Li, P. Liang, Y. Pei, Calculation of the maximum mechanical stress on the rotor of interior permanent-magnet synchronous motors, *IEEE Trans. Indust. Electron.* 63 (6) (2016) 3420–3432, <https://doi.org/10.1109/TIE.2016.2524410>.
- [8] D. Knetsch, M. Funk, T. Kennerknecht, C. Eberl, Load data calculation in electric axle drives and fatigue assessment for the electric motor subsystem, *Mater. Test.* 56 (7–8) (2014) 535–541, <https://doi.org/10.3139/120.110594>.
- [9] P. Lindh, M. Gerami Tehrani, T. Lindh, J. Montonen, J. Pyrhönen, J. Sopanen, M. Niemelä, Y. Alexandrova, P. Immonen, L. Aarniovuori, M. Polikarpova, Multidisciplinary design of a permanent-magnet traction motor for a hybrid bus taking the load cycle into account, *IEEE Trans. Indust. Electron.* 63 (6) (2016) 3397–3408, <https://doi.org/10.1109/TIE.2016.2530044>.
- [10] Y. Lee, *Fatigue Testing and Analysis: Theory and Practice*, Butterworth-Heinemann, 2005.
- [11] Z. Jia, X. Peng, Z. Guan, L. Wang, B. Yue, Evaluation of the degradation of generator stator ground wall insulation under multistresses aging, *IEEE Trans. Energy Convers.* 23 (2) (2008) 474–483, <https://doi.org/10.1109/TEC.2008.918653>.
- [12] V. Climente-Alarcon, J. Antonino-Daviu, E. Strangas, M. Riera-Guasp, Rotor-bar breakage mechanism and prognosis in an induction motor, *IEEE Trans. Indust. Electron.* 62 (3) (2015) 1814–1825, <https://doi.org/10.1109/TIE.2014.2336604>.
- [13] J. Nerg, M. Rilla, V. Ruuskanen, J. Pyrhönen, S. Ruotsalainen, Direct-driven interior magnet permanent-magnet synchronous motors for a full electric sports car, *IEEE Trans. Indust. Electron.* 61 (8) (2014) 4286–4294, <https://doi.org/10.1109/TIE.2013.2248340>.
- [14] P. Lindh, P. Immonen, Y. Alexandrova, M. Gerami Tehrani, J. Pyrhönen, J. Sopanen, The design of rotor geometry in a permanent magnet traction motor for a hybrid bus, in: 2014 International Conference on Electrical Machines (ICEM), 2014, pp. 310–315, doi:<https://doi.org/10.1109/ICELMACH.2014.6960198>.
- [15] A. Kulkarni, S. Ranjha, A. Kapoor, Fatigue analysis of a suspension for an in-wheel electric vehicle, *Eng. Fail. Anal.* 68 (2016) 150–158, <https://doi.org/10.1016/j.engfailanal.2016.05.020>.
- [16] H. Shimazaki, S. Shinomoto, A method for selecting the bin size of a time histogram, *Neural Comput.* 19 (6) (2007) 1503–1527, <https://doi.org/10.1162/neco.2007.19.6.1503>.
- [17] A. Hobbacher, *Recommendations for Fatigue Design of Welded Joints and Components*, Springer, 2009.
- [18] F. Campbell, *Elements of Metallurgy and Engineering Alloys*, ASM International, 2008.
- [19] A. Fatemi, L. Yang, Cumulative fatigue damage and life prediction theories: A survey of the state of the art for homogeneous materials, *Int. J. Fatigue* 20 (1) (1998) 9–34, [https://doi.org/10.1016/S0142-1123\(97\)00081-9](https://doi.org/10.1016/S0142-1123(97)00081-9).
- [20] Y. Gao, R. Long, Y. Pang, M. Lindenmo, Fatigue properties of an electrical steel and design of EV/HEV IPM motor rotors for durability and efficiency, in: SAE 2010 World Congress & Exhibition, doi:<https://doi.org/10.4271/2010-01-1308>.
- [21] J. McFarland, T. Jahns, Investigation of the rotor demagnetization characteristics of interior PM synchronous machines during fault conditions, *IEEE Trans. Indust. Appl.* 50 (4) (2014) 2768–2775, <https://doi.org/10.1109/ECC.2012.6342277>.

ACTA UNIVERSITATIS LAPPEENRANTAENSIS

801. MATTSSON, ALEKSI. Design of customer-end converter systems for low voltage DC distribution from a life cycle cost perspective. 2018. Diss.
802. JÄRVI, HENNA. Customer engagement, a friend or a foe? Investigating the relationship between customer engagement and value co-destruction. 2018. Diss.
803. DABROWSKA, JUSTYNA. Organizing for open innovation: adding the human element. 2018. Diss.
804. TIAINEN, JONNA. Losses in low-Reynolds-number centrifugal compressors. 2018. Diss.
805. GYASI, EMMANUEL AFRANE. On adaptive intelligent welding: Technique feasibility in weld quality assurance for advanced steels. 2018. Diss.
806. PROSKURINA, SVETLANA. International trade in biomass for energy production: The local and global context. 2018. Diss.
807. DABIRI, MOHAMMAD. The low-cycle fatigue of S960 MC direct-quenched high-strength steel. 2018. Diss.
808. KOSKELA, VIRPI. Tapping experiences of presence to connect people and organizational creativity. 2018. Diss.
809. HERALA, ANTTI. Benefits from Open Data: barriers to supply and demand of Open Data in private organizations. 2018. Diss.
810. KÄYHKÖ, JORMA. Erityisen tuen toimintaprosessien nykytila ja kehittäminen suomalaisessa oppisopimuskoulutuksessa. 2018. Diss.
811. HAJIKHANI, ARASH. Understanding and leveraging the social network services in innovation ecosystems. 2018. Diss.
812. SKRIKO, TUOMAS. Dependence of manufacturing parameters on the performance quality of welded joints made of direct quenched ultra-high-strength steel. 2018. Diss.
813. KARTTUNEN, ELINA. Management of technological resource dependencies in interorganizational networks. 2018. Diss.
814. CHILD, MICHAEL. Transition towards long-term sustainability of the Finnish energy system. 2018. Diss.
815. NUTAKOR, CHARLES. An experimental and theoretical investigation of power losses in planetary gearboxes. 2018. Diss.
816. KONSTI-LAAKSO, SUVI. Co-creation, brokering and innovation networks: A model for innovating with users. 2018. Diss.
817. HURSKAINEN, VESA-VILLE. Dynamic analysis of flexible multibody systems using finite elements based on the absolute nodal coordinate formulation. 2018. Diss.
818. VASILYEV, FEDOR. Model-based design and optimisation of hydrometallurgical liquid-liquid extraction processes. 2018. Diss.
819. DEMESA, ABAYNEH. Towards sustainable production of value-added chemicals and materials from lignocellulosic biomass: carboxylic acids and cellulose nanocrystals. 2018. Diss.

- 820.** SIKANEN, EERIK. Dynamic analysis of rotating systems including contact and thermal-induced effects. 2018. Diss.
- 821.** LIND, LOTTA. Identifying working capital models in value chains: Towards a generic framework. 2018. Diss.
- 822.** IMMONEN, KIRSI. Ligno-cellulose fibre poly(lactic acid) interfaces in biocomposites. 2018. Diss.
- 823.** YLÄ-KUJALA, ANTTI. Inter-organizational mediums: current state and underlying potential. 2018. Diss.
- 824.** ZAFARI, SAHAR. Segmentation of partially overlapping convex objects in silhouette images. 2018. Diss.
- 825.** MÄLKKI, HELENA. Identifying needs and ways to integrate sustainability into energy degree programmes. 2018. Diss.
- 826.** JUNTUNEN, RAIMO. LCL filter designs for parallel-connected grid inverters. 2018. Diss.
- 827.** RANAEI, SAMIRA. Quantitative approaches for detecting emerging technologies. 2018. Diss.
- 828.** METSO, LASSE. Information-based industrial maintenance - an ecosystem perspective. 2018. Diss.
- 829.** SAREN, ANDREY. Twin boundary dynamics in magnetic shape memory alloy Ni-Mn-Ga five-layered modulated martensite. 2018. Diss.
- 830.** BELONOGOVA, NADEZDA. Active residential customer in a flexible energy system - a methodology to determine the customer behaviour in a multi-objective environment. 2018. Diss.
- 831.** KALLIOLA, SIMO. Modified chitosan nanoparticles at liquid-liquid interface for applications in oil-spill treatment. 2018. Diss.
- 832.** GEYDT, PAVEL. Atomic Force Microscopy of electrical, mechanical and piezo properties of nanowires. 2018. Diss.
- 833.** KARELL, VILLE. Essays on stock market anomalies. 2018. Diss.
- 834.** KURONEN, TONI. Moving object analysis and trajectory processing with applications in human-computer interaction and chemical processes. 2018. Diss.
- 835.** UNT, ANNA. Fiber laser and hybrid welding of T-joint in structural steels. 2018. Diss.
- 836.** KHAKUREL, JAYDEN. Enhancing the adoption of quantified self-tracking wearable devices. 2018. Diss.
- 837.** SOININEN, HANNE. Improving the environmental safety of ash from bioenergy production plants. 2018. Diss.
- 838.** GOLMAEI, SEYEDMOHAMMAD. Novel treatment methods for green liquor dregs and enhancing circular economy in kraft pulp mills. 2018. Diss.

Acta Universitatis
Lappeenrantaensis
839



ISBN 978-952-335-330-5
ISBN 978-952-335-331-2 (PDF)
ISSN-L 1456-4491
ISSN 1456-4491
Lappeenranta 2019
